Università degli Studi di Cagliari

PhD DEGREE

Civil Engineering and Architecture

Cycle XXXIII

TITLE OF THE PHD THESIS

Inversion strategies for seismic surface waves and time-domain electromagnetic data with application to geotechnical characterization examples.

Scientific Disciplinary Sector

GEO/11

PhD Student:	Jeniffer Costa Barreto Viegas
Supervisors	Dr. Giulio Vignoli Dr. Julien Guillemoteau Dr. Jaime Alberto dos Santos

Final exam. Academic Year 2019/2020

Thesis defence: February 2022 Session

Abstract

Geophysical methods are broadly used to map the subsurface. Their ability to investigate large areas in a short time and to reach significant depths with good resolution makes them suitable for a wide range of applications: from hydrological studies, mineral exploration, archaeological investigations to geotechnical characterization.

Unfortunately, most of the geophysical methods are ill-posed. Thus, to be able to effectively invert the geophysical data and get meaningful models of the subsurface a priori information needs to be included in the process. This is the basic idea behind the inversion theory. This thesis deals with the inversion of two types of geophysical measurements: the Seismic Surface Waves (SSW) data and the Time Domain Electromagnetic (TDEM) observations.

The present work consists of two parts: (1) The first one is about possible implementations of the minimum gradient support stabilizer into a SSW inversion routine and its extension to the laterally constrained case. By means of this novel approach, it is possible to tune the level of sparsity of the reconstructed velocity model, providing a solution with the desirable characteristics (smooth or sharp) in both directions (vertically and laterally). The capabilities of the proposed approach have been tested via applications on synthetic and measured data. (2) The second part of the thesis is about the joint interpretation of SSW and TDEM measurements for an improved geotechnical characterization of an area intended for construction. In this case, the SSW results, together with other ancillary data, are used as prior information for the subsequent inversion of TDEM measurements. In this respect, the SSW results have been translated into pieces of information to be used in the TDEM inversion via a petrophysical relationship.

This work is coherent with one of the goals of the United Nations Agenda 2030 for sustainable development [3], specifically, the item 11b, as geotechnical characterization is one of the essential components for the design of civil engineering works, ensuring the necessary safety and resilience to natural disasters and climate change. However, the field of application of the proposed approaches is very broad as they can also be used, e.g., for groundwater mapping, as well as for the evaluation of aquifer contamination. In this respect, the present work is also in line with items 6.1, 6.3 and 6.4 of the 2030 UN Agenda.

Sommario

I metodi geofisici sono largamente utilizzati per mappare il sottosuolo. La loro capacità di investigare rapidamente grandi estensioni e di raggiungere profondità significative con ragionevoli risoluzioni li rende adatti a una vasta gamma di applicazioni: dagli studi idrogeologici, esplorazione mineraria, indagini archeologiche fino a caratterizzazioni geotecniche.

Sfortunatamente, la gran parte dei metodi geofisici sono mal-posti. Di conseguenza, per invertire efficacemente i dati misurati e ottenere modelli significativi del sottosuolo, è necessario includere nel processo le informazioni a priori disponibili. Questa è l'idea di base dietro alla teoria dell'inversione. Questa tesi si concentra su due tipi di dati geofisici: misure derivate dallo studio delle Onde Sismiche Superficiali (SSW), e misure Elettromagnetiche nel Dominio del tempo (TDEM).

Il presente lavoro consiste di due parti: (1) La prima riguarda possibili implementazioni del minimum gradient support stabilizer per l'inversione di dati SSW e la sua estensione al caso vincolato lateralmente. Attraverso questo nuovo approccio, è possibile regolare il livello di sparsità del modello di velocità ricostruito, producendo una soluzione con le caratteristiche desiderate (con variazioni lisce o con interfacce nette) in entrambe le direzioni (verticale e laterale). L'efficacia di questo approccio è stata testata sia su dati sintetici che effettivamente misurati. (2) La seconda parte della tesi è relativa all'interpretazione congiunta di dati SSW e TDEM per una migliore comprensione delle caratteristiche geotecniche di una zona interessata da un cantiere. In questo caso, i risultati SSW, insieme ad altre informazioni ancillari, sono stati usati come informazioni a priori per le successive inversioni di dati TDEM. A questo proposito, i risultati SSW sono stati tradotti in informazioni utili per l'inversione TDEM attraverso una relazione petrofisica.

Questa ricerca è coerente con uno degli obiettivi dell'Agenda delle Nazioni Unite 2030 per lo sviluppo sostenibile [3], in particolare, il punto 11b; infatti, la caratterizzazione geotecnica è necessaria per assicurare la sicurezza e resilienza ai disastri naturali e ai cambiamenti climatici. In ogni caso, il campo di applicazione degli approcci proposti è vasto potendo essere usati, ad esempio, per la mappatura degli acquiferi e per la valutazione della loro contaminazione. In questo senso, la presente ricerca è compatibile anche con i punti 6.1, 6.3, e 6.4 dell'Agenda UN 2030.

Resumo

Os métodos geofísicos são amplamente utilizados para mapear a subsuperfície. A capacidade de investigar grandes áreas em pouco tempo e atingir profundidades significativas com boa resolução, os torna adequados para uma ampla gama de aplicações: desde estudos hidrológicos, exploração mineral, investigações arqueológicas até caracterizações geotécnicas.

Infelizmente, a maioria dos métodos geofísicos são mal condicionados. Assim, para poder inverter efetivamente os dados geofísicos e obter modelos com significado da subsuperfície, é necessário incluir informações a priori no processo. Esta é a ideia básica por trás da teoria da inversão. Esta tese trata da inversão de dados de dois métodos geofísicos: Ondas Sísmicas de Superfície (SSW) e Eletromagnético no Domínio do Tempo (TDEM).

O presente trabalho é composto por duas partes: (1) A primeira parte abrange possíveis implementações de um estabilizador do tipo do suporte de gradiente mínimo em uma rotina de inversão de SSW e sua extensão para a direção lateral. Por meio dessa nova abordagem, é possível ajustar o nível de esparsidade do modelo de velocidade reconstruído, fornecendo uma solução com as características desejadas (com alterações suaves ou bruscas) em ambas as direções (vertical e lateral). A aplicabilidade da abordagem proposta foi testada através da inversão de dados sintéticos e reais. (2) A segunda parte da tese trata da interpretação conjunta dos dados SSW e TDEM para uma melhor caracterização geotécnica de uma área destinada à construção. Neste caso, os resultados da inversão SSW, juntamente com outros dados auxiliares, são utilizados como informação prévia para a posterior inversão dos dados TDEM. A ligação entre os diferentes dados é feita através de relações petrofísicas.

Este trabalho é coerente com um dos objetivos da Agenda 2030 das Nações Unidas para o desenvolvimento sustentável [3], especificamente, o item 11b, pois a caracterização geotécnica é uma das componentes essenciais para o dimensionamento das obras de engenharia civil, assegurando a segurança e a resiliência necessárias aos desastres naturais e alterações climáticas. No entanto, o campo de aplicação das abordagens propostas é muito amplo, pois também podem ser usadas, por exemplo, para mapeamento de águas subterrâneas, bem como para avaliação de contaminação de aquíferos. Nesse sentido, o presente trabalho também está alinhado com os itens 6.1, 6.3 e 6.4 da Agenda 2030 da ONU.

Aknowlodgements

Thank you, God, for guiding me to this point, and for giving me the strength to keep going.

I would like to thank you, my tutors, Jaime Santos and Julien Guillemoteau for the instructions, the lectures, the time, and support in developing this thesis.

Thank you to prof. Fernando Santos, for guiding me through the TDEM method, for lending me the equipment, for all the knowledge shared.

Thank you, Francisco Moreno, for the help in acquiring the data.

Thank you, my dear friends, Pedro, Cláudia, and Zjambor for helping me at the field several times and for the support during this Ph.D.

Thank you, Isabel, for teaching me the MASW method, for having me in your field survey, and for all explanations.

Thank you, Prof. Leonardo Azevedo, for accepting me into your group when I needed it most.

A special thank you to my tutor Giulio Vignoli that besides all the academic support, also helped me in my 'less good' moments with kindness and care.

Thank you to the amazing people I have met during this journey and that has made my period in Italy more shine and happy: Thank you Peng and Fabrizia.

Thank you to all the other colleagues I made, and that share their knowledge with me, from IST and FCUL.

Finally, thank you to my family for the all support and love (and understanding!), I wouldn't be able to be here without you guys.

Contents

Acronyms

a.c	alternating current.
d.c	direct current.
DOI	Depth of Investigation.
EM	Electromagnetic.
FDEM	Frequency Domain Electromagnetic.
LCI	Laterally Constrained Inversion.
MASW	Multichannel Analysis of Surface Waves.
MGN	Minimum Gradient Norm.
MGS	Minimum Gradient Support.
SI	International System of Units.
SSW	Seismic Surface Waves.
TDEM	Time-Domain Electromagnetic.

List of symbols

β	Trade-off parameter.
E	Young's modulus.
E	Electric Field.
D	Electric displacement.
ε_v	Volumetric strain.
ε	Dielectric permittivity.
e_z	Base vector normal to the surface.
G	Shear Modulos.
H	Magnetic field.
J	Current density.
K	Bulk modulus.
λ	Wavelength.
λ	Lamé's constant.
μ	Lamé's constant.
ν	Poisson's ratio.
ρ	Material density.
ρ	Eletrical resistivity.
σ	Estimated uncertainty.
σ_{ij}	Stress component.
σ	Eletrical conductivity.
u_i	Displacement component.
V_P	Compression-wave velocity.
V_R	Rayleigh-wave velocity.
V_S	Shear-wave velocity.
ζ	Focusing parameter.

List of Figures

List of Tables

Chapter 1

Introduction

1.1 Motivation & Objectives

Reconstructing subsoil characteristics, is the first step in designing foundations for further construction. Common strategies for geotechnical characterization rely on intrusive tests which only provides information from a determined point in depth where the test was carried out. These tests, such as boreholes, Standard Penetration Tests (SPT) and Cone Penetration Tests (CPT), are time consuming and require large and heavy equipments. The cross-hole test is another option for characterizing the subsoil, but is intrusive and expensive. Seismic surface waves (SSW) and time domain electromagnetics (TDEM) are two types of surveys that allow the investigation of the earth without intrusion. This is desirable for places where there is no possibility of drilling, or to bring large and heavy equipments such as urban zones, or zones with difficult access. SSW and TDEM can also provide information about large areas in less time than current intrusive techniques. The big issue with SSW and TDEM is to process the data. The inversion of SSW and TDEM data are ill-posed problems, in the sense that for the same dataset several earth models can be reproduced. This thesis deals with the ill-posedness of the inversion in a deterministic way, where the goal is to obtain from all models that fit the data, the one that also is compatible with some prior information, given by the user. The prior information is introduced through regularization strategies, that can tune the resulting model to some specific characteristic, for example, to reproduce sharp interfaces, or smoothly change in depth. In order to be able to control the shape of the resulting inversion model, this thesis presents a tunable stabilizer, implemented for a SSW inversion algorithm. This stabilizer allows the user to control the level of sharpness of the final model. The first goal of this thesis concerns with the implementation of the minimum gradient support (MGS) stabilizer to invert SSW data. By playing with the focusing parameter ζ , the MGS stabilizer allows the user to tune the penalties to be applied in variation on the inverted model. This methodology was extended into the lateral direction, which gives rise to a pseudo-2D model laterally constrained with tunable level of sparsity. The second goal of this work, is try to combine different datasets, such as SSW and TDEM, to characterize the subsurface.

SSW and EM methods offer complementary information about the subsurface of the Earth. Clearly, the physics of the methods is completely different and, so, the properties they can sense are different: in one case, SSW methods can infer mechanical subsurface property (e.g. shear modulus), in the other case, EM methods can be used to reconstruct the electrical property of the ground (e.g. electrical conductivity).

Combining SSW and TDEM improves the resolution and reliability of the geotechnical characterization study, with an eventual reduction of the number of field tests required and, consequently the associated cost and time. For this purpose, the possibility of a mutually constrained SSW-TDEM inversion is investigated, using open source softwares.

1.2 Methodology

The methodology is presented according to each thesis objective.

For the first goal - Implementation of MGS to SSW inversion routine:

- The MGS stabilizer was implemented in in the framework on an already existing inversion package [42].
- The stabilizer was tested with synthetic and real data proving its capability in providing tunable sparsity results.
- The applicability of the tunable stabilizer has been extended and made capable to act, not only vertically, but also horizontally; in this way, it has been possible to obtain pseudo-2D reconstructions with variable levels of sparsity (in both spatial directions). As before, the new pseudo 2D approach has been tested and validated via synthetic and experimental datasets.

For the second goal - Characterization of the subsurface by combining different datasets:

- Firstly, fieldwork has been carried out, where TDEM and SSW data were collected.
- Secondly, the data were individually processed and inverted by using preexisting softwares [20, 42].
- Finally, the SSW data and borehole information were used to constrain the TDEM inversion. In order to validate the geophysical results, a thorough comparison against other ancillary measurements has been performed.

1.3 Thesis outline

This thesis follows the sequence below:

- Chapter 2: The reader is introduced to the main topics developed in the thesis: TDEM and SSW. The first section is about electromagnetics - An introduction to Maxwell's equation followed by the description of electromagnetic properties is given, and finally the electromagnetic time-domain method is summarized.

  The second section is about surface waves - An introduction to seismic wave propagation with focus on surface waves is given. The equations and possible numerical solutions for Rayleigh waves in stratified media are also discussed. By the end, the multichannel acquisition of surface waves (MASW) method is described.

- Chapter 3: The reader is introduced to ill-posed problems and possible ways to tackle them. The inversion theory is briefly explained, with a focus on regularization strategies, some stabilizers are presented.

- Chapter 4: The first goal of the thesis is developed. The implementation of the MGS stabilizer (z-direction) and its extension to x-direction through the laterally constrain inversion are explained. Both are tested with synthetic and real data. This chapter is based on the published article *"Reconstruction, with tunable sparsity levels, of shear wave velocity profiles from surface wave data"* - Vignoli et al. [103], and on the submitted article *"Sparse laterally constrained inversion of surface wave dispersion curves via minimum gradient support regularization"* - Guillemoteau et al. [39], of which the author of this thesis is a co-author.

- Chapter 5: The second goal of the thesis is developed. A case of study is presented. The geotechnical characterization of the place is improved by the constrained inversion of TDEM and SSW, and an analysis of all information available is performed. This chapter is based on two conference papers where the author of this thesis is a co-author:

  - *Inversion of electrical resistivity tomography (ERT) and transient electromagnetic (TEM) data for geotechnical site characterization of PLLN alluvial area, Lisbon.* submitted to the 6^{th} International Conference on Geotechnical and Geophysical Site Characterization that will take place in Budapest - Hu, September 2021 -Baltazar et al. [9].
  - *Inversion of TDEM data constrained by surface seismic and borehole surveys for geotechnical characterization of the Northen Lisbon Logistic Park (PLLN)* presented on the 4^{th} Doctoral Congress in Engineering, that took place in Porto - PT, June 2021 - Viegas et al. [99].

- Chapter 6: Conclusions about what has been done and possible future research are drawn.

Chapter 2

Background

2.1 Electromagnetic Method

2.1.1 Introduction

The need to investigate the interior of the earth, and searching for precious materials boosted the development of Electromagnetic (EM) methods. Since most base-metal massive sulfide ores are very conductive and provide a strong contrast to their host rocks, mineral exploration surveys have been the prime application of the EM methods and the mineral exploration industry has funded most of the development [69]. Comprising a large range of applications from mineral exploration to engineering purposes, EM methods rely on the measurements of electric or magnetic fields by a receiver from some sources of electromagnetic energy (natural or artificial). There are several EM methods, which differ in terms of transmitter, receiver, signal, place where the survey is carried out, etc. A common separation of EM methods is between Time-Domain Electromagnetic (TDEM) method and Frequency Domain Electromagnetic (FDEM) method. In FDEM methods the ground is energized by passing an alternating current (a.c) through a loop situated usually on or above the surface of the earth. The primary field of the loop will induce eddy currents in all conductors present in the earth. The receiver will read the primary and secondary electromagnetic fields. In TDEM methods a strong direct current (d.c) is usually passed through a loop, then this current is abruptly interrupted. When the current is switched off, the secondary fields due to the induced eddy currents in the ground can be read at the receiver in the absence of the primary field. Usually, the secondary field is the one that contains information about the underground conductors and may be several orders of magnitude smaller than the primary field, which makes it desirable to read the secondary field in the absence of the primary field [70]. There is no perfect method, and in the choice of the method should be taken into account: 1) the physical property that better fits the goal of the survey; 2) proper conditions to maximize the contrast of this physical property; 3) the estimated size and depth of the target; 4) the spatial variation of the property under view; 5) the local conditions (topography, access, EM noise, etc.); 6) the time, money and people available [68]. Table 2.1 shows some geophysical methods, including Electromagnetic, and their characteristics.

Geophysical Method	Main sources of the fields	Depths of application	Main Application areas	Survey methods
Gravity	- Natural: (gravitational masses of rocks)	Entire of the Earth	Mining Hydrology Plate tectonics Mantle dynamics Core dynamics	Ground Airborne Spaceborne
Magnetostatic	- Natural (Outer Core convection; solar storms; magnetization of near-surface rocks)	0-20 km 3000-6450 km	Basin analysis Plate tectonics Paleo-tectonics Core dynamics	Ground Airborne Spaceborne
DC resistivity	- Artificial (electric current sources)	0-0.1 km	Hydrology Ore mining	Ground
Magnetotelluric	- Natural (Ionospheric events)	0-150 km	Hydrology Plate tectonics	Ground
Electromagnetic induction	- Artificial (electromagnetic induction)	0-10 km	Geologic mapping Ore mining Metal detection	Ground Airborne
Electromagnetic radiation (GPR)	- Artificial (electromagnetic radiation)	0-0.05 km	Geotechnology Hydrology Archeology	Ground Airborne
Seismic reflection	- Artificial (explosives; falling loads)	0-10 km	Basin analysis	Ground
Seismic refraction	- Artificial (explosives; falling loads)	0-150 km	Basin analysis Crustal studies Plate tectonics	Ground
Earthquake seismology	- Natural (earthquakes in the Crust)	10-6450 km	Plate tectonics Mantle dynamics Core dynamics	Ground
Heat flow	- Natural (radioactivity of rocks; secular heat of the Earth)	0.1-120 km	Crustal rheology Plate tectonics Mantle rheology	Ground

Table 2.1: Principal geophysical methods and some characteristics [29].

2.1.2 Maxwell's equations

All electromagnetic methods obey Maxwell's equations, therefore, a good starting point for understanding these methods is going through these equations. Maxwell's equations are uncoupled first-order linear differential equations that can be coupled by empirical constitutive relations which reduce the number of basic vector functions from five to two. For most earth problems, are assumed [107] isotropy, homogeneity, linearity, and temperature-time-pressure independence of the electrical parameters of local regions of the earth . Maxwell's equations consist of Faraday's and Ampere's laws. In differential form, Faraday's law is:

$$\nabla \times \mathbf{E} + \frac{\partial \mathbf{B}}{\partial t} = 0 \tag{2.1}$$

whereas Ampere's law is:

$$\nabla \times \mathbf{H} - \frac{\partial \mathbf{D}}{\partial t} = \mathbf{J} \tag{2.2}$$

where ∇ is the Laplace operator, **E** is the electric field [V/m], **B** is the magnetic flux density [T], **H** is the magnetic field [A/m], **D** is the electric displacement [C/m^2], **J** is the current density [A/m^2] and t is time [s].

Faraday's law describes how time-varying magnetic fields induce the rotational electric fields, which explain the electromagnetic induction phenomenon (which, in turn, is the fundamental excitation mechanism of the inductive source). Ampere's law describes how currents generate rotating magnetic fields [47, 89].

In order to investigate the properties of the materials, these equations are coupled through constitutive relations which relate the fields and fluxes with physical properties of the materials, explained in section 2.1.3

2.1.3 Electromagnetic properties

In addition, to understand Maxwell's equations, it is necessary to know the meaning of each physical parameter involved. There are three main parameters used to describe the properties of the subsurface from an EM perspective, the electrical conductivity, σ, the magnetic permeability, μ, and the dielectric permittivity, ε. They are used in the constitutive relationships.

Electrical Conductivity

The electrical conductivity σ describes how easily a material can carry electrical current. This material property quantifies the relationship between the electrical field applied **E**, and the current density **J** that flows through the material volume. That relationship is given by the Ohm's law:

$$\mathbf{J} = \sigma \mathbf{E} \tag{2.3}$$

In the International System of Units (SI), the conductivity unit of measurement is Siemens per meter [S/m]. The reciprocal of the conductivity is the resistivity which is measured in Ohm per meter [Ω m]. In general, electrical conductivity is not a scalar but an imaginary number, as it is, in general, a complex function of the frequency [62], [68]. However, for most frequencies used in geophysical methods, the conductivity can be represented by a real number(scalar).

According to its ability to transport electricity, each material can be classified as a conductor, semiconductor, or insulator. In conductors and semiconductors, the electrical conduction mechanism is the same: It is provided through the movement of electrons. The major differences are the temperature effect and the energy necessary to make the electrons move. In conductors, the highest conductivity is achieved for a temperature close to zero, whereas for semiconductors as the temperature rises, the conductivity also increases. The energy required for activation of the electrons in conductors is zero, while in semiconductors, it ranges from a few tenths to several electron volts. In insulators, the conduction is given by ions, which makes a substantial difference between this and the conductors and semiconductors: while the electrons may move rather freely over the energy barriers between atoms, the ions would have more barriers to overcome in order to move around [80].

When investigating the subsurface, two materials are essential: rocks and soils. A definition is given by Samtani and Nowatzki in [84] :

> *Rock is a relatively hard, naturally formed solid mass consisting of various minerals and whose formation is due to any number of physical and chemical processes. The rock mass is generally so large and so hard that relatively great effort (e.g., blasting or heavy crushing forces) is required to break it down into smaller particles.*
>
> *Soils are defined as a conglomeration consisting of a wide range of relatively smaller particles derived from a parent rock through mechanical weathering processes that include air and/or water abrasion, freeze-thaw cycles, temperature changes, plant and animal activity, and chemical weathering processes that include oxidation and carbonation. The soil mass may contain air, water, and/or organic materials derived from the decay of vegetation, etc. The density or consistency of the soil mass can range from very dense or hard to lose or very soft.*

Unfortunately, there is no precise and direct correspondence between the rock type and its electrical properties as the conductivity is highly dependent not only on the lithology, but also on the porosity/connectivity and the characteristics of the pore-filling fluid. With some exceptions, the solid minerals which constitute the rock or soil are good insulators.

The electrical properties of the rock tend to be controlled by the more conductive components of the rock, especially if the rock has a significant porosity. For example, if the rock is fractured and filled with water, the conductivity that one could sense via geophysical methods would be mainly affected by the water conductivity rather than the rock, and this, in turn, would depend on the fluid salinity. [25, 80]. Generally speaking, the three types of rocks, sedimentary, igneous, and metamorphic can be described as follows [68]:

- *Sedimentary* are usually characterized by having higher porosity and larger conductivity; there are, however, some exceptions such as dried sand dunes and gypsum.
- *Igneous* rocks generally have low conductivities since they are less porous, but, if they are fractured, the conductivity may increase dramatically.
- *Metamorphics* rocks present conductivity values between those of the sedimentary and igneous counterparts. As the porosity and the water content depends on the metamorphism degree, the electrical conductivity decreases with it. In addition, often, metamorphic rocks are characterized by anisotropic conductivities.

Similarly, analogous ambiguities in terms of electrical property correspondence affect also the different types of soil. So, as above-mentioned, soil electrical properties hang on several features such as particle size distribution, mineralogy, porosity, pore size distribution, connectivity between pores, degree of water saturation, salinity, and temperature [83].

Tables 2.2 and 2.3 show typical values of resistivities for rocks and table 2.4shows typical values of resistivities for soils. Clearly, resistivity varies over a wide range (despite the fact that these kinds of tables are merely indicative). Often, the signal contains high geological noise, and the resistivity value itself is not meaningful. In this situation, the variation of the resistivity values is analyzed rather than the values themselves [65].

Table 2.2: Resistivities of igneous and metamorphic rocks [65].

Rock Type	Resistivity range (Ω.m)
Granite	3×10^2 - 10^6
Feldspar porphyry	$4{,}5 \times 10^3$ (wet)
Albite	3×10^2 (wet) - $3{,}3 \times 10^3$ (dry)
Syenite	10^2 - 10^6
Diorite	10^4 - 10^5
Quartz diorite	2×10^4 - 2×10^6 (wet) - $1{,}8 \times 10^6$ (dry)
Dacite	2×10^4 (wet)
Andesite	$4{,}5 \times 10^4$ (wet) - $1{,}7 \times 10^2$ (dry)
Diabase (various)	20 - $5\,10^7$
Gabbro	10^3 - 10^6
Basalt	10 - $1{,}3 \times 10^7$ (dry)
Schists (calcareous and mica)	20 - 10^4
Tuffs	2×10^3 (wet) - 10^5 (dry)
Graphite schist	10 - 10^2
Gneiss (various)	$6{,}8 \times 10^4$ (wet) - 3×10^6 (dry)
Marble	10^2-$2{,}5 \times 10^8$ (dry)
Quartzites (various)	10 - 2×10^8

Table 2.3: Resistivities of sediments [65].

Rock Type	Resistivity range (Ω.m)
Consolidated shales	20 - 2×10^3
Argillites	10 - 8×10^2
Conglomerates	2×10^3 - 10^4
Sandstones	1 - $6{,}4 \times 10^8$
Limestones	50 - 10^7
Dolomite	$3{,}5 \times 10^2$ - 5×10^3
Unconsolidated wet clay	20
Marls	3 - 70
Clays	1 - 100
Alluvium and sands	10 - 800
Oil sands	4 - 800

Table 2.4: Resistivity range for various soil materials with their classification according to USCS [11, 65].

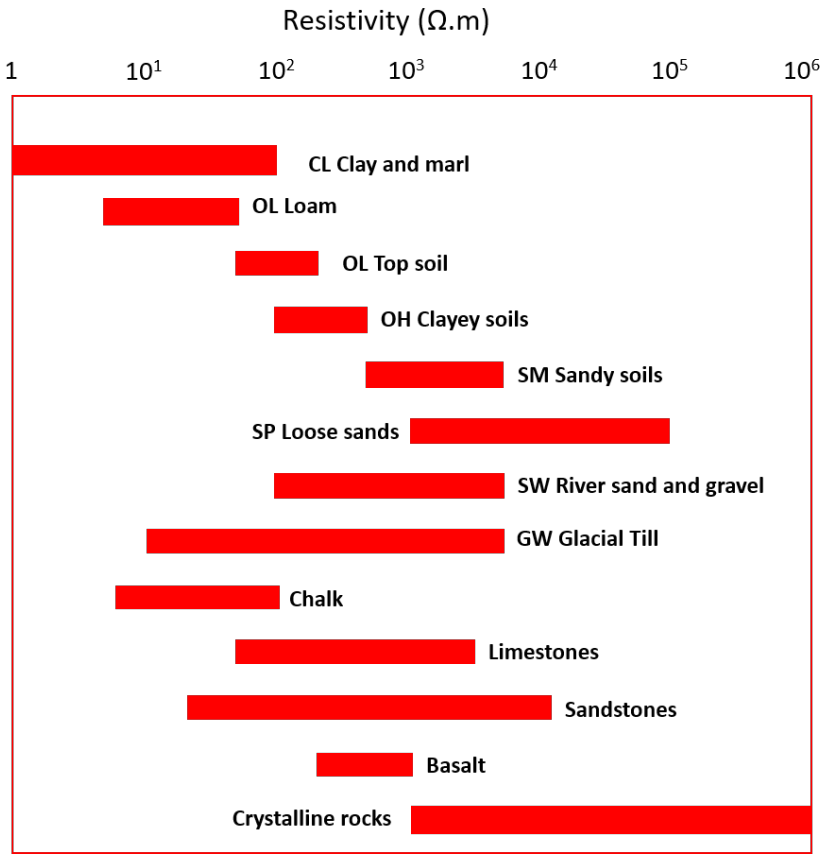

Dielectric Permittivity

An insulator material can be called dielectric since, when subjected to an electric field, it polarizes. Since it is not a conductor, the current does not flow through the material, instead, the current generated by the electric field disturbs its equilibrium position begetting a limited movement of charged particles or orientation of polar molecules defined as dielectric polarization. The dielectric permittivity ε, of different materials, varies according to their ability to become electrically polarised [25]. Dielectric permittivity, ε, is the ratio between the dielectric displacement, $\mathbf{D}$, and the electric field, $\mathbf{E}$ [80], $\mathbf{D} = \varepsilon\mathbf{E}$. Similarly to the electrical conductivity, also the dielectric permittivity is, in its most general form, a tensor and it may have a complex frequency-dependent behaviour.

The ratio of a material's permittivity ε, and the permittivity of the free space ε_0 is known as the dielectric constant κ, and is given by:

$$\kappa = \frac{\varepsilon}{\varepsilon_0} \tag{2.4}$$

Table 2.5 shows the typical ranges of the dielectric onstants for earth materials [48]. From Tab. 2.5 it is possible to see that the range of values for the dielectric constant is narrow when compared with other properties (e.g. resistivity). Most materials have a value between 0 and 50, with the exception of the water, for which this value increases to 81,1. Due to the high value of the dielectric constant of water and its distribution as moisture in rocks and soils, the dielectric constant of geologic structures is strongly affected by the water content [25, 90].

Table 2.5: Dielectric constant for some earth materials [48].

Material	Dieletric constant
Basalt (saturated)	8
Clayey soil (dry)	2
Clayey soil (saturated)	15
Clays	5 - 40
Cultivated soil	15
Granite (dry)	5
Granite (saturated)	7
Humid soil	30
Limestone (dry)	7
Limestone (saturated)	4 - 8
Rocky soil	7
Sand (dry)	3 - 6
Sand (saturated)	20 - 30
Sand soil (dry)	3
Sand soil (saturated)	19
Sandstone (saturated)	6
Shales	5 - 15
Silts	5 - 30

Magnetic Permeability

Magnetic permeability μ is a property of the material describing the degree of induced magnetism that material experiences under the influence of an external magnetic field [89].

The magnetic permeability constitutes the basis for magnetic methods in geophysical exploration but is also relevant for electromagnetic methods [107]. So, the magnetic permeability connects the magnetic field strength **H** to the magnetic flux density **B**

$$\mathbf{B} = \mu\mathbf{H} \tag{2.5}$$

The magnetic permeability of the free space μ_0, in SI units, is equal to $\mu_0 = 4\pi \times 10^{-7} H/m$. In centimeter–gram–second (cgs) units the permeability of free space is dimensionless and has a value of $\mu_0 = 1$. Magnetic properties can also be represented in terms of relative permeability μ_r or magnetic susceptibility κ, given by:

$$\mu_r = \frac{\mu}{\mu_0} \tag{2.6}$$

$$\kappa = \frac{\mu - \mu_0}{\mu_0} = \frac{\mu}{\mu_0} - 1 \tag{2.7}$$

Accordingly to their relative permeability, materials can be classified as diamagnetic, paramagnetic, or ferromagnetic. Figure 2.1 shows the relationship between the flux density **B** and the magnetic field strength **H** for different types of rocks and the vacuum.

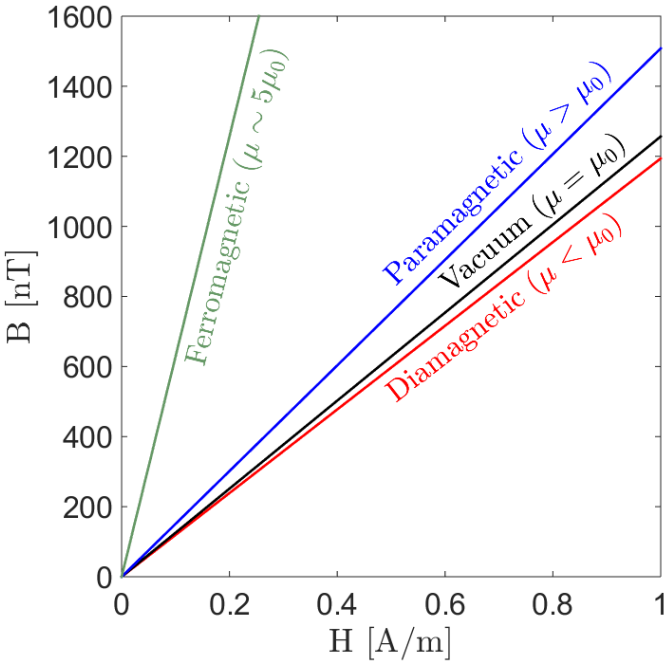

Figure 2.1: Representation of flux density **B** versus magnetic field strength **H** for ferromagnetic, paramagnetic, diamagnetic rocks, and the vacuum. After [89].

A diamagnetic material is characterized by a very weak form of magnetism that is nonpermanent and persists only while an external field is applied. It is induced by a change in the orbital motion of electrons due to an applied magnetic field. The magnitude of the induced magnetic moment is extremely small, and in a direction opposite to that of the applied field [16]. These materials don't have unpaired electrons and are weakly repelled by a magnet. Their relative permeability is slightly less than 1, some examples are bismuth, gold, quartz, silver, graphite, gypsum, air, water, and many clay minerals.

When a paramagnetic material is subject to a magnetic field, their magnetic dipoles align with the external field and become slightly magnetized. These materials have at least one unpaired electron and are attracted by a magnet. The relative permeability in these materials is barely higher than 1, some examples are platinum, oxygen, aluminum, pyroxene, garnet, manganese carbonates, and pyrite [14, 25]. Diamagnetic and paramagnetic materials are considered nonmagnetic because they only present magnetization when in the presence of an external field [16].

Ferromagnetic materials do not present a constant value of relative permeability, as the magnetic field increases, the relative permeability also increases, reaches a maximum, and then decreases [14]. Unlike paramagnetic materials, in ferromagnetic materials, the unpaired electrons are very close to each other giving rise to coupling interactions that cause net spin magnetic moments of adjacent atoms to align with one another, even in the absence of an external field [16]. These materials are strongly attracted by a magnet and some examples are iron, nickel, cobalt, hematite, magnetite [14, 49].

2.1.4 Time Domain Electromagnetic Method

The Time-Domain Electromagnetic (TDEM) method is based upon Faraday's law of induction. Faraday noticed that by passing an electric current on a wire, a magnetic field was generated around it. He came to this conclusion by observing a dipping compass that was near the wire on which the current was flowing, moving on its own. He then thought about the opposite and decided to do the inverse experiment, bringing some magnets closer to a coil connected to a lamp, and observed that in this case, an electric current was generated causing the lamp to light up. That is how the variation in the magnetic field (moving the magnet closer or away) generates an induced current.

For grounded TDEM, an electrical cable is placed on the ground usually forming a square or rectangular loop. The loop is energized by injecting a strong direct current (d.c) through it. The d.c flowing in the cable gives rise to the primary magnetic field, this field is stationary and does not induce underground currents. To induce underground currents, the current in the cable is rapidly switched off (T_{off} from Fig. 2.2), however the magnetic field is not cut off instantaneously, but it does change sharply. The variation of the primary field generates electric fields which give rise to eddy currents in conductors, the faster the variation in the primary field the stronger the eddy current induced. To counteract the effect of these eddy currents, according to Lenz's law[1] a new magnetic field (named secondary) is then created which tends to cancel the variation (decrease) of the primary field. Receivers are usually designed to record the variation of the secondary field, $\frac{\partial B}{\partial t}$, even if, they are becoming common receivers measuring directly the **B**-field.

At time $t = 0$, when the current in the transmitter loop is switched off, the induced currents are confined only to the surface of the conductor (surface currents), and, initially, for a source lying on the ground, they are an exact mirror image of the transmitter loop current [70]. Over time, the eddy currents lose energy, mostly as heat due to the resistance of the conductor, and become weaker, propagating as a "smoke ring" shown in Fig. 2.3. The decay of eddy currents depends on the body's electrical properties and its shape, and since the currents are flowing in different parts of the underground with increasing time, analyzing the variation of the secondary magnetic field can provide information about the distribution of the conductivity [18, 25, 70].

[1] Lenz'law states that an induced electric current flows in a direction such that the current opposes the change that induced it [15]

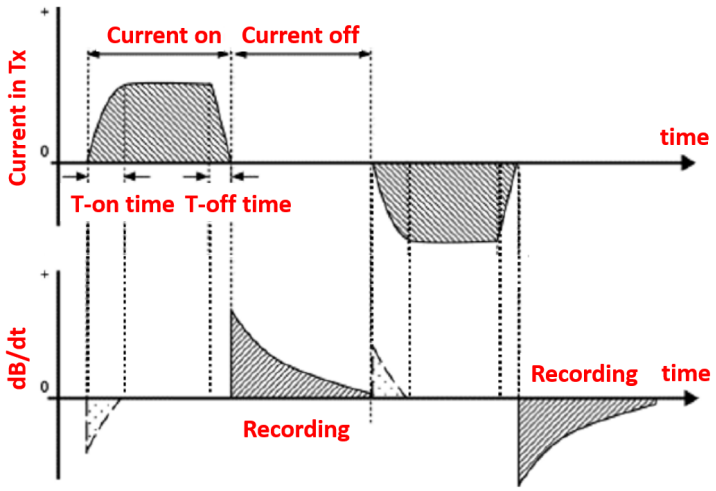

Figure 2.2: Signal in TDEM method: Current and Primary magnetic field (top), and recorded secondary field (bottom). Based on [56].

TDEM methods operate in the quasi-static regime in which the (relatively) high-frequency components in the equations governing the involved phenomena can be neglected [40, 46, 58].

Consistently, in the quasi-static regime, the diffusive term is much larger than the conservation term, i.e.:

$$\sigma \frac{\partial \mathbf{E}}{\partial t} \gg \varepsilon \frac{\partial^2 \mathbf{E}}{\partial t^2} \quad and \quad \sigma \frac{\partial \mathbf{H}}{\partial t} \gg \varepsilon \frac{\partial^2 \mathbf{H}}{\partial t^2}$$

and both $\mathbf{E}$ and $\mathbf{H}$ behave according to the heat equation, with:

$$\nabla^2 \mathbf{E} - \mu\sigma \frac{\partial \mathbf{E}}{\partial t} = 0 \quad and \quad \nabla^2 \mathbf{H} - \mu\sigma \frac{\partial \mathbf{H}}{\partial t} = 0$$

The rate of diffusion is controlled by the product of $\mu\sigma$. However, $\mu \approx \mu_0$ for most materials and σ varying over many orders of magnitude, the diffusive properties of electromagnetic signals are primarily dependent on conductivity.

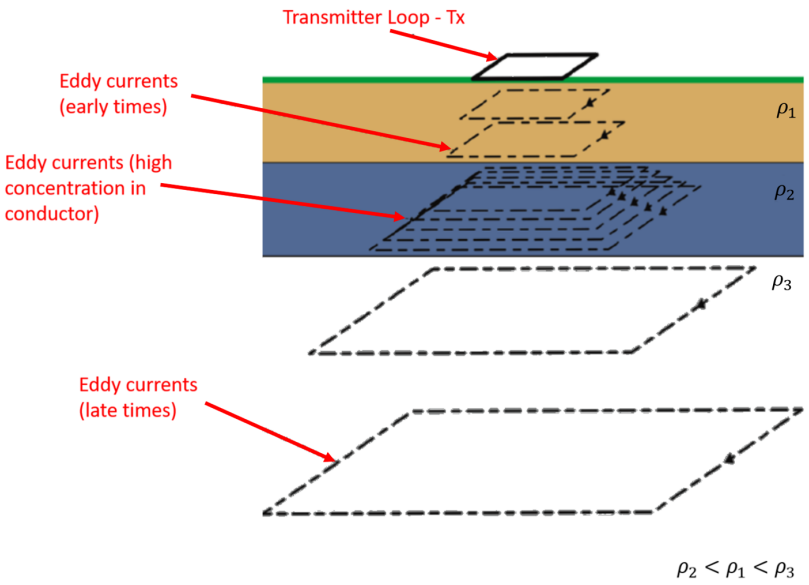

Figure 2.3: Square loop geometric scheme and illustration of the propagation of induced currents. Based on [18].

2.2 Seismic Surface Waves Method

2.2.1 Introduction

Seismic methods take advantage of dynamic perturbations (vibrations) on the subsurface, that can be caused naturally (e.g., earthquake, volcanic eruptions) or by man (e.g, explosions, the drop of a weight) to infer the properties of the medium. The medium properties are inferred by analysing the characteristics (usually the velocities) of the wave produced by the dynamic perturbation and relating them to the subsurface properties (e.g., bulk modulus, shear modulus etc.). Seismic methods can be used for a large range of applications from mine to engineering purposes. The depth of investigation and the resolution will depend on the kind of seismic method applied.

The present research focuses on the application of methods that take advantage of specific portions of the wave-field that is known as surface waves (or ground roll). The surface waves method is suitable for engineering purposes due to its non-intrusive characteristics and the ability to sample a large area with minimum disturbance. The link between the wave propagation properties and the dissipative nature of the soil makes it desirable to solve the inverse problem: identify the geological model that fits the data produced by the dynamic excitation. The growing range of applications of this method has leveraged the development of theoretical and field advancements to maximize the efficiency of the method.

As Aki et al. [2] write in their book :

"Seismology is at an extreme of the whole spectrum of Earth sciences:

- *It is concerned only with the mechanical properties and dynamics of the Earth.*

- *It offers a means by which investigation of the Earth's interior can be carried out to the greatest depths, with resolution and accuracy higher than are attainable in any other branch of geophysics. Resolution and accuracy are good because seismic waves have the shortest wavelength of any wave that can be observed after modulation by passing through structures inside the Earth. Seismic waves undergo the least distortion in waveform and/or the least attenuation in amplitude, as compared with other geophysical observable, such as heat flow, static displacement, strain, gravity, or electromagnetic phenomena.*
- *It contributes to our knowledge of only the present state of the Earth's interior"*

This chapter starts by briefly introducing the reader to seismic wave propagation, with focus on surface waves, following by presenting the forward approach used in this thesis and finally introducing the Multichannel Analysis of Surface Waves (MASW) method.

2.2.2 Seismic Wave Propagation

Waves can be classify as body waves or surface waves. A body wave is a seismic wave that moves through the interior of the earth, as opposed to surface waves that travel near the earth's surface. P and S waves are body waves. Each type of wave shakes the ground in different ways [96]. Because body waves are easy to isolate from other waves in seismograms and their relatively short period, they are suitable for studies of highly localized regions within the earth [2]. Body waves can be divided in:

- Compression waves, P-waves, primary waves, longitudinal waves, dilatation waves, or irrotational waves. They are the first to arrive in the seismic records. In isotropic media, while propagating, compression waves cause the medium portions to be displaced in the parallel direction to the wave propagation. [85].
- Shear waves, also called S-waves, transverse waves, distorsional waves, rotational waves, equivolumial waves, or secondary waves. They constitute the second arrival in seismic records and, in their case, the material displacement is transverse with respect to the wave propagation direction.

In this thesis, surface waves will be explored, more specifically Rayleigh waves.

2.2.3 Surface Waves

Surface waves travel in shallow zone (the depth reached by surface waves will depends on the wavelength as well as the frequency of the source used to generates the signal), in presence of a free boundary, such as the surface of the earth, and propagate parallel to this surface. They are radiated at the surface and oscillate similar to capillary water waves in the water as shown in Fig. 2.4. They are the last to arrive in the seismography, have a higher amplitude, and generate larger ground movements than body waves.

With increasing distance to the source, the wave energy decreases, this effect is called *geometrical attenuation or damping*. In an elastic half-space, the amplitude of the body waves into the solid decreases in proportion to the ratio $\frac{1}{r}$, where r is the distance from the input source. At the surface, for longitudinal and shear waves, the amplitude decreases

with a ratio of $\frac{1}{r^2}$ and for Rayleigh waves this ratio is $\frac{1}{r^{0.5}}$ [28, 33]. Thus, at distances on the order of one to two wavelengths from the source, the contribution of body waves becomes negligible and the wave field is dominated by Rayleigh waves [28, 31, 33].

Rayleigh waves are a combination of longitudinal and vertically polarized transverse waves. The combination of both components defines the movement of a point in the media, that describes in time an ellipse [98]. At the surface, where the motion of the Rayleigh wave is dominated by compression waves (P) and vertical shear waves (SV) components, the particle motion is retrograde elliptical. By a depth, $z \approx 0.2\lambda$ (where λ is the wavelength), the particle motion in the Rayleigh wave becomes dominated by the SV component, and hence, the motion changes into a prograde ellipse as shown in Fig. 2.5 [85]. From Fig. 2.5 is also possible to note that the amplitude of the associated motion decays exponentially with depth, as no energy is propagated in the interior of the half-space, the displacement components have significant energy up to a depth of $z \approx 1.5\lambda$, which foreshow that the energy carried by Rayleigh wave travels predominantly near the surface.

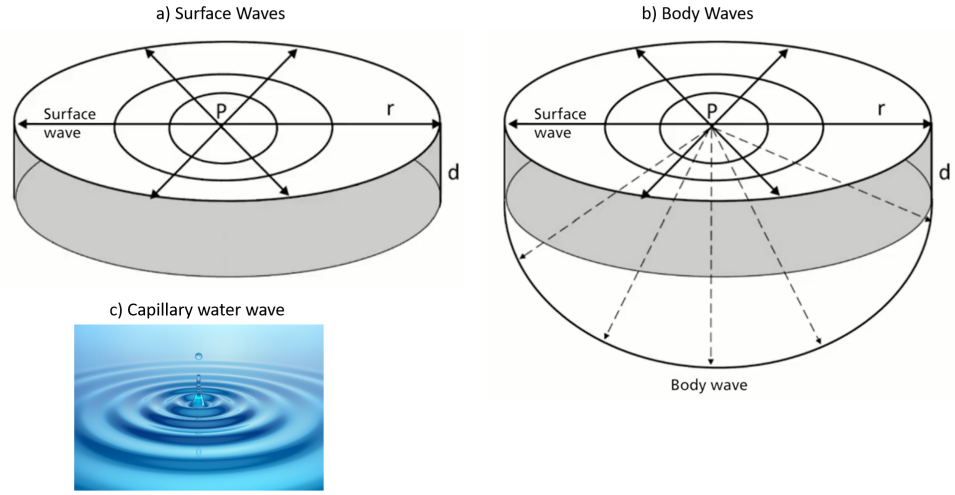

Figure 2.4: Illustration of waves propagation: a) Surface waves are radiated two-dimensionally, and b) body waves spread out in three dimensions - Image adapted from [98]. c) a demonstration of capillary water wave which is similar to surface waves propagation - Image from [8]

The Rayleigh waves are commonly used with the goal to indirectly characterize the soil in terms of stiffness, through the shear modulus G. The speed with which they travel in the media is influenced by the mechanical properties of the media up to a depth of about a wavelength, if the media is inhomogeneous, surface waves of different wavelengths will travel at a different speed because they will sample a media whose properties vary with depth (i.e they are dispersive [2]) [57]. To compute the shear modulus it is necessary to determine the density of the material, ρ, and the shear-wave velocity, V_S. To determine the density is a simple task accomplished, e.g., from laboratory tests or tables. On the other hand, the shear-wave velocity is obtained from seismic techniques. Very often the

[2]Here, dispersive means that the wave velocity depends on the frequency of excitation or wavelength

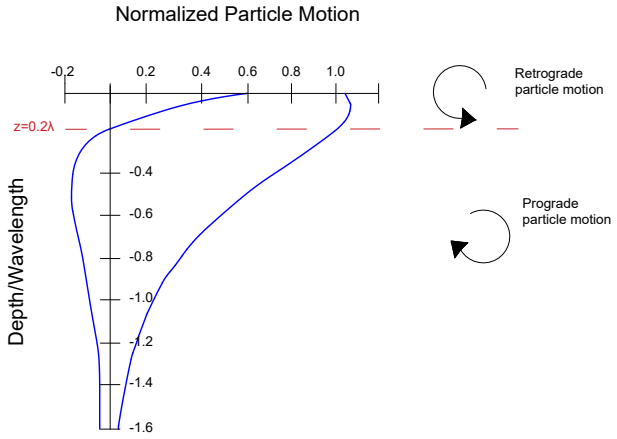

Figure 2.5: Particle motion, horizontal and vertical displacements for Rayleigh waves normalized with respect to the vertical displacement at the surface for Poisson's ratio $\nu = 0.25$. Based on [85]

Rayleigh velocity and shear-wave velocity are considered the same, since they are very close, with an interval of the ratio between the shear-wave velocity, V_S and the Rayleigh velocity, V_R given by $1.05 < \frac{V_S}{V_R} < 1.16$ [21, 28]. The relationship between the V_S and G is given by:

$$G = \rho V_s^2 \tag{2.8}$$

Soils behave differently under different strain levels, vibrations such as the one produced by seismic techniques usually imply very small strain, which allows the model to be linear. There are two models currently used to represent the soil behavior at very small strain: linear elasticity and linear visco-elasticity. The linear model does not allow the dissipation of energy, which happens even for very low cyclic shear strains, besides that, this model is still used in many cases due to its simplicity [33].

Considering the equilibrium of a small element of an infinite elastic, isotropic medium and, by neglecting body forces [28], Navier's equation of motion can be written as:

$$\rho\frac{\partial^2 u_x}{\partial t^2} = (\lambda+\mu)\frac{\partial \varepsilon_v}{\partial x} + \mu\nabla^2 u_x \tag{2.9}$$

$$\rho\frac{\partial^2 u_y}{\partial t^2} = (\lambda+\mu)\frac{\partial \varepsilon_v}{\partial y} + \mu\nabla^2 u_y \tag{2.10}$$

$$\rho\frac{\partial^2 u_z}{\partial t^2} = (\lambda+\mu)\frac{\partial \varepsilon_v}{\partial z} + \mu\nabla^2 u_z \tag{2.11}$$

where ∇^2 is the Laplacian operator in Cartesian coordinates defined as:

$$\nabla^2 = \frac{\partial^2}{\partial x^2} + \frac{\partial^2}{\partial y^2} + \frac{\partial^2}{\partial z^2} \tag{2.12}$$

u_x, u_y, and u_z are the displacements in the x- y- and z- directions, respectively. ε_v is the volumetric strain. μ and λ are Lamé's constants. Table 2.6 and Table 2.7 present Lamé's constants and elastic properties, their definition, and relationships.

The propagation of a wave can be represented by Navier's equations (Eqs- 2.9, 2.10 and 2.11) and three solutions can be found:

Symbol	Designation	Definition
E	Young's modulus	$\frac{Longitudinal\ stress}{Longitudinal\ strain}$
G	Shear modulus	$\frac{Shear\ stress}{Shearl\ strain}$
ν	Poisson's ratio	$\frac{Longitudinal\ strain}{transversal\ strain}$
K	Bulk modulus	$\frac{idrostatic\ pressure}{volumetric\ strain}$

Table 2.6: Elastic Constants: name, symbol and definition [33].

	λ,μ	G,ν	E,ν	K,G
λ	λ	$\frac{2G\nu}{1-2\nu}$	$\frac{\nu E}{(1+\nu)(1-2\nu)}$	$K-\frac{2}{3}G$
μ≡G	μ	G	$\frac{E}{2(1+\nu)}$	G
K	$\frac{(3\lambda+2\mu)}{3}$	$\frac{2G(1+\nu)}{3(1-2\nu)}$	$\frac{E}{3(1-2\nu)}$	K
E	$\frac{\mu(3\lambda+2\mu)}{\lambda+\mu}$	$2(1+\nu)G$	E	$\frac{9KG}{3K+G}$
ν	$\frac{\lambda}{2(\lambda+\mu)}$	ν	ν	$\frac{3K-2G}{2(3K+G)}$

Table 2.7: Relationship between elastic constants [33].

- Solution 1: Propagation of a wave of pure volume change (irrational wave)

$$V_P = \sqrt{\frac{\lambda + 2G}{\rho}} \tag{2.13}$$

- Solution 2: Propagation of a wave of pure rotation (equivoluminal wave)

$$V_S = \sqrt{\frac{G}{\rho}} \tag{2.14}$$

- Solution 3: Propagation of a wave whose motion is confined to a zone near the boundary of the half-space - *Rayleigh wave dispersion equation*

$$\left(\frac{V_R}{V_S}\right)^6 - 8\left(\frac{V_R}{V_S}\right)^4 + \left[24 - 16\left(\frac{V_S}{V_P}\right)^2\right]\left(\frac{V_R}{V_S}\right)^2 + 16\left[\left(\frac{V_S}{V_P}\right)^2 - 1\right] = 0 \tag{2.15}$$

Equation 2.15 is obtained for a half-space homogeneous, isotropic elastic media, by imposing the boundary conditions for a free surface, and considering a plane wavefront[3], traveling in the positive x-direction [28].

The relationship between V_S and V_P is given by:

$$\frac{V_P}{V_S} = \sqrt{\frac{2-2\nu}{1-2\nu}} \tag{2.16}$$

From Eq. 2.15 and 2.16 one can see that for homogeneous and linear elastic media, the Rayleigh wave velocity, V_R, depends only on Poisson's ratio, does not depend on the frequency of the wave.

Despite these solutions being used, they do not contemplate the layered nature of the subsurface. Following the theory for propagation of Rayleigh waves in elastic layered media will be presented.

2.2.4 Rayleigh wave propagation in layered elastic half-space

This section presents the theory of Rayleigh waves propagation in elastic and weakly dissipative media. For a horizontally stratified media with homogeneous isotropic layers and free surface, i.e. mechanical properties are only dependent on depth: $\lambda = \lambda(z), \mu = \mu(z)$ and $\rho = \rho(z)$, Navier's equation of motion is given by [38, 57]:

$$\mu\nabla^2\mathbf{u} + (\lambda+\mu)\nabla(\nabla\cdot\mathbf{u}) + e_z\frac{d\lambda}{dz}\nabla\cdot\mathbf{u} + \frac{d\mu}{dz}\left(e_z\times\nabla\times\mathbf{u} + 2\frac{d\mathbf{u}}{dz}\right) = \rho\frac{\partial^2\mathbf{u}}{\partial t^2} \tag{2.17}$$

where e_z is the unit vector normal to the surface.

To seek solutions of Eq. 2.17 representing surface waves, assuming the plane wavefront condition along the x-direction and harmonic waves, the displacement field, **u(x,t)** must be assumed of the form:

For *Rayleigh waves*:

$$\mathbf{u}: \left\{u_x = r_1(z,k,\omega)e^{i(\omega t-kx)}, \qquad u_y = 0, \qquad u_z = r_2(z,k,\omega)e^{i(\omega t-kx)}\right\} \tag{2.18}$$

Equation 2.18 represents a two-dimensional (plane) strain field. For real positive r_1 and r_2 values, the combination of u_x and u_z corresponds to prograde particle motion. When r_1 and r_2 have different signs, particle motion is retrograde. With the boundary conditions of vanishing stress field at the free surface of the half-space and vanishing of stress and displacements field at infinite depth,

$$z = 0 : \sigma_{zz} = \sigma_{zx} = 0$$

$$z = \infty : \sigma_{zz} = \sigma_{zx} = 0 \qquad and \qquad u_x = u_z = 0$$

since the stress and displacement field must be continuous at each layer interface, and applying Hooke's law, the stress σ_{zz} and σ_{zx} are given by:

[3]The plane wave simplification is considered acceptable if the source is relatively far from the observation point. If the source is near the observation point, then the curvature of the wavefront may be taken into account [38].

$$\begin{aligned}\sigma_{zz} &= i\left[(\lambda+2\mu)\frac{dr_2}{dz} + k\lambda r_1\right].e^{i(kx-\omega t)} \qquad \Leftrightarrow \\ \sigma_{zz} &= r_1^{\sigma}.e^{i(kx-\omega t)}\end{aligned} \tag{2.19}$$

$$\begin{aligned}\sigma_{zx} &= \mu\left(\frac{dr_1}{dz} - kr_2\right).e^{i(kx-\omega t)} \qquad \Leftrightarrow \\ \sigma_{zx} &= r_2^{\sigma}.e^{i(kx-\omega t)}\end{aligned} \tag{2.20}$$

where r_1^{σ} is the amplitude of the vertical compression stress σ_{zz}, and r_2^{σ} is the amplitude of the radial shear stress, σ_{zx}.

By substituting Eq. 2.18 into Navier's equation (Eq. 2.17) and rearranging the later in order to include r_1^{σ} and r_2^{σ} as shown in Eqs. 2.19 and 2.20, one obtains [2, 38]

$$\frac{d}{dz}\begin{bmatrix} r_1 \\ r_2 \\ r_1^{\sigma} \\ r_2^{\sigma} \end{bmatrix} = \begin{bmatrix} 0 & -ik & 0 & \frac{1}{\mu} \\ \frac{-i\lambda}{\lambda+2\mu} & 0 & \frac{1}{\lambda+2\mu} & 0 \\ 0 & -\omega^2\rho & 0 & -ik \\ \frac{4k^2\mu(\lambda+\mu)}{\lambda+2\mu} & 0 & \frac{-ik\lambda}{\lambda+\mu} & 0 \end{bmatrix} \cdot \begin{bmatrix} r_1 \\ r_2 \\ r_1^{\sigma} \\ r_2^{\sigma} \end{bmatrix} \tag{2.21}$$

with λ, μ, ρ as a function of depth, z, and the wavenumber, k, as a function of the frequency, ω. Defining the vector $\mathbf{f}(z) = [r_1, r_2, r_1^{\sigma}, r_2^{\sigma}]^T$ and the matrix $\mathbf{A}$(z) denoting the 4×4 array of Eq. 2.21, this equation can be re-written in the compact form:

$$\frac{df(z)}{dz} = \mathbf{A}(z) \cdot \mathbf{f}(z) \tag{2.22}$$

Eq. 2.22 is a first-order, ordinary differential equation and defines an eigenvalue problem with a linear operator $\frac{d}{dz}$. The displacement and stress eigenfunctions are $[r_1(z,k,\omega), r_2(z,k,\omega)]$ and $[r_1^{\sigma}, r_2^{\sigma}]$. The boundary conditions associated with the eigenproblem 2.22 can be deduced from Eqs. 2.18, 2.19 and 2.20.

$$\begin{aligned} &r_1^{\sigma}(z,k,\omega) = r_2^{\sigma}(z,k,\omega) = 0 \qquad at \qquad y = 0 \\ &r_1(z,k,\omega) \to 0, \qquad r_2(z,k,\omega) \to 0 \qquad as \qquad y \to \infty \end{aligned} \tag{2.23}$$

For a given frequency value - ω, each one associated to a given wavenumber - k(ω), is possible to find the solution of Eq. 2.22 subject to the boundary conditions given in Eq. 2.23.

Numerical Solutions

There are several techniques to solve eigenproblems like the one described by Eq. 2.22, such as numerical integration, finite difference, finite element, boundary element, and spectral element methods, nevertheless, the present work will focus on two techniques commonly used by seismologists and geophysicists, the *Thomson-Haskell method* [45], and the method used at the present work, the *Thin-Layer method* [53].

Thomson-Haskell Method

The Thomson-Haskell method is based on the use of transfer matrices in the frequency/wavenumber domain. The matrix formalism is applied to obtain the phase and

group velocities of Rayleigh waves in vertically heterogeneous media that can be idealized by a stack of homogeneous strata overlying a homogeneous half-space. The solutions of Navier's Equation are considered in the form of plane waves, and not the more complex case of waves diverging from a point source. This involves no loss of generality since the point source solution can be developed by integration of plane-wave solutions [45]. In the transfer matrix approach, the displacements and internal stresses at a given interface define the state vector, which in turn is related through the transfer matrix to the state vectors at neighboring interfaces [54]. For a layered soil, like the one shown in Fig. 2.6, the state vectors is given by:

$$\mathbf{z_j} = [u_x, u_y, iu_z, \tau_{xz}, \tau_{yz}, i\sigma_{zz}]^T = \begin{bmatrix} \mathbf{u_j} \\ \mathbf{s_j} \end{bmatrix} \tag{2.24}$$

where, $\mathbf{u}$, τ and σ are the displacement, shear, and normal stress components at a given elevation in the direction identified by the sub-index. The index j represents the *jth* layer. It's assumed that the displacement vector u_j and the stress vector, s_j are functions of z only, i.e., it's considered that the variation of displacements and stresses in the horizontal plane is harmonic. The factor $i = \sqrt{-1}$ in front of σ_{zz} and u_z has the advantage that the stiffness matrices relating stresses and displacements thus defined are symmetric and for the static case, they are in addition real.

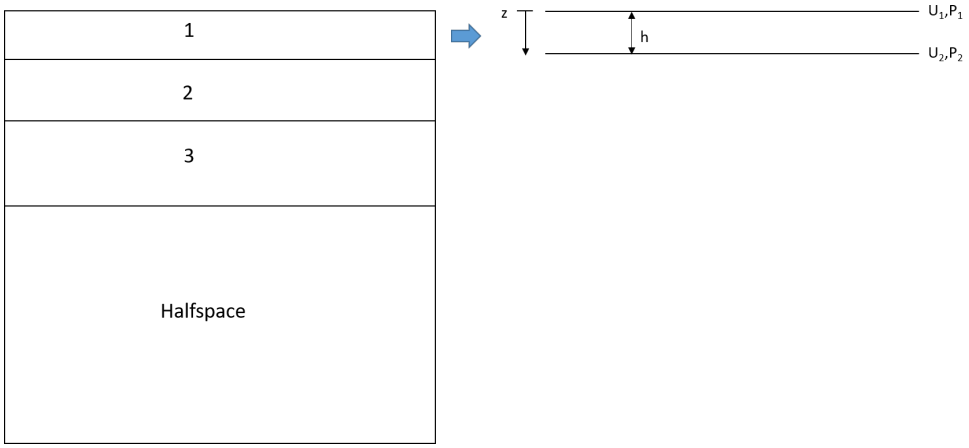

Figure 2.6: Example of layered soil over a half-space

The displacements and stresses at a point, for plane waves, can be obtained by:

$$\begin{bmatrix} \mathbf{U_j} \\ \mathbf{S_j} \end{bmatrix} = \begin{bmatrix} \mathbf{u_j} \\ \mathbf{s_j} \end{bmatrix} \cdot e^{i(\omega t - kx)} \tag{2.25}$$

The state vector from Eq.2.24 at a given interface is related to that at the preceding one by [45]:

$$\mathbf{Z_{j+1}} = \mathbf{H_j Z_j} \tag{2.26}$$

where H_j is the transfer matrix of the *jth* layer. This matrix is a function of the frequency ω, the wavenumber k, the soil properties, and the thickness of the layer [54]. The implementation of the method as well as all equations for the transfer and state matrix are given in detail in [45, 88] and will not be presented here.

To better understand the resolution of Eq. 2.22 with the Thomson-Haskell method, and the meaning of eigenvalue and eigenfunctions, an example extracted from [57] will

be presented. Let's define a layered medium with the properties described in Table 2.8 and represented in Fig. 2.6. Applying the Thomson-Haskell modified algorithm [88], the roots of the Rayleigh dispersion equation, $F[\lambda(z), \mu(z), \rho(z), k_m, \omega] = 0$ can be found for a given frequency. Each root represents an eigenvalue of the eigenproblem from Eq. 2.22, and identifies the number of Rayleigh modes that can exist for a particular layered medium. Figure 2.7 shows the roots of the Rayleigh dispersion equation for the medium with properties described in Table 2.8, where phase velocity is plotted against the frequency. Each dispersion curve is labeled with a number that represents a root from the equation (and so, a eigenvalue). Two frequencies are highlighted with blue lines, to make the comparison easier. At each frequency, the interception with the roots is marked with red circles. As the frequency increases, the number of roots associated with that frequency also increases, as is possible to see by comparing the 5Hz frequency to the 30Hz frequency. On the contrary, at low frequencies, it may be possible that only the fundamental mode is propagating. As $\omega \to \infty$ all the modes tend to a common limit which is the Rayleigh phase velocity of the first layer, that corresponds to $V_S = V_R = 50m/s$. This is not surprising as the high frequencies investigate (i.e. are sensitive) to the very shallow layers: thus, for extremely high frequencies, all the propagation modes sense the very near-surface (and in particular its V_s value). After calculating the roots of the dispersion curve, it is possible to evaluate the eigenfunctions that represent the displacements, u_x and u_z, and the stresses, σ_{zz} and σ_{zx} for the layered medium.

Layer	Thickness[m]	Vp[m/s]	Vs[m/s]	ρ[t/m^3]
1	5	100	50	1.8
2	10	300	200	1.8
3	20	800	500	1.8
half-space	∞	1400	800	1.8

Table 2.8: Medium properties used to construct the Rayleigh secular function plotted in Fig. 2.7 [57].

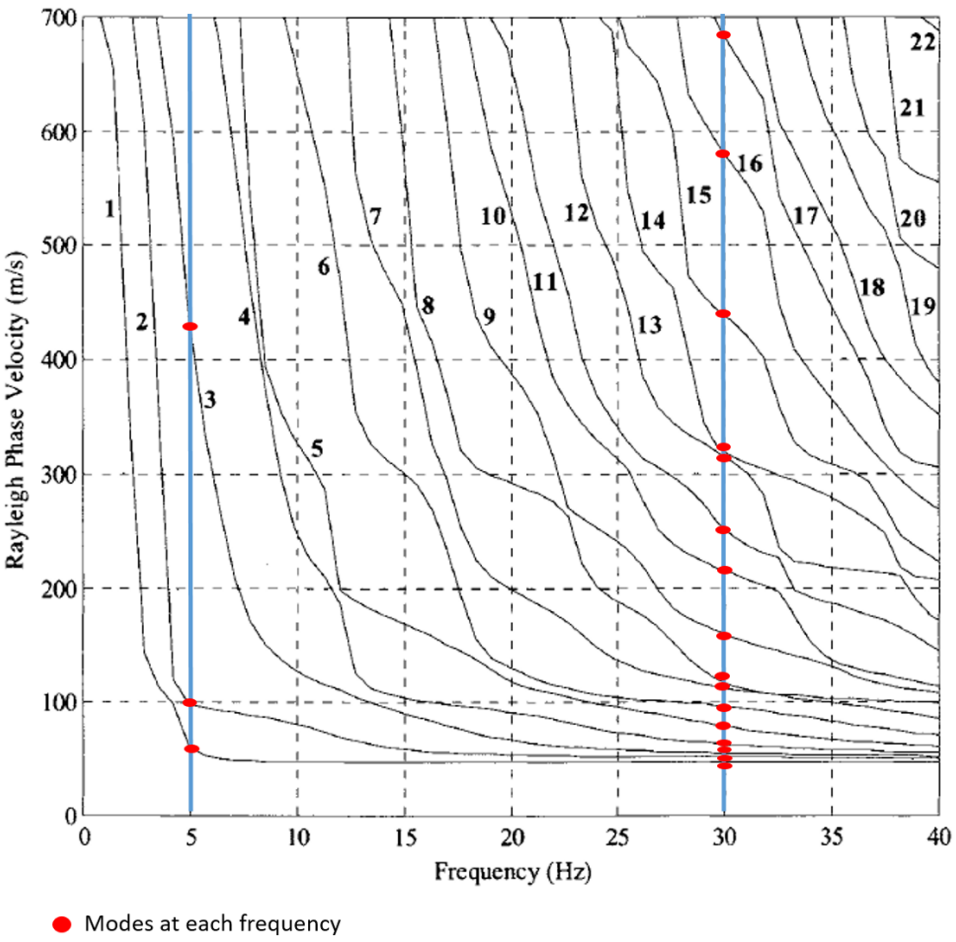

Figure 2.7: Rayleigh dispersion curves for the layered medium of Table 2.8. Each curve denotes a single mode of propagation and corresponds to an eigenvalue of Eq. 2.22 for different values of frequencies. Adapted from [57].

The Thin-Layer method

The thin-layer method results from the Thomson-Haskell method by replacing the transfer matrix into a stiffness matrix very similar to the stiffness matrix widely used in structural analysis. In this method, the displacement field is discretized in the direction of the layering. As a result, the eigenvalue problem changes from transcendental [4] to algebraic (which means that for a fixed frequency, ω, the eigenvalue problem is linear in k^2). These layer stiffness matrices have several advantages over the more usual transfer matrices: 1) they are symmetric; 2) fewer operations are required in its formulation and posterior analysis; 3) it is easier to introduce multiple loading [54].

From Fig. 2.6, by taking one specific layer and by the condition of equilibrium of the external loads, $\mathbf{p}$ with the internal stress $\mathbf{s}$, we have $\mathbf{p}_1 = \mathbf{s}_1$ at the upper interface, and $\mathbf{p}_2 = -\mathbf{s}_2$ at the lower interface. From Eq. 2.26 one obtain:

[4] A transcendental function is an analytic function that does not satisfy a polynomial equation. It cannot be expressed in terms of a finite sequence of the algebraic operations of addition, subtraction, multiplication, division, raising to a power, and root extraction. Examples of transcendental functions include the exponential function, the logarithm, and the trigonometric functions [13].

$$\begin{bmatrix} \mathbf{u}_2 \\ -\mathbf{p}_2 \end{bmatrix} = \begin{bmatrix} \mathbf{H_{11}} & \mathbf{H_{12}} \\ \mathbf{H_{21}} & \mathbf{H_{22}} \end{bmatrix} \begin{bmatrix} \mathbf{u}_1 \\ \mathbf{p}_1 \end{bmatrix} \tag{2.27}$$

where $\mathbf{H_{ij}}$ are submatrices of the transfer matrix $\mathbf{H_j}$. After some matrix algebra:

$$\begin{bmatrix} \mathbf{p}_1 \\ \mathbf{p}_2 \end{bmatrix} = \begin{bmatrix} -\mathbf{H_{12}}^{-1}\mathbf{H_{11}} & \mathbf{H_{12}}^{-1} \\ \mathbf{H_{22}}\mathbf{H_{12}}^{-1}\mathbf{H_{11}} - \mathbf{H_{21}} & -\mathbf{H_{22}}\mathbf{H_{12}}^{-1} \end{bmatrix} \begin{bmatrix} \mathbf{u}_1 \\ \mathbf{u}_2 \end{bmatrix} \tag{2.28}$$

or simply:

$$\mathbf{p} = \mathbf{K}\mathbf{u} \tag{2.29}$$

where $\mathbf{K}$ is the stiffness matrix of the layer (symmetric), $\mathbf{p}$ is the external load vector, and $\mathbf{u}$ is the displacement vector. For layered soils, the global stiffness matrix is obtained by overlapping the contribution of the layer matrices at each "node" (interface) of the system. The global load vector corresponds in this case to the prescribed external stresses at the interfaces. Thus, the assemblage and solution of the equations are formally analogous to the solution of structural dynamics problems in the frequency domain.

If the layer thickness is small when compared to the wavelengths of interest, i.e.:

$$h' < \frac{\lambda_{min}}{4} \Leftrightarrow h' < \frac{V_s}{4f_{max}} \Leftrightarrow \frac{H}{N} < \frac{V_s}{4f_{max}} \tag{2.30}$$

where h' is the thickness of the thin layer, f_{max} is the maximum frequency, H is the total medium thickness to be divided into N thin layers. Under these conditions, a discrete approach can be applied [64] through linearization of the transcendental functions which govern the displacements in the vertical direction, allowing its substitution by algebraic expressions in the frequency and wavenumber domain. In this case, the resulting eigenvalue problem can be solved by standard techniques [54].

The discrete layer stiffness matrices may be obtained as:

$$\mathbf{K_m} = \mathbf{A_m}k^2 + \mathbf{B_m}k + \mathbf{G_m} - \omega^2\mathbf{M_m} \tag{2.31}$$

where k is the wavenumber, ω is the frequency of excitation and $\mathbf{A_m}$, $\mathbf{B_m}$,$\mathbf{G_m}$ and $\mathbf{M_m}$ depend only on material properties of the layer m, and are given by:

$$\mathbf{A_m} = \frac{h}{6}\begin{bmatrix} 2(\lambda+2G) & \cdot & \cdot & \lambda+2G & \cdot & \cdot \\ \cdot & 2G & \cdot & \cdot & G & \cdot \\ \cdot & \cdot & 2G & \cdot & \cdot & G \\ \lambda+2G & \cdot & \cdot & 2(\lambda+2G) & \cdot & \cdot \\ \cdot & G & \cdot & \cdot & 2G & \cdot \\ \cdot & \cdot & G & \cdot & \cdot & 2G \end{bmatrix} \tag{2.32}$$

$$\mathbf{B_m} = \frac{1}{2}\begin{bmatrix} \cdot & \cdot & \lambda-G & \cdot & \cdot & -(\lambda+G) \\ \cdot & \cdot & \cdot & \cdot & \cdot & \cdot \\ \lambda-G & \cdot & \cdot & \lambda+G & \cdot & \cdot \\ \cdot & \cdot & \lambda+G & \cdot & \cdot & -(\lambda-G) \\ \cdot & \cdot & \cdot & \cdot & \cdot & \cdot \\ -(\lambda+G) & \cdot & \cdot & -(\lambda-G) & \cdot & \cdot \end{bmatrix} \tag{2.33}$$

$$\mathbf{G_m} = \frac{1}{h}\begin{bmatrix} G & \cdot & \cdot & -G & \cdot & \cdot \\ \cdot & G & \cdot & \cdot & -G & \cdot \\ \cdot & \cdot & \lambda+2G & \cdot & \cdot & -(\lambda+2G) \\ -G & \cdot & \cdot & G & \cdot & \cdot \\ \cdot & -G & \cdot & \cdot & G & \cdot \\ \cdot & \cdot & -(\lambda+2G) & \cdot & \cdot & \lambda+2G \end{bmatrix} \tag{2.34}$$

$$\mathbf{M_m} = \frac{\rho h}{6}\begin{bmatrix} 2 & \cdot & \cdot & 1 & \cdot & \cdot \\ \cdot & 2 & \cdot & \cdot & 1 & \cdot \\ \cdot & \cdot & 2 & \cdot & \cdot & 1 \\ 1 & \cdot & \cdot & 2 & \cdot & \cdot \\ \cdot & 1 & \cdot & \cdot & 2 & \cdot \\ \cdot & \cdot & 1 & \cdot & \cdot & 2 \end{bmatrix} \tag{2.35}$$

for a medium with 3 layers on a rigid half-space, the global stiffness matrix would be:

$$\mathbf{K} = \begin{bmatrix} \mathbf{K^1_{11}} & \mathbf{K^1_{12}} & & \\ \mathbf{K^1_{21}} & \mathbf{K^1_{22}} + \mathbf{K^2_{11}} & \mathbf{K^2_{12}} & \\ & \mathbf{K^2_{21}} & \mathbf{K^2_{22}} + \mathbf{K^3_{11}} & \mathbf{K^3_{12}} \\ & & \mathbf{K^3_{21}} & \mathbf{K^4_{22}} + \mathbf{K^4} \end{bmatrix} \tag{2.36}$$

where $\mathbf{K^m_{ij}}$ represents a sub-matrix $[2 \times 2]$ from the layer matrix at the layer m. The stiffness matrix has a tridiagonal structure and is symmetric.

The discrete solution is valid for layered soils over a rigid rock, although the analysis of soils over elastic half-spaces could be accomplished with a hybrid formulation (for more details read [53, 54]). An alternative to model the elastic half-space is to discretize the place above the half-space, in contact with the other layers, with a sufficient number of thin layers, until the amplitude of reflected waves by the rigid surface is so small that it has no influence on the global characteristics of the propagation of the Rayleigh waves [31].

By applying spectral decomposition of the stiffness matrix it is possible to obtain the propagation modes. The propagation modes in the stratum are obtained from the eigenvalue problem that follows from setting the vector of external loads, $\mathbf{p}$, from equation 2.29 to zero:

$$\begin{aligned} \mathbf{p} = \mathbf{Ku} \xrightarrow[\mathbf{p}=0]{setting} \mathbf{Ku} = 0 \\ (\mathbf{Ak_j^2} + \mathbf{Bk_j} + \mathbf{C})\phi_\mathbf{j} = 0 \end{aligned} \tag{2.37}$$

where $\mathbf{C} = \mathbf{G} - \omega^2\mathbf{M}$ (from Eq.2.31). The notation for the displacement vector $\mathbf{u}$, has been changed to $\phi_\mathbf{j}$ to emphasize the identification as an eigenvector (the subindex j refers to the various possible solutions) [52]. Eq. 2.37 constitutes a quadratic eigenvalue problem, with eigenvalues $\mathbf{k_j}$ and modal shapes $\phi_\mathbf{j}$. A brief description of the method is given below, for more details, consult [31, 52–54, 64].

- Divide each layer into several thin layers as described by Eq. 2.30;
- Evaluate the matrices $\mathbf{A_m}$, $\mathbf{B_m}$, $\mathbf{G_m}$ and $\mathbf{M_m}$ for each thin layer from Eqs. 2.32, 2.33, 2.34, 2.35;

- Construct the global matrices *A, B, G, M* by overlapping the contribution of each thin layer;
- Evaluate a new matrix $\mathbf{C} = \mathbf{G} - \omega^2\mathbf{M}$ (for each frequency);
- Rearrange the lines and rows of the global matrices by degrees of freedom rather than by interface and evaluate the new matrices **A** and **C**, such that Eq. 2.37 is verified.

2.2.5 Multichannel Analysis of Surface Waves (MASW) method

The dispersive properties of Rayleigh waves make them suitable to investigate the shallow subsurface. The Multichannel Analysis of Surface Waves (MASW) method take advantage of this dispersion property of surface waves for reconstructing the V_s(shear wave velocity) profile in depth of the subsurface. By using several receivers at the same time, MASW integrates the information along the entire acquisition array, improving the data quality and robustness [105]. The method consists of 3 steps [79]: 1) Multichannel data acquisition; 2) extracting dispersion curves (one from each shot), and 3) inverting these dispersion curves to obtain 1D (vertical) V_s profiles (one profile for each dispersion curve). The MASW method investigates the shallow subsurface, going from a few meters to a few tens of meters (e.g., 2-200m), and therefore, the frequency range of the method is about 1Hz to 30Hz [78]. There are two ways to apply the method, depending on the source:

- Active: The surface waves are generated actively through an man-made event, such as explosions, vibrations, the impact of sledgehammer etc. The depth of investigation will depend on the wavelength.
- Passive: The surface waves are generated passively by cultural (e.g., traffic) or natural (e.g., thunder and tidal motion) activities. Can reach an investigation depth of about a few hundred meters.

The survey consists of displaying a receiver (e.g., geophones) array, connected to a recorder (e.g., seismograph), and by recording the time arrivals of the waves. The acquisition is made in the space-time (x-t) domain but for investigating the dispersion property of the subsurface is necessary to transform to a frequency domain. This task can be accomplished in two ways: Transforming the data into a frequency-wavenumber domain (f-k) or to a frequency-slowness domain (f-p). The transformation into the frequency-wavenumber domain is made by applying the Fourier Transform in both, time and space domain, while the transformation into the frequency-slowness domain is made by applying the Slant-stack transform. When a planar, fundamental-mode Rayleigh wave is generated, it also generates several other waves such as body waves, nonplanar surface waves, backscattered waves, and ambient noise. The recorder will receive all these waves. The transformation to the frequency domain allows the identification of noise in the signal and the possibility of applying filters to improve the signal/noise (S/N) ratio. Figure 2.8 represents the workflow of MASW, described below:

- The data is acquired from a multichannel survey;
- The time arrivals recorded is plotted in function of the offset distance (t-x domain), for all waves;

- A dispersion image (overtone) is generated by using a 2-D (time and space) wavefield transformation method (e.g., phase-shift method, tau-pi transformation, f-k, etc.). Some waves are already filtered in this step;
- The dispersion curve is obtained from the dispersion image by following the image trends (e.g. extracting the maximum associated to each wavenumber in the f-k domain)
- The 1D V_s profile is obtained through the inversion of the dispersion curve;
- 2D sections can be obtained by jointly inverting multiple 1D adjacent soundings (Lateral Constrained Inversion - LCI [5, 6]) or by spatial interpolating several 1D models [75].

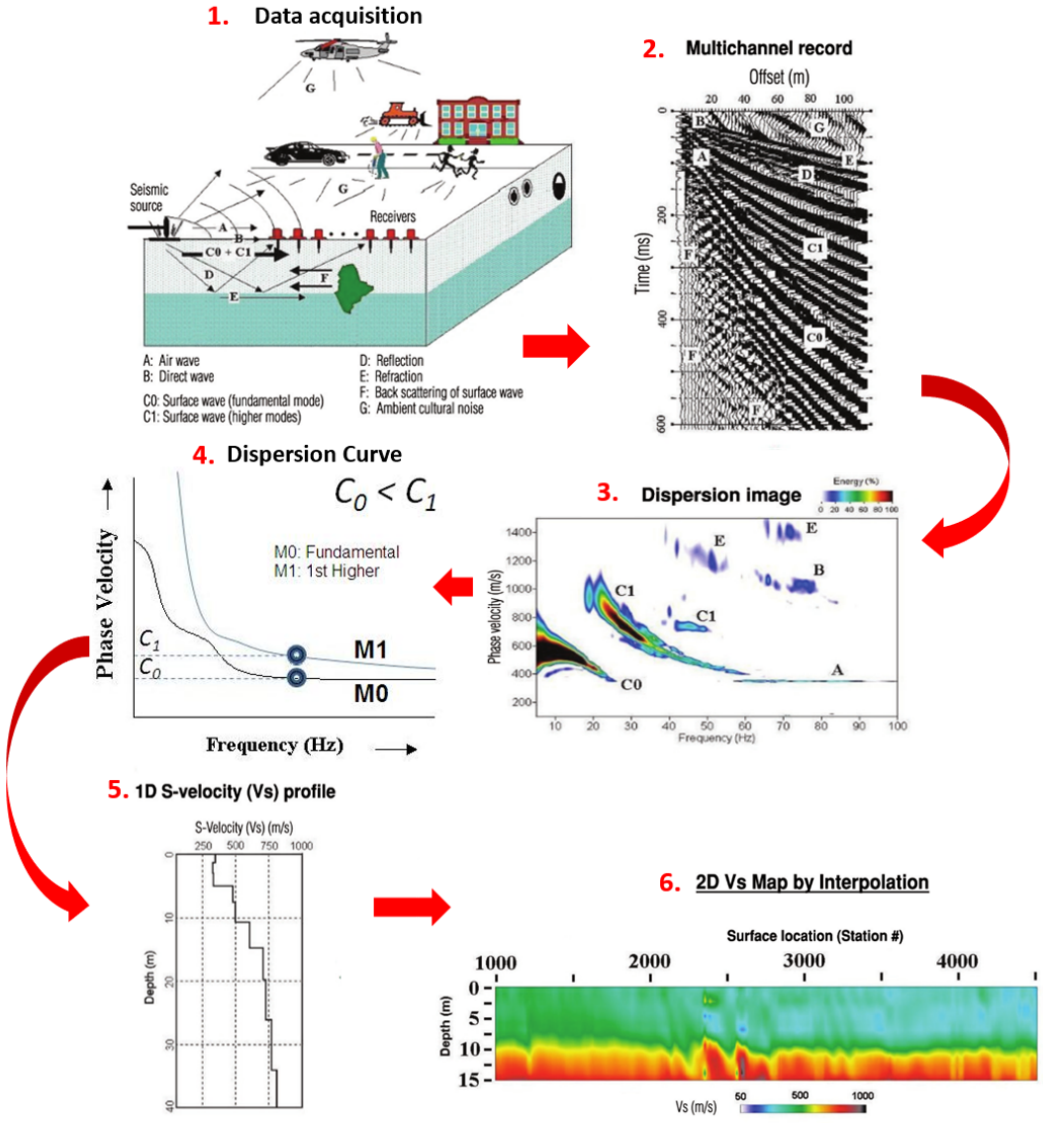

Figure 2.8: Scheme of MASW: from data acquisition to 2D profile. Adapted from [78]

For a detailed description of the MASW method and how to set the survey, please read Park et al. [77], Foti et al. [34], Strobbia [94].

Chapter 3

Inversion Techniques

> "Solution of an inverse problem entails determining unknown *causes* based on observation of their *effects*."
>
> —Oleg Mikailivitch Alifanov

3.1 Introduction

Usually, to investigate the earth's interior, surveys are carried out on the surface. These surveys allow the collection of information concerning the subsurface - the *observed data*. The receiver usually record times or voltages, but for an interpretation from the subsurface what is necessary are parameters that can help to characterize the medium where the signal has travelled, such as the resistivity or the shear velocity. The image from the subsurface can be obtained by parameterizing the "space" under investigation. The space becomes a model, with m_i parameters, and a transformation from the data collected to the model image is applied, this transformation is called inversion. There are several approaches to solve an inverse problem, (e.g., singular value decomposition, least-squares, variational methods, neural networks, Bayesian methods). The data collected are limited in number and they are always characterized by noise. This usually makes the inversion of geophysical data an ill-posed problem.

Most earth problems are ill-posed in the sense that one of the following conditions is not verified: the existence, the uniqueness, and the stability of the solution. To overcome the ill-posed nature of inverse problems, extra information also called *a priori* information is necessary. This information quantifies expectations about the character of the solution that is not based on the collected data, e.g., all parameters are positive and changes slowly. Besides being ill-posed, geophysical problems are also discrete problems. Even if each data provided a value of the property under study at some location, only N values will be available, which is not enough to provide the solution everywhere [73]. Thus, if there exists one solution that fits the data at the desirable noise level, then, there are infinitely many others that will fit just as well. The selection of a unique solution (the best guess) will require additional information.

The inverse problem can be written as a system of equations, where the data collected, $d_{obs} = [d_1, d_2, ..., d_N]^T$ and the model parameters, $m = [m_1, m_2, ..., m_M]^T$ are vectors. The simplest inverse problems are those that can be represented with the explicit linear equation $\mathbf{Gm} = \mathbf{d}$ [73]:

$$\begin{bmatrix} d_1 \\ d_2 \\ \vdots \\ d_j \\ \vdots \\ d_N \end{bmatrix} = \begin{bmatrix} G_{11} & G_{12} & \cdots & G_{1k} & \cdots & G_{1M} \\ G_{21} & G_{22} & \cdots & G_{2k} & \cdots & G_{2M} \\ \vdots & \vdots & \vdots & \vdots & \vdots & \vdots \\ \cdots & \cdots & \cdots & G_{jk} & \cdots & G_{jM} \\ \vdots & \vdots & \vdots & \vdots & \vdots & \vdots \\ G_{N1} & G_{N2} & \cdots & G_{Nk} & \cdots & G_{NM} \end{bmatrix} \cdot \begin{bmatrix} m_1 \\ m_2 \\ \vdots \\ m_k \\ \vdots \\ m_M \end{bmatrix} \tag{3.1}$$

The matrix **G** is called the data kernel, and its elements are given by [73]:

$$G_{jk} = \int_{x_{k-1}}^{x_k} g_j(x)dx \tag{3.2}$$

where $x = (x_0, x_1, ..., x_M)$ are the nodal points of the mesh used to discretize the problem. The function $g(x)$ depends upon the physics of the problem, boundary conditions, and location of sources and receivers. Each kernel entry is the window through which each datum sees the model since the j^{th} datum is given by the inner product of the j^{th} row of **G** with the model vector. So, each datum is a weighted average of the model components. [73].

Usually, the system of equations **Gm=d** is underdetermined, which means there are more model parameters to be determined than data collected ($N<M$), leading to an ill-posed problem without a unique solution.

In mathematical words, the system of equations **Gm=d**, is considered a discrete ill-posed problem if both of the following criteria are verified [43]:

1. The singular values of G decay gradually to zero;

2. The ratio between the largest (σ_1) and the smallest (σ_n) nonzero singular value is large (the condition number of G = $\frac{\sigma_1}{\sigma_n}$ is large)

Given that the matrix **G** has small singular values, it's necessary to incorporate further information about the desired solution, in order to stabilize the problem and to single out a useful and stable solution. This is the purpose of regularization [43].

To find the best model that fits the data, it is necessary to define a "rule" to evaluate each model and thereby select the model that fulfills the prior information available. A possible "rule" is measuring the distance from the observed and calculated data, and selecting the model reproduced by the smallaest distance. The final selected model will be strongly affected by the choice of the "selection rule", all the models that don't satisfy the " selection rule" will be discarded. The present thesis focus on a "selection rule" associated with some definition of distances (to be intended in a broad sense) between models such as:

$$\phi_d = \sum_{j=1}^{N} \left(\frac{\mathbf{d_j^{pred}} - \mathbf{d_j^{obs}}}{\sigma_\mathbf{j}} \right)^2 \qquad = \qquad \left\| \mathbf{W_d} (\mathbf{d^{pred}} - \mathbf{d^{obs}}) \right\|^2 \tag{3.3}$$

where $\mathbf{d^{obs}} = \frac{1}{\sigma_\mathbf{j}}$, and $\sigma_\mathbf{j}$ is the estimated uncertainty associated with the j^{th} datum that encompasses measurements errors, discrepancies between the mathematical representation of the earth and the real earth, and other errors. Often, it's assumed they are Gaussian and independent.

The term ϕ_d is the data misfit [1] and is a measure of how well the data predicted by a given model reproduce the observed data. Given a certain model and through application of physics equations, the data that would fit to the model is evaluated ($\mathbf{d_{pred}}$). This procedure is called forwarding modelling and is represented by $\mathbf{F}(\mathbf{m})$

With a "selection rule" defined, it is necessary to define a tolerance value, such that if the misfit is about equal to that value, then the predicted data is fitting well the observed data. Suppose that σ_j are known and that errors are Gaussian. Then ϕ_d becomes the chi-squared variable χ^2_N with N degrees of freedom [73]. This is a well-known statistical quantity whose expected value is $E[\chi^2_N] = N$ and the standard deviation is $\sqrt{2N}$. The inverse problem can be formulated as the optimization of an objective function that takes into account all the requirements. The objective function can be expressed by:

$$\phi = \phi_d + \lambda\phi_m \tag{3.4}$$

The goal is to find the model m that minimizes ϕ_m subject to $\phi_d = \phi_d^*$, where ϕ_d^* is the tolerance or target misfit. If the assumptions of Gaussian errors are valid, a good estimation for the target misfit is $\phi_d^* \approx N$. The parameter λ is called the trade-off parameter and is a balance between the misfit, ϕ_d and the regularization, ϕ_m. The term ϕ_m is the regularization term (also known as stabilizer) and brings to the inversion the prior information required to transform the ill-posed problem into a well-posed problem. As mentioned before, this term will allow selecting one solution between all the solutions that exist. ϕ_m can take many shapes and will be discussed in section 3.2.

3.2 Regularization

Despite all the forms that the stabilizer can take, its goal is always the same: to select the desired stable solution from a class of solutions with specific physical and/or geometrical properties [116]. The stabilizer brings to the inversion algorithm some information about the properties of the solution that is known a priori, for example, if the kind of data in study usually reproduces smooth(or sharp) boundaries.

Although there are many regularization methods (e.g., Damped SVD/GSVD, Maximum entropy, Truncated Total Least Squares) will be focused on Tikhonov regularization, where the goal is to minimize the stabilizer. Some possible stabilizers are given below:

- Minimum Norm
$$\phi_m = \|\mathbf{m} - \mathbf{m_{ref}}]\|^2 \tag{3.5}$$
- Quadratic
$$\phi_m = \|\mathbf{Wm}\|^2 \tag{3.6}$$
- Minimum norm of the gradient (maximum smoothness)
$$\phi_m = \|\nabla\mathbf{m}\|^2 \tag{3.7}$$
- Total Variation
$$\phi_m = \|\nabla\mathbf{m}\|_{L_1} = \int_v |\nabla\mathbf{m}|\, dv \tag{3.8}$$

[1] distance between the observed data and the calculate data

- Total Variation Modified

$$\phi_m = \int_v \sqrt{|\nabla \mathbf{m}|^2 + \beta^2} \quad dv \tag{3.9}$$

- Minimum Support

$$\int_v \frac{(\mathbf{m} - \mathbf{m_{ref}})^2}{(\mathbf{m} - \mathbf{m_{ref}})^2 + \varepsilon^2} \quad dv \tag{3.10}$$

- Minimum Gradient Support

$$\int_v \frac{\nabla \mathbf{m} \cdot \nabla \mathbf{m}}{\nabla \mathbf{m} \cdot \nabla \mathbf{m} + \varepsilon^2} \quad dv \tag{3.11}$$

- Exponential

$$\sum_{j=1}^{N_m} \quad e^{|m_j|^2} \tag{3.12}$$

- Exponential modified

$$\sum_{j=1}^{N_m} \quad 1 - e^{-\left|\mathbf{m_j} - \mathbf{m_j^{ref}}\right|} \tag{3.13}$$

To exemplify the importance of the choice of the stabilizer, an example where synthetic crosswell travel-time tomography data is inverted with three different stabilizers: Minimum Support (MS), Minimum Norm (MN), and Exponential[2] is given. During the inversion, as the reference model, a homogeneous model with slowness equal to the background slowness has been used. In addition, the inverted data have been corrupted with a 1% Gaussian noise. Figure 3.1 shows the true model (a), and the inverted model for each stabilizer: (b) Minimum Support (MS), (c) Minimum Norm (MN), and (d) Exponential. It's clear the influence of the choice of the stabilizer on the resulting inverted model, the MS reproduces a sharp image while in the MN the resulting model is smoother. According to the shape of the desired target, the stabilizer should be chosen to reproduce blocky or smooth boundaries.

[2]The exponential stabilizer intend to generate a focused inversion image avoiding the process of selecting the focusing factor and calculation the model gradient [114]

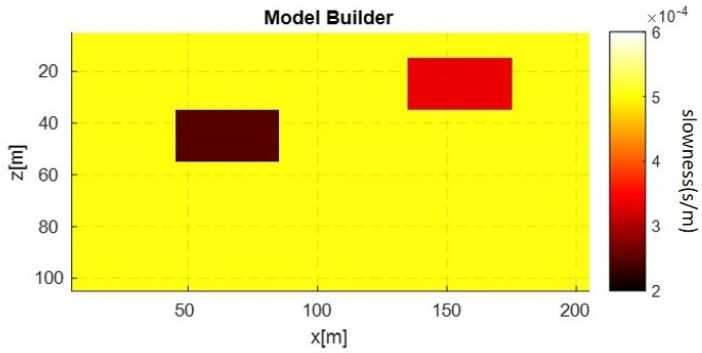

(a) Model 1

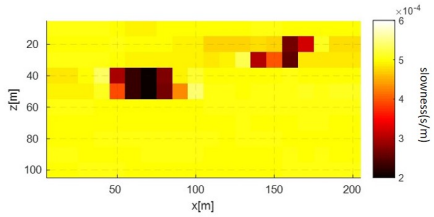

(b) MS

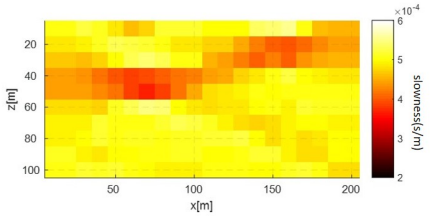

(c) MN

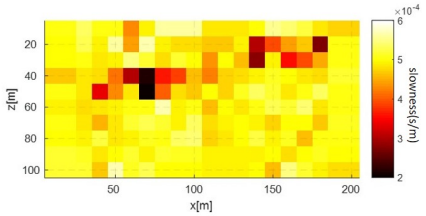

(d) Exponential

Figure 3.1: True model and model recovered by the inversion of crosswell travel-time tomography with the minimum norm (MN), minimum support (MS) and exponential stabilizers

Chapter 4

Inversion of seismic surface waves data

4.1 Tunable sparse inversion

This section describes the implementation of a regularized 1D inversion of SSW data promoting solution with a tunable sparsity leve and is based on the published article *"Reconstruction, with tunable sparsity levels, of shear wave velocity profiles from surface wave data"* [103].

4.1.1 Introduction

Seismic surface waves are increasingly used to infer geological units. As explained in chapter 2.2 the inversion of dispersion curves are an ill-posed problem, and can provide innumerous solutions. In chapter 3, it was explained a way to deal with the ill-poseness of the problem through introduction of a regularization term. This section presents an adjustable stabilizer based on the minimum support regularization, that has been applied on the inversion of other geophysical measurements, but never on surface wave data. The stabilizer is tested on synthetic and real data sets: (i) two synthetic data sets at crustal and near-surface scales (publicly available [42]) and (ii) an experimental data set collected on a well-characterized site.

It is also discussed a possible strategy for the estimation of the depth of investigation. This strategy relies on the integrated sensitivity kernel used for the inversion and calculated for each individual propagation mode.

The inversion of dispersion curves is a typical ill-posed problem and the associated ambiguity is tackled with different kinds of regularizations. Many of these strategies are based on smoothing regularizations accomplished via the penalization of the L2-norm of a roughening operator applied to the model parameter vector.

Alternative inversion methodologies are based on stochastic approaches; for example, [110], [24] and [67]. In general, these latter strategies have several advantages compared to the deterministic ones. For example, they are capable to explore more effectively the model parameter space and, by doing so, to naturally provide a more comprehensive estimation of the uncertainty of the result. However, their main drawback is still the computational cost. Thus, at least in the (more and more common) case of large data sets [95], it is highly desirable to have a fast inversion tool that, at the same time, is flexible enough to incorporate a large class of different kinds of prior information.

The present study evaluates a modification of a 'standard' L2-norm approach that, instead of selecting the smoothest possible solution, promotes 'sparse' reconstructions (of course, all equally compatible with the observations). The 'sparse´ nature of the result is actually variable, since the final model can be smooth depending on the choice of the focusing parameter ζ, which brings the strength point of this stabilizer: by tuning this parameter, one can obtain results with variable degree of sharpness/smoothness. The main difference between the standard L2-norm regularization and the proposed sparse strategy is that, whereas the first favours solutions with the smallest spatial variations of the shear wave velocities, the latter is selecting the model characterized by the smallest number of model parameters in which the velocity variations occur (regardless of the actual amount of the variation). The proposed deterministic inversion approach is based on the minimum support regularization. Recently, other strategies, making use of L1-norm regularizations have been applied to dispersion curve data for the reconstruction of blocky solutions [26, 41]. However, here, it should be emphasized the flexibility of the minimum support approach capable of retrieving shear wave velocity profiles with an adjustable level of sparsity. The performances of the novel tunable approach is demonstrated in three examples. The effects of the choice of the free parameter characterizing the proposed regularization and how, in principle, it can be used to explore the model parameter space is discussed. The synthetic data sets are at very different scales and deal with the inversion of different numbers of propagation modes. The conclusions are verified by applying the proposed inversion strategy to the real data set collected for geotechnical investigations on a well-characterized site.

In the literature, there are several examples of the applications of this type of regularization on different geophysical measurements; just to mention few examples: travel-times [1, 106, 116], electrical resistivity tomography [32, 74], electromagnetic observations [27, 60, 104, 115] and gravimetric measurement [59]. However, the present research is the first attempt at dealing with seismic surface waves. In addition, to facilitate the interpretation of the results, it is developed the analysis in Haney and Tsai [42] and described a possible approach for the assessment of the depth of investigation associated with each mode of propagation.

4.1.2 Theory

Inversion Scheme

In studying the surface wave propagation in layered systems, a crucial problem is the determination of the dispersion curves given the elastic properties of the subsurface. This problem is highly nonlinear and can be addressed in several ways as discussed in chapter 2.2. Nevertheless, independently from the forward modelling formulation used, the corresponding inverse problem can be solved via an iterative process making use of local linearizations of the original problem [117]. As discussed in detail in [2] and [42], the linear relationship between the relative perturbations in the phase velocity $\mathbf{V_R}$ and in shear wave velocity $\mathbf{V_S}$ can be expressed as

$$\frac{\delta \mathbf{V_R}}{\mathbf{V_R}} = K \frac{\delta \mathbf{V_S}}{\mathbf{V_S}} \tag{4.1}$$

where K is the shear wave velocity kernel (as presented in Eq. 2.36), and $\mathbf{V_R}$ and $\mathbf{V_S}$ are two vectors, as the first is evaluated over many frequencies (and, possibly, several

modes of propagation), whereas the latter consists of the velocities of the numerous layers used for discretizing the subsurface.

Under the frequent assumptions of a constant density model and a fixed Poisson's ratio, K is simply twice the sum of the kernels for the shear modulus and Lamé's first parameter. These common assumptions are justified, for example, by parametric analyses confirming that phase velocities are mainly affected by the shear wave velocity distributions [112] and that the mass density is characterized by limited ranges and impacts [50].

Consistently, Poisson's ratio is, in general, considered known. A homogeneous Poisson's ratio is reasonable, especially for deep investigations [26, 113], whereas, for shallower explorations, the effect of the saturation on compressional-wave velocity (and, in turn, on Poisson's ratio) can be significant; in these cases, for example, the depth of the water-table should be taken into account for the proper assessment of the Poisson's ratio variability [35]. The examples discussed in the present paper are all performed accordingly to these two above-mentioned hypotheses concerning the homogeneous mass density and constant Poisson's ratio.

From 4.1, it is easy to see that the linear Jacobian operator, locally mapping the shear velocity onto the phase velocity, is

$$\frac{\delta \mathbf{V_R}}{\delta \mathbf{V_S}} = J = diag(\mathbf{V_R})\, K\, diag(\mathbf{V_S})^{-1} \tag{4.2}$$

in which diag($\mathbf{V_R}$) is the square diagonal matrix with the non-zero entries equal to the elements of $\mathbf{V_R}$, and, similarly, $diag(\mathbf{V_S})^{-1}$ is the inverse of the diagonal matrix having as diagonal the vector $\mathbf{V_S}$.

Thus, within the inversion scheme described in chapter 3, the objective function to be minimized is

$$\phi(\mathbf{V_S}) = \left\| \mathbf{W_d}(\mathbf{V_R^{obs}} - \mathbf{F}(\mathbf{V_S^n})) \right\|^2 + \beta \left\| \mathbf{W_m}(\mathbf{V_S^n} - \mathbf{V_S^{ref}}) \right\| \tag{4.3}$$

where $\mathbf{V_R^{obs}}$ represents the observed data set, $\mathbf{F}(.)$ is the nonlinear forward modeling operator (whose Fréchet derivative calculated in ${\mathbf{V_S}}^{n-1}$ is $\mathbf{J}$), $\mathbf{V_S^{ref}}$ is the reference (and, in our case, also, the initial) model, and $\mathbf{W_d}$ and $\mathbf{W_m}$ are the weighting matrix for the data and the model vectors, respectively. The goal is to find, after n iterations, the shear wave velocity update $\delta\mathbf{V_S^n}$ minimizing the objective function given by Eq. 4.3. In this work, the number of iterations n is dynamically defined as the number of iterations necessary to reach a stationary point characterized by no significant variations in the value of the objective functional resulting from Eq. 4.3.

$\mathbf{W_d}$ is related to the data covariance $\mathbf{C}$, and, in our case, by assuming mutually independent data, it can be considered equal to

$$\mathbf{W_d} = diag(\sigma_\mathbf{d})^{-1} = \mathbf{C}^{-1/2} \tag{4.4}$$

where the i^{th} component of the vector $\sigma_\mathbf{d}$ is the standard deviation of the phase velocity associated with the i^{th} frequency.

If $\mathbf{W_m}$ is set as a discrete approximation of the spatial derivative (in 1D model), $L = \nabla = \frac{\partial}{\partial z}$, then, Eq. 4.3 provides the standard Minimum Gradient Norm (MGN) solution. In the case of a homogeneous reference model $\mathbf{V_S^{ref}}$ (i.e. in the case of a spatial variation of the reference model $\mathbf{V_S^{ref}}$ being zero everywhere), the MGN solution is characterized by the minimum velocity variations between the adjacent layers of the subsurface parameterization (strictly speaking, the MGN stabilizer guarantees the uniqueness of the

solution only if the forward problem is linear. Clearly, this is not the case when dealing with dispersion curve inversion. Thus, in this circumstance, the previous statement must be considered true only locally).

If, instead, $\mathbf{W_m}$ is chosen to be

$$\mathbf{W_m} = diag(\mathbf{W_e})\mathbf{L} \tag{4.5}$$

with

$$\mathbf{W_e} = \frac{1}{\sqrt{\mathbf{L}(\mathbf{V_S^n} - \mathbf{V_S^{ref}}) + \zeta^2}} \tag{4.6}$$

then, we are dealing with the Minimum Gradient Support (MGS) [116]. In the case of a homogeneous reference model, the MGS solution is characterized by the minimum number of parameters (i.e. layers) where a significant velocity variation between the adjacent layers occurs (again, strictly speaking, the same caveat concerning the uniqueness of the MGN solution is valid also for the MGS stabilizer). So, compared to the MGN, in the MGS, what matters is not the amount of the variation, but, rather, the number of parameters where a significant variation takes place [100]. A velocity variation contributes significantly to the MGS regularization term in Eq. 4.3 every time it is large compared to the threshold defined by the focusing parameter ζ [101]. Thus, as it will be clear from the numerical examples in the following, a strategy for the selection of the optimal ζ value can consist of setting the focusing parameter value in the order of magnitude of the velocity changes we are interested to investigate. In principle, the focusing parameter ζ can be a vector and, in this way, depth-dependent sparsity of the solution can be enforced. For sake of simplicity, in the present research, we consider all the components of such a vector equal to ζ; that is, $\zeta = \zeta\mathbf{1}$. In the described inversion scheme, the Tikhonov parameter β can be potentially chosen in many ways—for example, through the L-curve strategy [30]. Since the data uncertainty was accessible in the available test data sets, we select β in order to guarantee a chi-squared value

$$\chi^2 = \frac{\left\|\mathbf{W_d}(\mathbf{V_R^{obs}} - \mathbf{F}(\mathbf{V_S^n}))\right\|^2}{N_d} \tag{4.7}$$

approximately equal 1 (with N_d being the number of measurements [100]).

It might be worth looking at the proposed tunable approach from a Bayesian perspective. In that framework, the goal is to study the posterior probability density function $p(\mathbf{V_S}|\mathbf{V_R^{obs}})$ measuring the probability of having the model $\mathbf{V_S}$ compatible with the measurements V_R^{obs}. Accordingly to the Bayes' theorem, $p(\mathbf{V_S}|\mathbf{V_R^{obs}})$ is proportional to: i) the prior probability density function for the model parameters $p(\mathbf{V_S})$, and the conditional probability density function $p(\mathbf{V_R^{obs}}|\mathbf{V_S})$. The latter connects the measured data and the model parameters, and, in the specific case of Gaussian noise distribution, it can be written as

$$p(\mathbf{V_R^{obs}}|\mathbf{V_S}) = k_d\, e^{-(\mathbf{V_R^{obs}} - F(\mathbf{V_S}))^T \mathbf{W_d}^T \mathbf{W_d} (\mathbf{V_R^{obs}} - F(\mathbf{V_S}))} \tag{4.8}$$

where k_d is merely a normalization factor. If also the model parameters are assumed to follow a Gaussian distribution, then, the prior information about the solution can be formalized as follows:

$$p(\mathbf{V_S}) = k_m\, e^{-(\mathbf{V_S} - \mathbf{V_{S}}_{ref})^T \mathbf{W_m}^T \mathbf{W_m} (\mathbf{V_S} - \mathbf{V_{S}}_{ref})} \tag{4.9}$$

in which (i) k_m is another normalization factor and (ii) the Gaussian is centred on the reference model $\mathbf{V_S^{ref}}$. By comparing the posterior probability density function $p(\mathbf{V_S}|\mathbf{V_R^{obs}}) \propto p(\mathbf{V_R^{obs}}|\mathbf{V_S})p(\mathbf{V_S})$ and the objective functional $\left\|\mathbf{W_d}(\mathbf{V_R^{obs}} - \mathbf{F}(\mathbf{V_S^n}))\right\|^2 + \beta\left\|\mathbf{W_m}(\mathbf{V_S^n} - \mathbf{V_S^{ref}})\right\|$ minimized by the system of equations in 4.3, it is evident that the proposed deterministic MGN algorithm is designed to search for the maximizer of the $p(\mathbf{V_S}|\mathbf{V_R^{obs}})$ via linearized steps with the assumption of a Gaussian distribution of the data noise and of the variation of the model. Along the same line of reasoning, the MGS can be seen as related to the assumption of a model variation distribution that is still Gaussian, but with a standard deviation $\mathbf{W_e^{-1}}$ that is, iteration by iteration, locally defined. In particular, such a standard deviation tends to the constant value ζ, anywhere the associated variation of the model update $\Delta\mathbf{V_S}^n = \mathbf{V_S}^n - \mathbf{V_S}^{ref}$ is small with respect to ζ, whereas it is proportional to the variation of $\Delta\mathbf{V_S}^n$, whenever the model update itself is large compared to the threshold (defined by ζ). That is why, during the inversion, large variations are all penalized (approximately) by the same amount, no matter how big they are (in fact, large variations are associated with proportionally large standard deviations, and their penalization is, in any case, close to 1), whereas small variations of the model update are penalized depending on their departure from 0 with respect to the ζ value.

Clearly, for the MGN stabilizer, the model covariance is assumed to be such that $\mathbf{C_m^{-1}} = \beta^2\mathbf{L^T L}$, whereas, for the MGS, the relation $\mathbf{C_m^{-1}} = \beta^2\mathbf{L^T L}/(\Delta(\mathbf{V_S}^n)^T\mathbf{L^T L}\Delta\mathbf{V_S}^n + \zeta^2)$ is valid.

Of course, the convenience of the deterministic local inversion algorithm, even if computationally cheaper than the global counterpart, comes with a price. In fact, compared with global approaches [119], the proposed scheme starts from an initial guess, which is also the reference model $\mathbf{V_S^{ref}}$ (i.e. our best guess), and searches in the direction obtained by the neighborhood derivative; in doing so, the local strategy leads to a minimum that is close to the initial guess and that, in principle, might not be the global optimum. However, it is important to highlight that, usually, the convergence to the global minimum cannot be claimed within a finite time even for the global techniques [71]. Luckily, in the inversion of surface wave dispersion curves, a quite good (at least, homogeneous) starting model can be deducted from direct observation of the data. In fact, the maximum phase velocity can be considered a reasonable estimation of the final maximum shear wave velocity; therefore, generally, the proposed deterministic local approach should be able to perform quite well anytime proper starting models are selected based on an easy preliminary analysis (calculation of the maximum) of the observed data.

Concerning the assumption of a diagonal data covariance C, clearly, it is a modeling simplification and, most likely, the effectiveness of the proposed scheme can be improved by including, for example, an estimation of the error introduced by the 1-D interpretation of the dispersion curves. Indeed, this additional piece of information might be incorporated into the covariance matrix (under the assumption that also the modeling error is Gaussian) by simply defining a new covariance matrix $\mathbf{C}'$ as the summation, $\mathbf{C}' = \mathbf{C}+\mathbf{C_\Delta}$, of the original term C of Eq. 4.4 and an assessment of the modeling error $\mathbf{C_\Delta}$ [97]. For example, the additional covariance $\mathbf{C_\Delta}$ can be calculated statistically by performing a number of accurate forward simulations taking into account the higher dimensionality of the real problem and comparing the associate responses with those of the 1-D forward modeling used for the actual inversion [7, 44, 66, 118].

Depth of investigation

The Depth of Investigation (DOI) can be defined as the depth below which the data collected at the surface are not sensitive to the ground velocities. Hence, the DOI provides a rough estimation of the maximum depth that can be reliably investigated from the surface (given a specific frequency range, the number of considered modes, and, clearly, the physical properties of the medium).

A DOI assessment can be based on empirical relations relying on the longest wavelength in the data [76]. Alternatively, the study of the variability of the solution as function of the starting model can provide good indications of the sensitivity of the data to the velocity values inferred at depth. So, for example, [34] discusses the possibility of inverting the data with different initial velocity models and comparing the results to determine if they are data- or model-driven.

Similarly to [63], the approach used here is based on the integrated sensitivity matrix [117]. Hence, the DOI in the following examples is defined as the depth where, for each propagation mode, the normalized integrated sensitivity value drops by 70 dB.

The rationale behind this is that the variation $\delta[\mathbf{V_R}]_i = \delta[F(\mathbf{V_S})]_i$ — induced on the i^{th} phase velocity value by the perturbation $\delta[\mathbf{V_S}]_k$ of the k^{th} component of shear-velocity—is $\mathbf{J_{ik}}$ (if the linearized problem is considered). Thus, the overall influence of the perturbation of the k^{th} model parameter on the norm of the data vector is $[\mathbf{S}]_k = \sqrt{\sum_i (\delta[\mathbf{V_R}]_i)^2} = [\sqrt{\mathbf{J^T J}}]_k$. Therefore, the various components of the integrated sensitivity vector $\mathbf{S}$ quantify the influence of a specific shear-velocity layer on the observed data. When $[\mathbf{S}]_k$ reduces significantly, the reconstruction should be no longer assumed data-driven. This is the depth where the DOI can be set. Hence, the DOI collapses the $\mathbf{S}$ information content in one number (actually, in one number for each data subset since we are possibly dealing with more than one propagation mode). Definitely, in the operative definition of DOI, the selection of the 70 dB threshold is quite arbitrary, and it has been decided a-posteriori based on some numerical tests. In any case, the same threshold has been applied across all the discussed inversions; so, at least, it can provide a consistent term of comparison.

4.1.3 Results

Following the approach in [42], two synthetic data sets are inverted to demonstrate the capabilities of the two regularization strategies considered in this paper and defined by the two alternative choices for the model weight $\mathbf{W_m}$ in the previous section.

Crustal scale example

The first example concerns the inversion of the first two modes of propagation for a crustal-scale problem. The frequency range of the data spans between 0.1 and 0.65 Hz. The shear-velocity model to be reconstructed (Fig. 4.1, solid blue line) is characterized by a $\sim$ 2.2 km thick low-velocity zone, centered at around 3 km depth. Apart from this shallow velocity inversion, the shear velocity profile shows an increasing velocity from 2.3 to 3.5 km s^{-1}, with an intermediate step at 2.6 km s^{-1}. Accordingly to [42], the data were contaminated with 2.5 % of noise on both modes (Fig. 4.2, blue vertical bars).

The novel MGS($\beta = 5 \cdot 10^{-2}$; $\zeta = 10^2$) reconstruction is shown in Fig. 4.1(a) and is supposed to be compared with the 'standard' MGN ($\beta = 5 \cdot 10^{-8}$) result in Fig. 4.1(b). Both these inversions have a χ^2 value around 0.93. So, they are equally compatible with

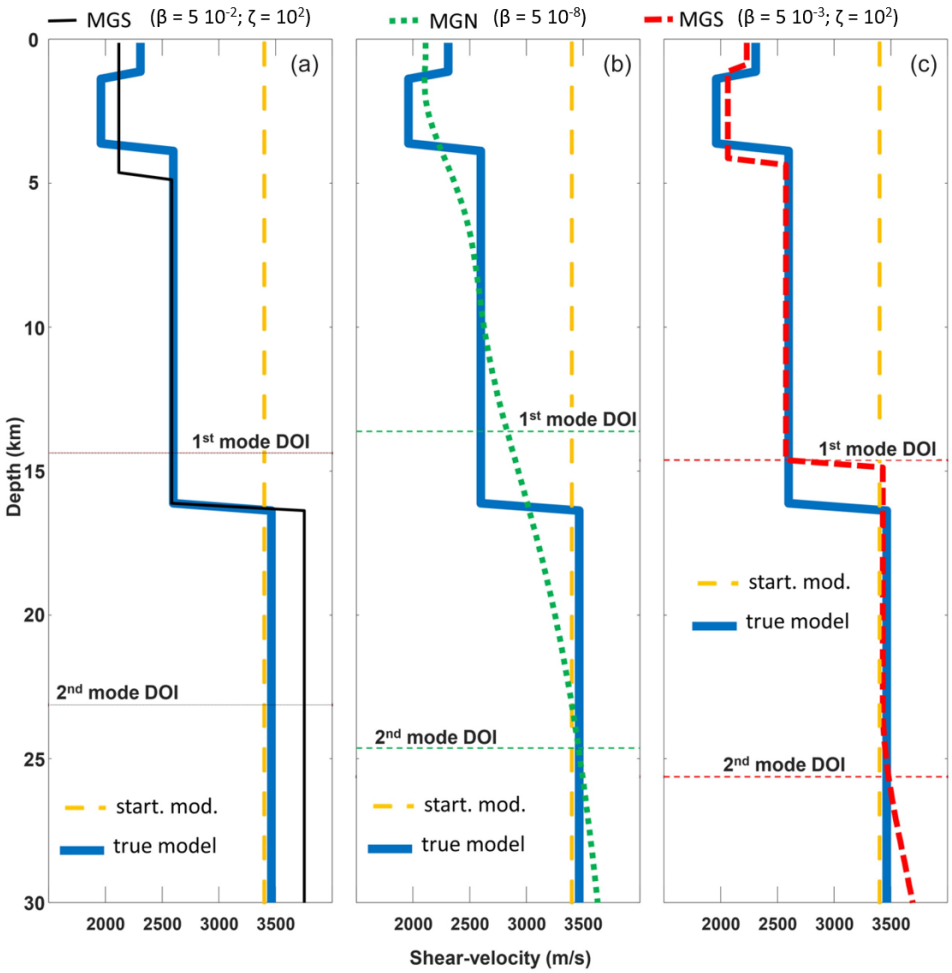

Figure 4.1: Shear wave velocity profiles related to the first numerical test (the crustal scale example). The solid thick blue line in all panels is the true model, whereas the dash orange line is the starting/reference model $\mathbf{V_S^{ref}}$. Panel (a) shows the MGS reconstruction (solid black line) that can be consistently compared with the MGN result (dash green line) in panel (b) as they have compatible data misfit ($\chi^2 \sim 0.93$). In panel (c), the MGS result with a smaller β (and, coherently, with a lower χ^2 value: 0.81) is plotted (dash red line). For all three cases, the depth of investigation (DOI) of each propagation mode is shown. All the inversion models consist of 240 layers of constant thickness (250 m) and the solutions are reached, respectively, in 69 (a), 5 (b), and 83 (c) iterations.

the data and in good agreement with the estimation of the noise level. Nevertheless, they show quite different features. In particular, despite the fact that both inferred models lack retrieving the shallow velocity inversion, this first MGS ($\beta = 5 \cdot 10^{-2}$; $\zeta = 10^2$) inversion can better identify the presence of sharp interface at around 4 km, and its velocities are very close to the true model down to 16 km (including the location of the velocity change at 16.3 km depth). This MGS ($\beta = 5 \cdot 10^{-2}$; $\zeta = 10^2$) inversion overestimates, by approximately 8 %, the velocity of the last 3.5 km/s layer. This is not surprising as that layer lies in the depth interval between the two DOIs (Fig. 4.1a). In this case, the plot of the normalized integrated sensitivity (Fig. 4.3) demonstrates the potential risks connected with a too rigid interpretation of the DOI value: even if the sensitivity decay associated with the fundamental mode reaches the 70 dB threshold above the abrupt velocity change

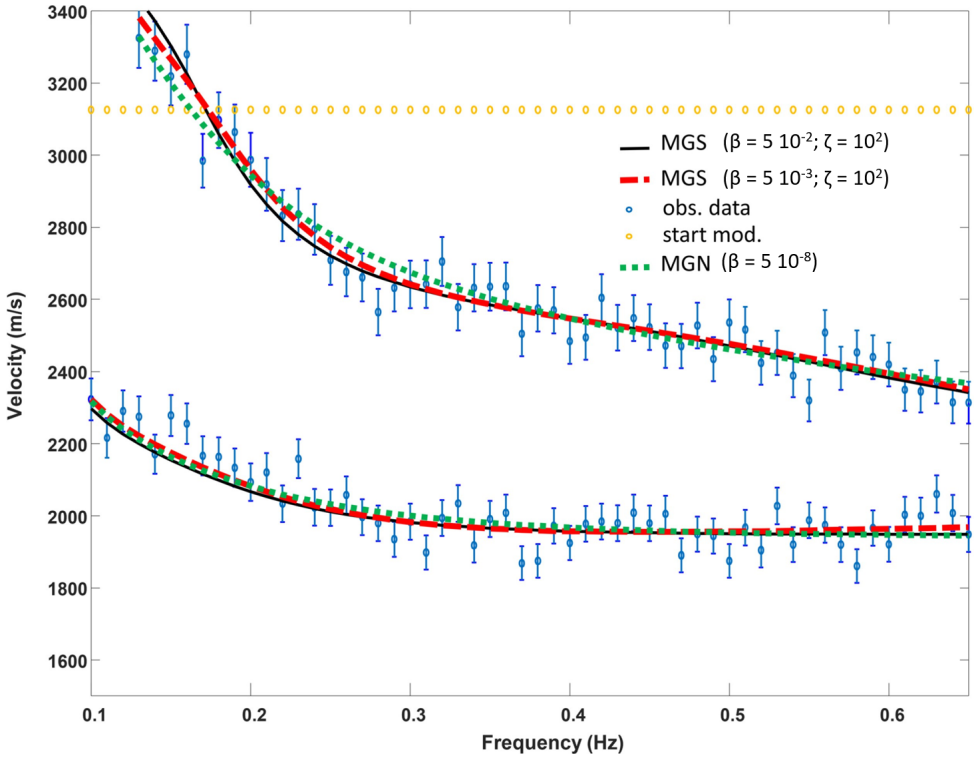

Figure 4.2: The observed (blue circles with the associated error bars) and calculated data for the three inversion results in Fig. 4.1. The data from the MGS and MGN results with comparable χ^2 values are plotted with a solid black and a dot green line, respectively, whereas the 'overfitting' response obtained with the MGS (and a smaller β) is represented by the dash red line. The orange circles are the data generated by the homogeneous starting model.

(in fact, the 1st DOI is set to ∼15 km depth), the dramatic variation of the sensitivity actually occurs at the interface located at ∼16 km; so, whereas the reconstruction above the abrupt (velocity/sensitivity) change can be considered reliable (even below the first DOI), the inferred velocity value for the last layer should be taken with more caution. On the other hand, the DOI for the MGN reconstruction is safer to be interpreted directly since, by definition, no sharp velocity (and in turn, sensitivity) changes are introduced (Fig. 4.4). Besides, this sensitivity analysis confirms that higher modes can be very valuable in bringing additional information at depth. The sensitivity decay is, indeed, less pronounced for the overtones, in particular, even below sharp transitions, where the fundamental mode sensitivity diminishes very rapidly.

Actually, the estimation of the originally provided noise might have been too conservative. In fact, by reducing the value of β, we can get the result in Fig. 4.1(c), in which the true model is effectively reconstructed (including the shallow velocity inversion) by the MGS ($\beta = 5 \cdot 10^{-3}$; $\zeta = 10^2$) algorithm. The corresponding χ^2 is around 0.81. The only appreciable differences between the latest MGS result and the true model are (i) the 9 % underestimation of the depth of the deepest velocity variation and (ii) an increasing velocity at the bottom of the profile. Both these differences occur below the sudden decrease of sensitivity (Fig. 4.5). Reaching the same level of data fitting (i.e. $\chi^2 \sim 0.81$) with the MGN regularization was not possible. This is in agreement with the fact that, through the MGN regularization, we try to enforce prior information in contrast with the actual blocky nature of the true model [97].

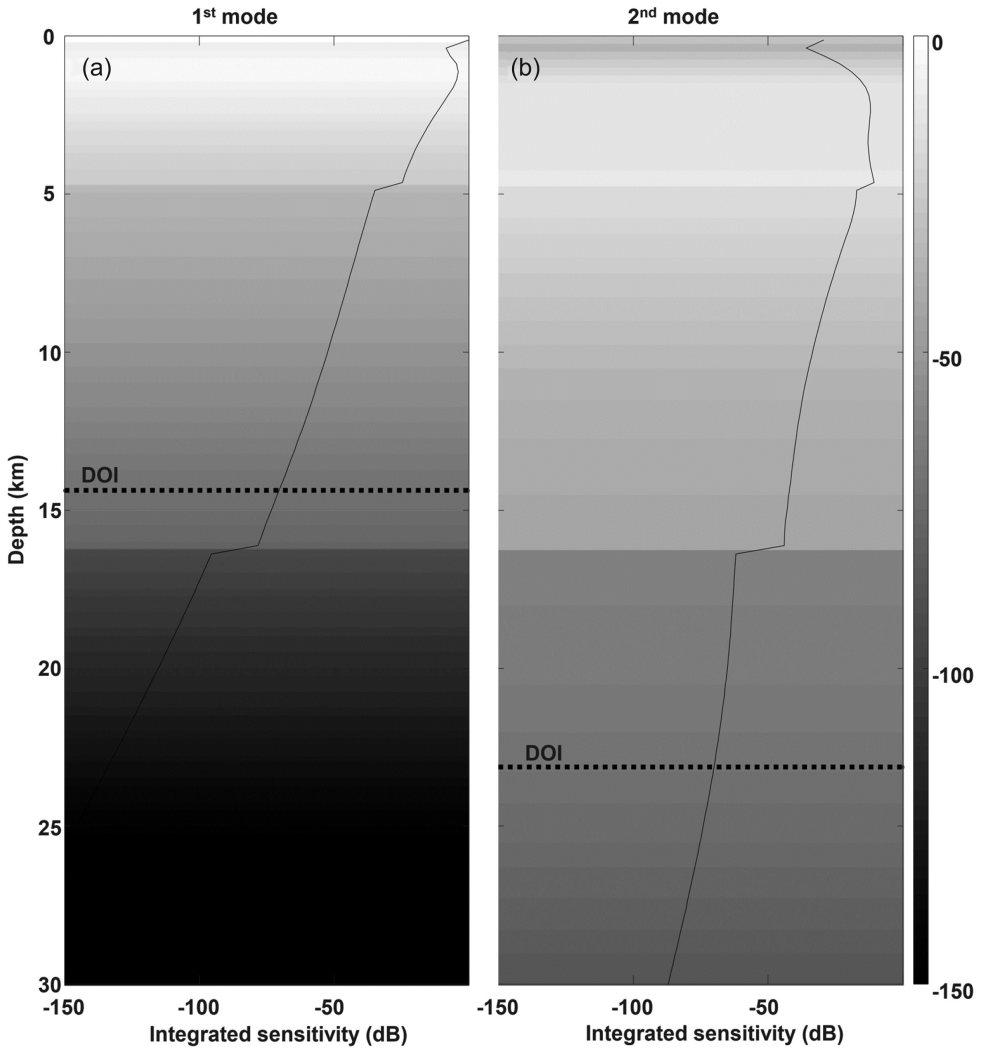

Figure 4.3: Integrated sensitivity and estimation of the DOIs for the MGS ($\beta = 5 \cdot 10^{-2}$; $\zeta = 10^2$) solution in Fig. 4.1(a). Panels (a) and (b) show respectively the normalized integrated sensitivity for the fundamental mode and the first overtone. The DOI lines indicate at which depth the sensitivity drops by 70 dB.

Results similar to the MGS inversions in Figs 4.1(a) and (c) can be probably obtained with a few layers parameterization. However, in practice: (i) it is hard to know in advance the appropriate number of layers for the correct parameterization and (ii) the layer number might not be constant over a large survey with many adjacent acquisition locations (potentially requiring continuous supervised adjustments of the inversion settings). On the contrary, all the inversions discussed in this example are performed with layers with constant thickness (0.25 km). This provides a very flexible tool for the inversion of surface wave data in complex (blocky) geological settings, in which (i) the regularization parameter β is selected by the discrepancy principle (in general, $\chi^2 \sim 1$) and (ii) the focusing parameter ζ is chosen accordingly to the expected sparsity level. In this respect, for this first experiment, we use $\zeta = 10^2$ since we are targeting shear-velocity variations of that order of magnitude; clearly, velocity variations of the order of few hundreds of meters per second can be considered significant (and penalized by the stabilizer), not only as they characterize the true model, but, in general, because they are the variation range relevant

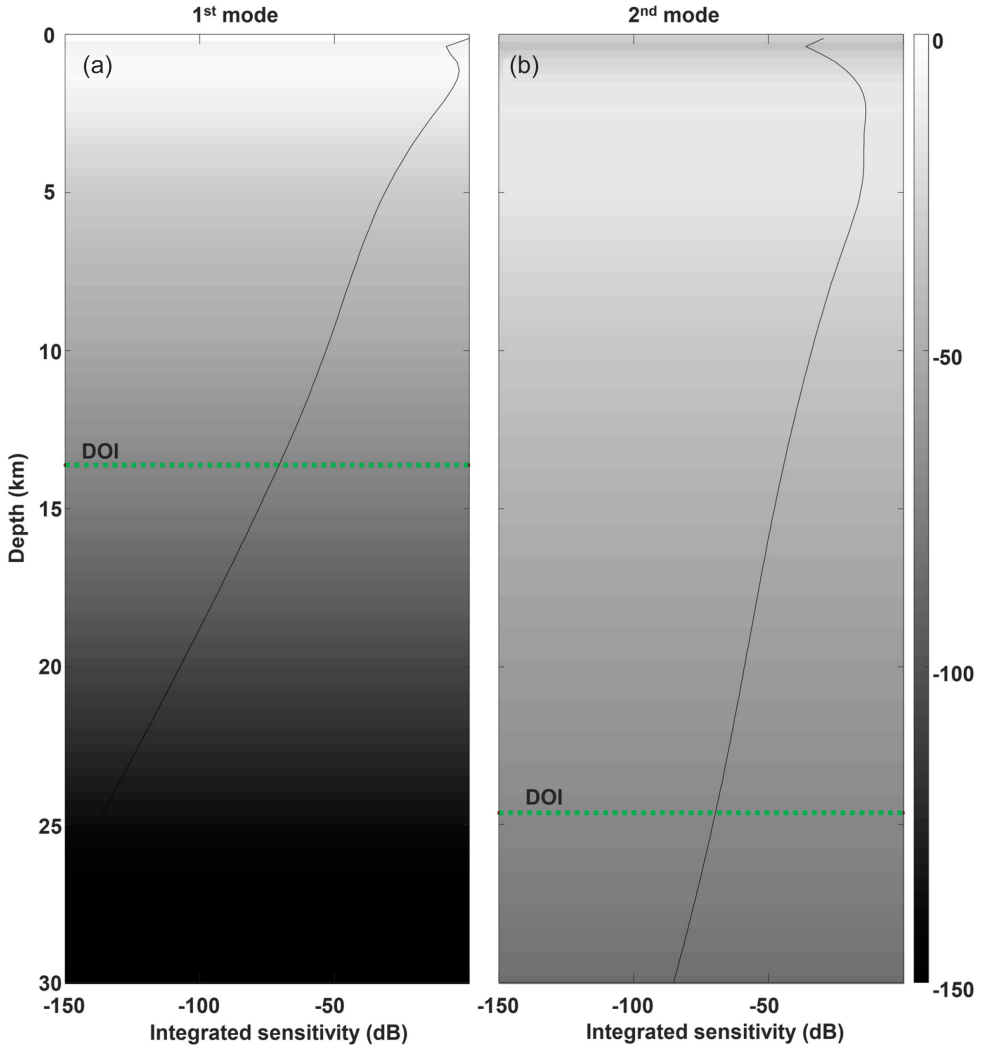

Figure 4.4: Integrated sensitivity and estimation of the DOIs for the MGN solution in Fig. 4.1(b). Panels (a) and (b) show respectively the normalized integrated sensitivity for the fundamental mode and the first overtone. The DOI lines indicate at which depth the sensitivity drops by 70 dB

for the (crustal) scale of the problem we are dealing with.

By changing the focusing parameter ζ, we can effectively control the level of sharpness of the result. For example, Fig. 4.6 shows the comparison of the results obtained with three different values of ζ (but, of course, similarχ^2 values; Fig. 4.7). With respect to the first inversion generated with $\zeta = 10^2$ (Figs 4.1c and 4.6b), as expected, a smaller value of ζ ($\zeta = 5$, in Fig. 4.6c) produces more numerous abrupt changes characterized by smaller mutual velocity differences (with $\zeta = 5$, the velocity jumps are of the order of tens of m/s); if, instead, we increase ζ ($\zeta = 10^3$, in Fig. 4.6a), we can get a smoothly varying vertical profile since only the variations larger than the threshold defined by the focusing parameter will be penalized significantly. This shows how the MGS regularization can be effectively used in a deterministic framework to generate a wide range of solutions characterized by different levels of sparsity by means of a simple modification of the value of the focusing parameter.

For this test, an extensive study of the sensitivity of the final inversion with respect to the starting/reference model has not been performed and a homogeneous velocity (

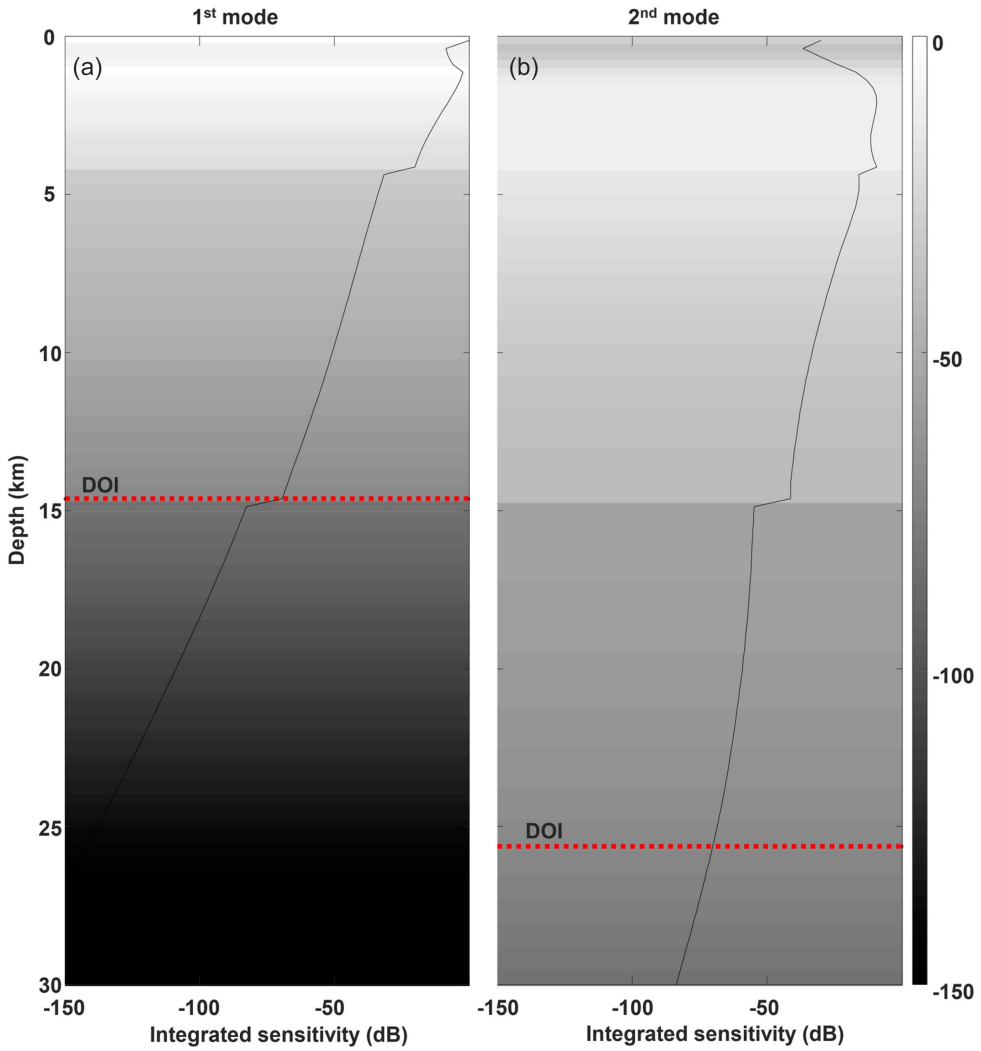

Figure 4.5: Integrated sensitivity and estimation of the DOIs for the MGS ($\beta = 5 \cdot 10^{-3}$; $\zeta = 10^2$) solution in Fig. 4.1(c). Panels (a) and (b) show respectively the normalized integrated sensitivity for the fundamental mode and the first overtone. The DOI lines indicate at which depth the sensitivity drops by 70 dB.

$[\mathbf{V_S^{ref}}]_k = 3.4$ km/s, $\forall k$) has been always used. However, as both (MGS and MGN) definitions include a derivative operator, we do not expect big impacts on the velocity values per se. In addition, even if starting from a model with a shape close to the real one would be, for sure, beneficial (even just in terms of convergence speed), it seems (Figs 4.1 and 4.6) that the proposed approach can effectively handle quite arbitrary (i.e. distant from the actual solution) starting models.

Near-surface example

The second synthetic example consists of the near-surface model MODX discussed in [19, 42, 112]. As described in [42], the data associated with this model were generated with 2 % noise, but, differently from that study, here, we use a homogeneous parameterization with 0.4 m-thick layers. By considering relevant for this test simply the velocity variations larger than a few meters per second, the value of the focusing parameter ζ for the MGS inversion has been chosen equal to 5 (corresponding to expected velocity variations of $\sim$12

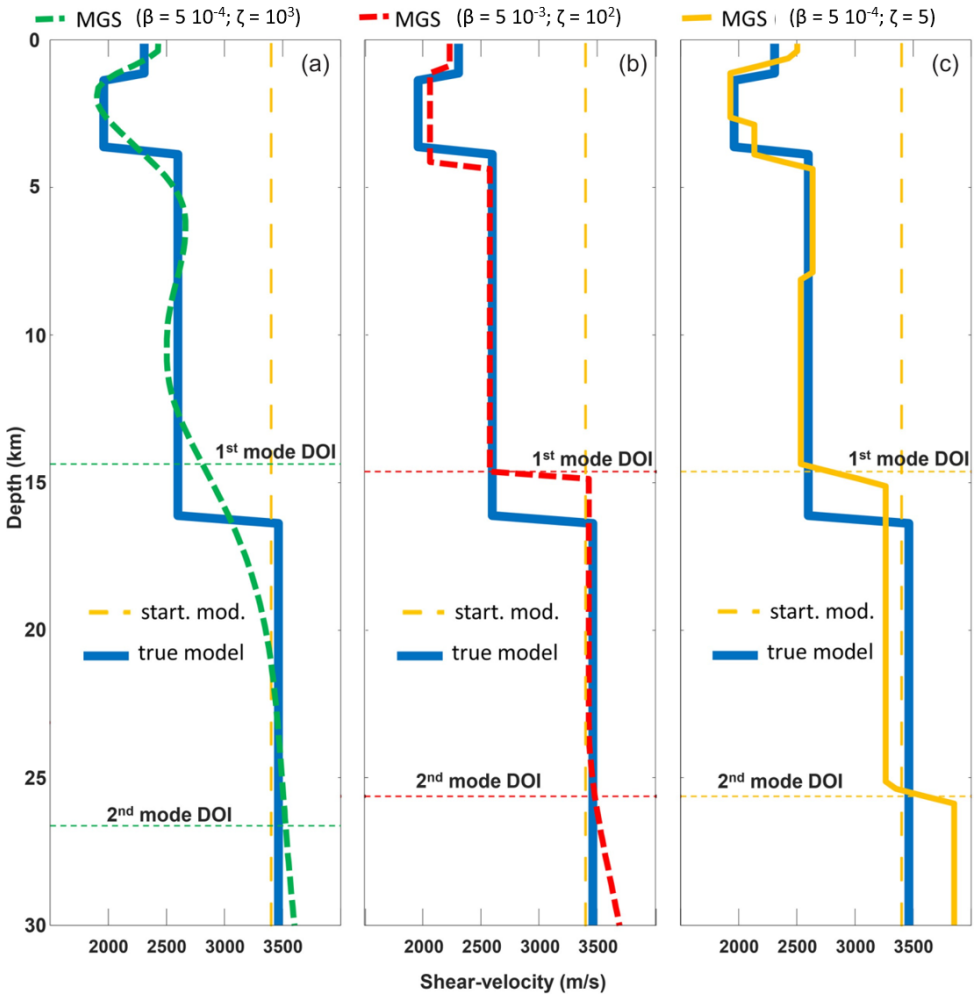

Figure 4.6: Comparison of three MGS results for the first (crustal scale) example. Each of them is characterized by a different choice of the focusing parameter ζ: (a) $\zeta = 1000$; (b) $\zeta = 100$; (c) $\zeta = 5$. All the inversion models consist of 240 layers of constant thickness (250 m) and the solutions are reached, respectively, in 7 (a), 83 (b) and 1572 (c) iterations. Of course, the data misfit for all three inversions is similar: $\chi^2 \sim 0.81$

m/s over a 1 m thickness). The corresponding result is plotted in Fig. 4.8(a), whereas the MGN result with comparable data fitting (Fig. 4.9) is showed in Fig. 4.8(b). Both results are very good in retrieving the overall gradually increasing velocity profile. Nevertheless, the MGS performs better in inferring the discontinuity at around 13 m depth and the velocity of the last layer. In addition, even if it is not capable to retrieve all the small velocity variations (at least at this data fitting level: $\chi^2 \sim 0.81$), the MGS model is more successful in following the little shallow velocity steps.

With respect to the crustal example, here, the DOIs inferred by the MGS and MGN solutions look quite different (Fig. 4.10). However, as before, this is mainly due to the fact that the DOI concept, despite being useful for its immediacy (critical, e.g. in case of large surveys), cannot entirely convey the complexity of the sensitivity dependence with depth. A proper interpretation of the DOI value should take into account also the velocity profile. In the specific case, it is clear, that, also for the MGS result, the sensitivity variation with depth is very limited below 15 m as, below that level, the velocity (and sensitivity) is

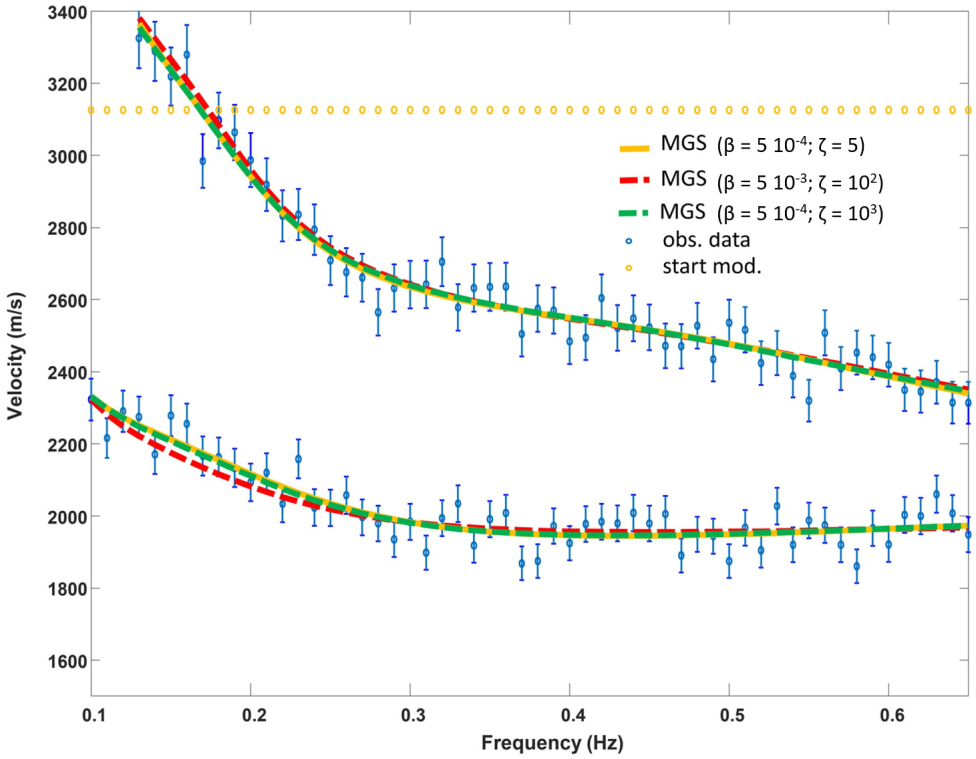

Figure 4.7: The observed (blue circles with the associated error bars) and calculated data for the three inversion results in Fig. 4.6. The orange circles are the data generated by the homogeneous starting model.

almost constant. So, the 25 m difference between the MGN's and the MGS's DOIs is merely due to the choice of the DOI threshold value and it is not really meaningful per se. As before, an analysis based on the integral sensitivity (and not just the DOI) can, instead, lead to a more correct interpretation (Fig. 4.10).

Geotechnical field test

We further verify the proposed tunable sparsity approach on an experimental data set collected over a site characterized by the following lithological sequence (Fig. 4.11d):

i 0.0 to 0.3 m—clay till;

ii 0.3 to 1.5–2.0 m—artificial soil;

iii 1.5–2.0 m to ∼10 m—till;

iv deeper than approximately 10 m—bedrock.

The geological settings are typical of the shallow subsurface around Lund (Sweden). However, in this specific case, the first 1.5– 2.0 m have been altered. In particular, the original unit between 0.3 and 1.5–2.0 m have been substituted with artificial soil, and, consequently, also the most superficial layer (0–0.3 m) has been reworked.

The proposed tunable stabilizer behaves as expected. Hence, as for the synthetic example at crustal-scale, also for this experimental test, by decreasing the value of ζ, we obtain shear wave velocity reconstructions characterized by an increasing level of sparsity. Fig. 4.11 shows three different solutions resulting from the application of ζ spanning a

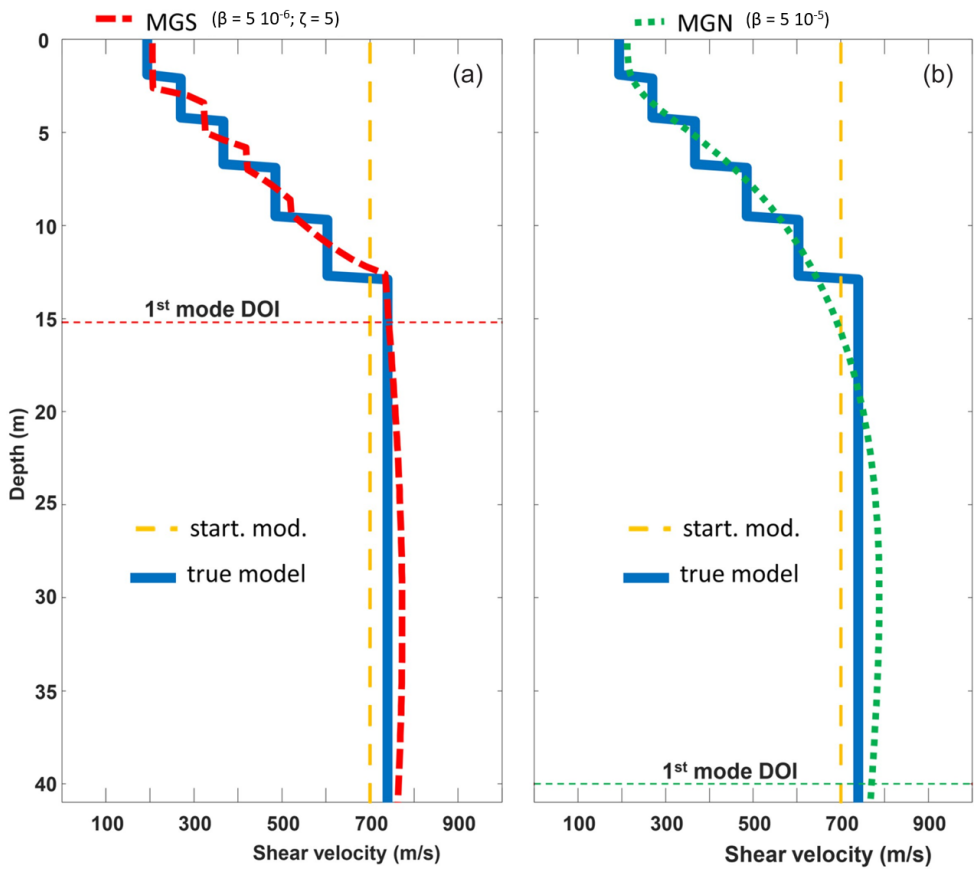

Figure 4.8: Shear wave velocity profiles related to the second numerical test (the near-surface example). The solid thick blue line in all panels is the true model, whereas the dash orange line is the starting/reference model $\mathbf{V_S^{ref}}$. Panel (a) shows the MGS reconstruction (dash red line) that can be consistently compared with the MGN result (dot green line) in panel (b) as they have compatible data misfit ($\chi^2 \sim 0.81$). For all two cases, the DOI for the fundamental propagation mode is shown. Both inversion models consist of 400 layers of constant thickness (0.4 m) and the solutions are reached, respectively, in 228 (a) and 13 (b) iterations.

wide range of values (from 6 to $9 \cdot 10^{-2}$). The parameterization consists of layers with a homogeneous thickness of 0.05 m; consistently, the selected ζ values result to be sensitive to velocity changes of the order of, respectively, 120, 12, and 1.8 m/s over a meter. All the results in Fig. 4.11 fit the data equally well as shown in Fig. 4.12 (the corresponding χ^2 values range between 0.45 and 0.50) and all of them capture the velocity inversion at 0.3 m and detect the top of the bedrock.

However, the two sparsest solutions correctly retrieve the thickness and location of the till layer. This is particularly true for the solution with ζ equal 0.6 (Fig. 4.11b), which, in fact, is sensitive to the most reasonable velocity change interval for the scale of interest of this specific test.

Concerning the DOI estimation, all three results in Fig. 4.11 provides approximately the same depth. It is interesting to see that, at depth (below the DOIs), the solution is influenced uniquely by the starting model and is no longer sensitive to the data. In this specific test, the DOI value can be considered a reliable estimation of the depth at which the results stop being data-driven as the integrated sensitivity does not drop abruptly at

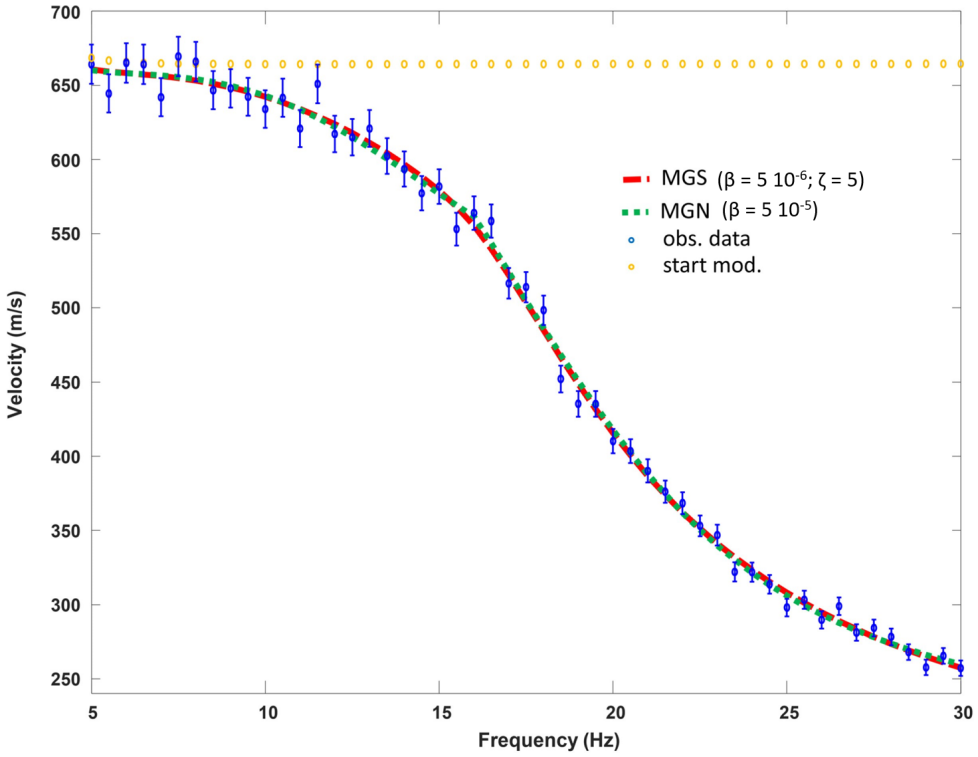

Figure 4.9: The observed (blue circles with the associated error bars) and calculated data for the two inversion results in Fig.4.8. The orange circles are the data generated by the homogeneous starting model.

a sharp velocity change, but rather cross the 70 dB threshold smoothly (Fig. 4.13).

Choice of the starting model, inversion robustness and reliability of the DOI assessment

We use the experimental data to further analyze the dependence of the retrieved solution with respect to the choice of the starting (and reference) model $\mathbf{V_S^{ref}}$. It is worth recalling that a reliable and easy to get an estimation of the shear wave velocity at depth is clearly provided by the value of the phase velocity at low frequencies as it can be immediately obtained by looking at the dispersion curves (e.g. in Fig. 4.12). Hence, we inverted the experimental data by using exactly the same settings except for the choice of the starting/reference model. More precisely, Fig. 4.14 shows the results of the inversion performed with $\beta = 5 \cdot 10^{-7}$; $\zeta = 0.6$ (as for Fig. 4.11 and homogeneous starting velocities equal, respectively, to 400, 500 and 600 m/s. Clearly, also, in this case, the three results correspond to very close data misfits ($\chi^2 \sim 0.5$; see Fig. 4.15). The almost perfect overlapping of the solutions above the DOIs confirms the effectiveness of the proposed algorithm: for a reasonable range of starting velocities, the solution is stable with respect to the choice of the inversion parameters.

Besides, this test proves, once more, also the validity of the suggested DOI assessment (and, in particular, the reasonability of the 70 dB threshold). In fact, the three solutions begin to be significantly different below the DOIs, where each of them is highly affected by the specific choice of the starting model and not, anymore, by the data. Actually, as discussed for example in [72], the DOI could be assessed by performing several inversions and checking where the solutions are mainly dependent on the starting model (and not on the data). This alternative approach for the estimation of the DOI, despite being much

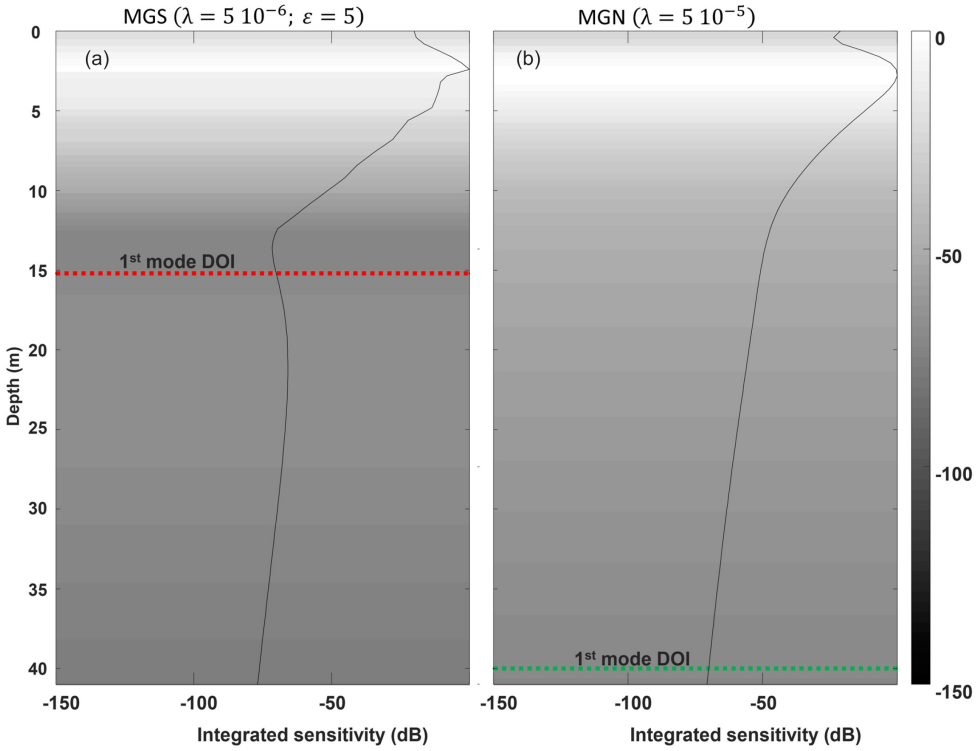

Figure 4.10: Integrated sensitivity and estimation of the DOIs for the solutions in Fig. 4.8. Panels (a) and (b) show respectively the normalized integrated sensitivity for the MGS and the MGN regularization. The two DOI lines indicate at which depth the sensitivity drops by 70 dB.

more computationally expensive as it involves multiple inversions, might have (similarly to the proposed analysis of the integrated sensitivity) the advantage of further highlighting, not only at which depth the solutions start not being data-driven, but, also, if there are shallower 'blind spots' (where the sensitivity of the model to the data is lower).

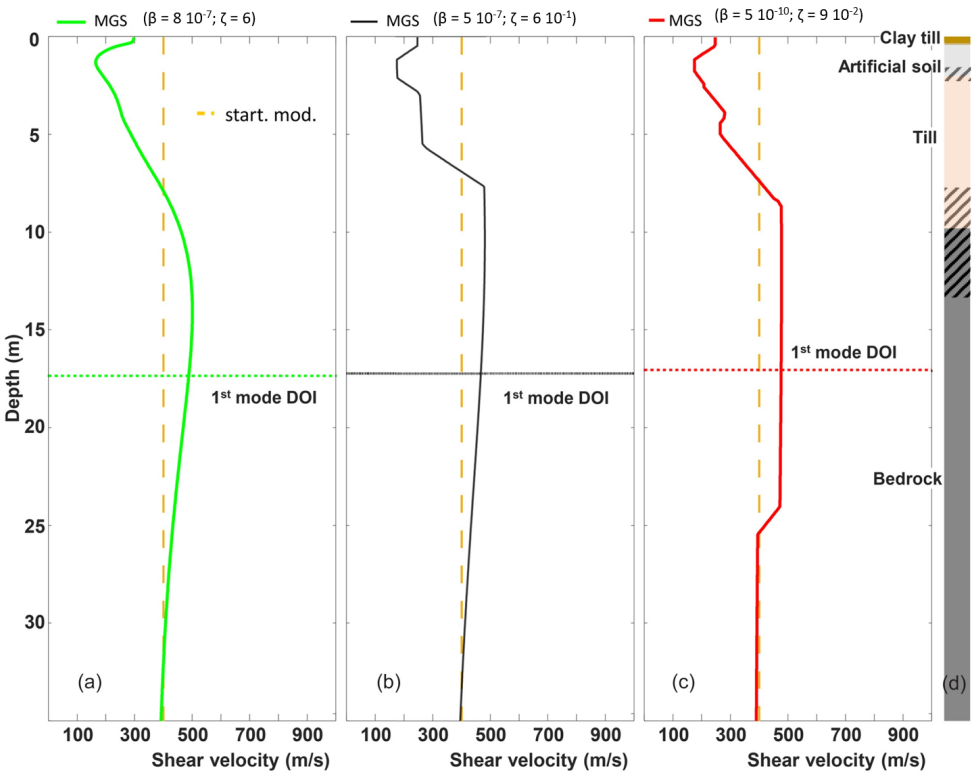

Figure 4.11: Shear wave velocity profiles retrieved from the data of the geotechnical experimental test. The green (a), black (b) and red (c) curves represent the solutions obtained with the MGS stabilizer and decreasing values of ζ (hence, increasing sparsity). All the solutions are characterized by χ^2 values between 0.45 and 0.50. The dash orange line is the starting/reference model $\mathbf{V_S^{ref}}$. In (d), the lithological sequence of the site is also shown (the dashed areas between 1.5 and 2.0 m and around 10 m represent the uncertainty related to the bottom interface of the artificial soil layer and the top of the bedrock). All models consist of 1000 layers of constant thickness (0.05 m) and the solutions are reached, respectively, in 18 (a), 13 (b) and 1788 (c) iterations.

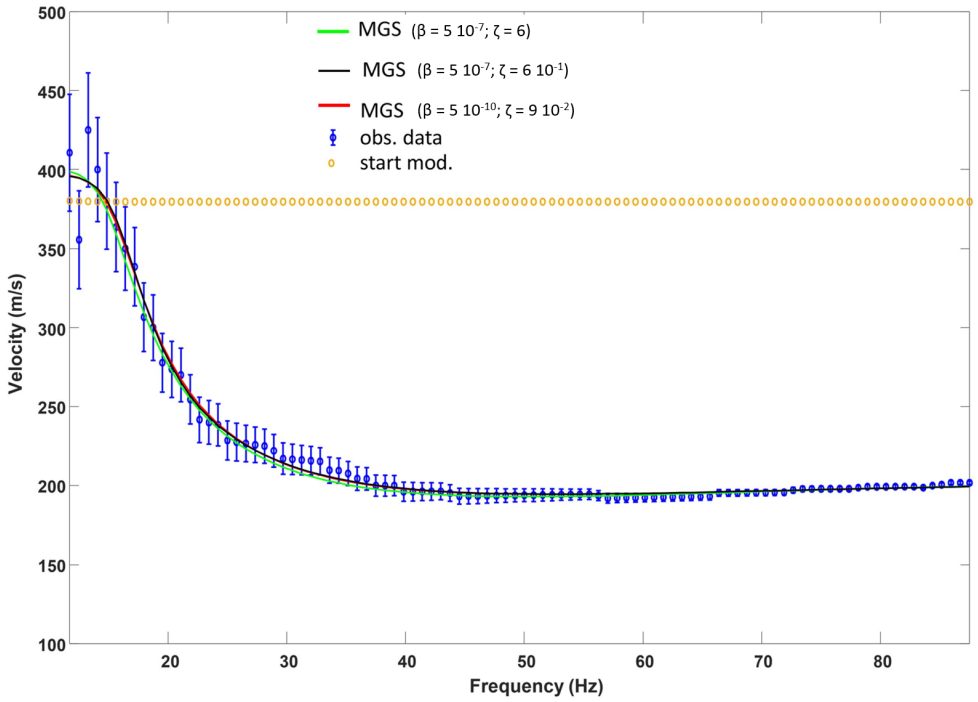

Figure 4.12: The observed (blue circles with the associated error bars) and calculated data for the three inversion results in Fig. 4.11. The orange circles are the data generated by the homogeneous starting model.

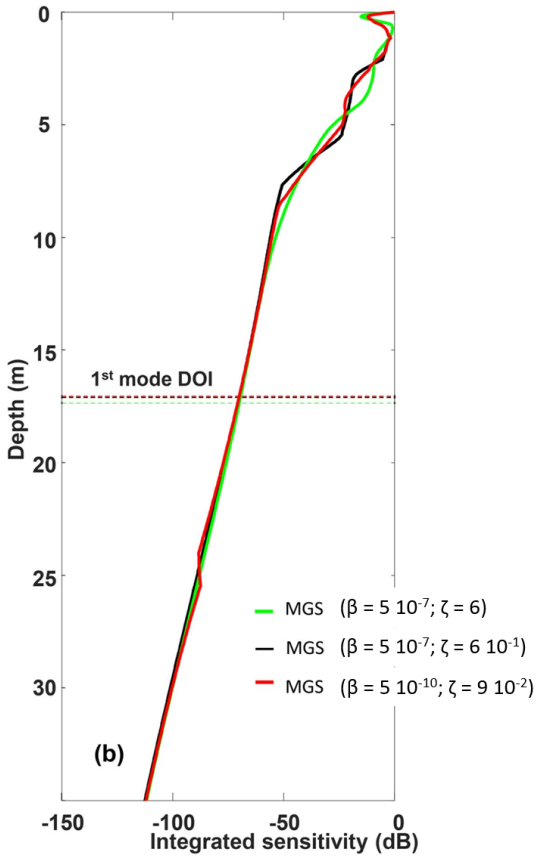

Figure 4.13: Integrated sensitivity profiles and estimation of the DOIs for the solutions in Fig. 4.11

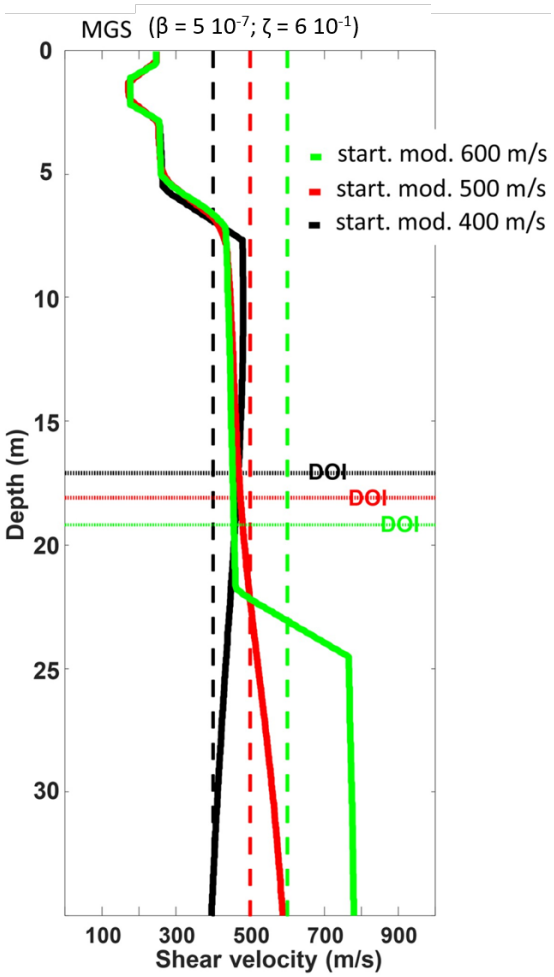

Figure 4.14: Shear wave velocity profiles retrieved from the data of the geotechnical experimental test. The green, red and black curves represent the solutions obtained with the MGS stabilizer with the same settings used to obtain the result in Fig. 4.11(b). The only difference between the three velocity profiles shown here is the starting/reference model. Together with the inversion results (solid lines), also the (homogeneous) starting models are shown (vertical dash lines) and the associated DOIs (horizontal dot lines). All the solutions are characterized by χ^2 values about 0.5 (Fig. 4.15). All inversions are obtained with the same model parameterization consisting of 1000 layers (0.05 m thick); the solutions are reached, respectively, in 75 (black), 51 (red), and 95 (green) iterations.

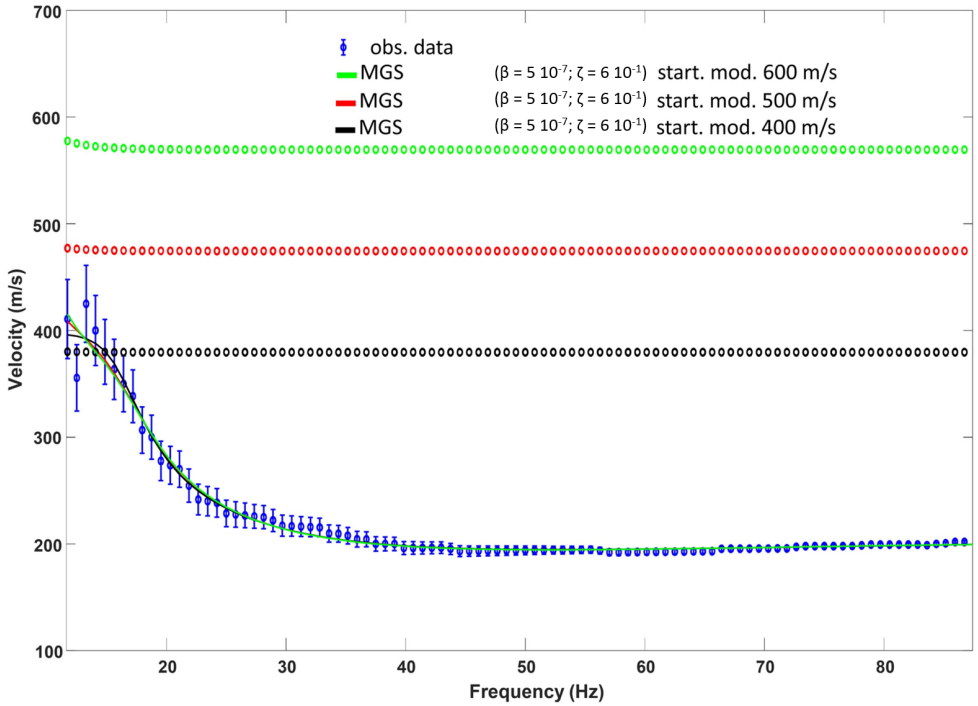

Figure 4.15: The observed (blue circles with the associated error bars) and calculated data for the three inversion results in Fig. 4.14. The black, red, and green circles represent the data generated by the homogeneous starting models.

4.1.4 Conclusions

It was applied, for the first time to the inversion of surface wave dispersion curves, a tunable regularization based on the minimum gradient support. In particular, we provide practical suggestions on how to select the free parameters involved in the definition of this kind of regularization and demonstrate the capabilities of this inversion scheme in retrieving solutions, equally compatible with the observations, but characterized by different sparsity levels. So, by selecting the appropriate focusing parameter value, we can effectively span the solution space. We first test the proposed approach on two synthetic—publicly available—benchmark data sets; they are about very different scales of application: from crustal to near-surface studies. Moreover, we verify the proposed strategy on an experimental data set collected for geotechnical purposes on a well-characterized site and compare the results against the known lithology. In addition, aiming at a fair comparison of the results of the proposed tunable sparsity regularization, we push further some of the conclusions in [42] and discuss the effectiveness of a strategy for the assessment of the depth of investigation based on the integrated sensitivity. In this respect, we highlight possible drawbacks of direct interpretation of the depth of investigation value (or values, depending on the number of propagation modes actually inverted), especially when dealing with abrupt velocity changes.

4.2 Laterally constrained inversion

This section deals with an extension to the 2D case of the previous algorithm; more specifically, here the tunable sparsity regularization is applied in the framework of the spatially constrained inversion in with the stabilizer acts not only in the vertical direction, but, also, laterally (providing pseudo-2D reconstructions based on 1D forward). The text presented below is based on the submitted article *"Sparse laterally constrained inversion of surface wave dispersion curves via minimum gradient support regularization"* [39]

4.2.1 Introduction

This section discusses the extension of the previously described strategy - based on the MSG regularization to obtain 1D V_S reconstructions with tunable levels of sparsity - to the Laterally Constrained Inversion (LCI). In the LCI case, the regularization acts, not only vertically - for each sounding - but, also, laterally, between adjacent models. This allows the reconstruction of (pseudo-) 2D V_S sections with different levels of sharpness. The forward model is the same discussed before for the 1D sparse inversion. A particular aspect of the deterministic inversion procedure applied here is the fact that the data are inverted by considering a shear-wave velocities model in the log-space as it was noticed that the corresponding Jacobian shows less model dependency, hence reducing the likeliness of local non-convexity. The results demonstrate the effectiveness of the proposed approach in different environments and for a broad range of applications. Also in this case, the conclusions are drawn based on several synthetic and field data examples.

Very often, in the attempt of retrieving 2D/3D shear-wave velocity distributions, adjacent dispersion curves are inverted individually and simply stitched together afterward [102]. This approach is generally justified by the fact that, because the physics of the method and the implicit lateral averaging for the dispersion curve extraction, nearby dispersion curves cannot be too different even when the geology is. However, for example, in

the (to a large extend, similar) case of electromagnetic signals, mutually constraining close by soundings has been proved to be effective in enforcing lateral consistency and further reducing unwanted artefacts. In these cases, by still using 1D forward modelling, multiple adjacent soundings are jointly inverted with a stabilizing term bounding the corresponding 1D models laterally. This is the essence of the 1D LCI, developed initially in the framework of electric [5] and electromagnetic methods [4], and, later, applied also to surface wave data [91, 111]. The original LCI algorithms select solutions that are laterally smooth (in the sense of the L2-norm inversion), preventing the reconstruction of blocky structures characterized by constant physical parameters. To cope with this, MGS regularizations have been successfully tested on LCI schemes for the interpretation of electromagnetic data [101, 104]. In a similar line of reasoning, in the present research, we discuss the implementation of a LCI-MGS algorithm for the sparse inversion of the seismic surface wave dispersion curves. In particular, we first discuss the theoretical framework and the implementation details; then, we analyse the performances on synthetic and experimental data collected on a Norwegian test site.

4.2.2 Theory

Following the procedure explained in section 4.1.2, the objective function is slightly modified in this section, with the inversion been carried out to the $log(V_S)$.

The problem of inverting phase velocity data to reconstruct a shear-wave subsurface model is highly non-linear as clearly shown by Eq. 4.1 where the Jacobian is explicitly dependant on the $\mathbf{V_S}$ velocities (note that in addition, $\mathbf{K}$ is also dependant on $\mathbf{V_S}$). This can be a source of local non-convexity of the inverse problem making gradient-based nonlinear inversion approaches likely sensitive to the starting model [34]. Regarding this aspect, it was noted that the Jacobian associated with a shear-wave velocity model in the log-space shows a reduced model dependency as explicitly shown here

$$G_{ij} = \frac{\delta \mathbf{V_R^i}}{\delta log(\mathbf{V_S^j})} = \mathbf{V_S^j J_{ij}} \tag{4.10}$$

where the term log stands for the natural logarithmic function (basis e). In Fig. 4.16 a-b, illustrates this aspect by comparing the original Jacobian $J = \delta \mathbf{V_R}/\delta \mathbf{V_S}$ and the new $G = \delta \mathbf{V_R}/\delta log(\mathbf{V_S})$ for two local perturbations of a homogeneous medium. Following this observation, and in the attempt to reduce at best the likeliness of local non-convexity of the inverse problem, we suggest an inversion procedure with a model space corresponding to the logarithm of the shear-wave velocities. To do so, we use the iterative procedure introduced by [22], which for our case takes the form:

$$log(\mathbf{V_S}^{n+1}) = [\mathbf{G}^{(n)T}\mathbf{W_d}\mathbf{G}^{(n)} + \beta \mathbf{W_m}]^{-1}\mathbf{G}^{(n)T}\mathbf{W_d}[\mathbf{V_R} + \mathbf{G}^{(n)} log(\mathbf{V_S}^{(n)} - F(log(\mathbf{V_S}^{(n)})) \tag{4.11}$$

Differently from the case discussed in 4.1.2, and, instead, similarly to [22] and [55], the β value is varying during the minimization of the objective function. In particular, its value is automatically defined at each iteration by analyzing the χ^2 or Root Mean Square (RMS) misfit function, which we note $\phi_n(\beta)$ for a broad range of β values. In practice, at iteration n, our algorithm starts with the largest β value and decreases it until $-d\phi/d\beta > 0$ for which we set $\beta^n = \beta$. An example of such iterative β^n selection is given in Fig. 4.16c.

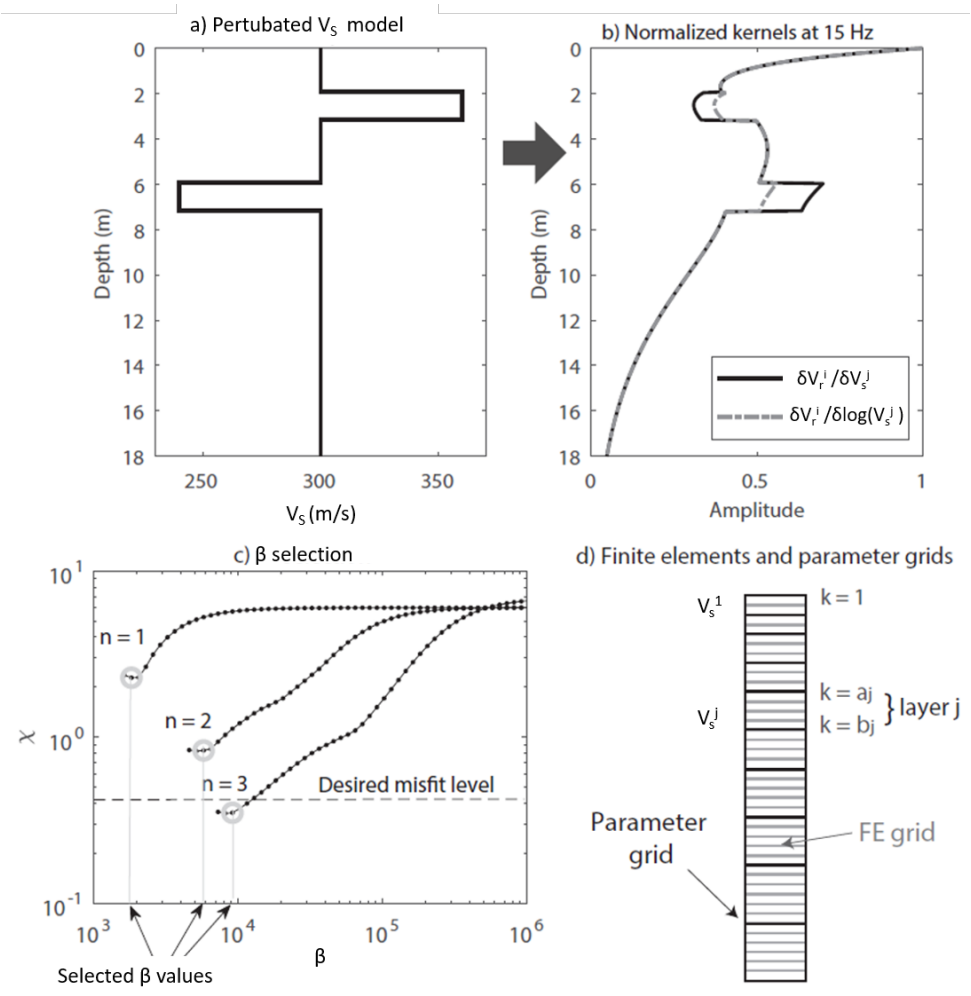

Figure 4.16: Description of the inverse modeling algorithm. a) Homogeneous subsurface background model with two local perturbations in shear-wave velocity. b) Comparison between **J** and **G** (Eq. 4.10) gradients computed for the model shown in a), and for the frequency f = 15 Hz. The results highlight how **G** is less dependent on the perturbations shown in a), which means that the related inverse problem is more comparable to a linear inverse problem. c) Strategy for selecting the model regularization weight at each iteration of the Occam procedure. d) Description of the decoupling between the FE grid used for forward calculations and the (coarser) parameter grid defined for the inversion.

As above mentioned, the forward modeling $\mathbf{F}(\mathbf{log}(\mathbf{V_S}))$ and the Jacobian $\mathbf{J_{ij}}$ from Eq. 4.12 are computed by using the same finite elements (FE) 1D approach utilized in 4.1 and discussed in detail in [37] and [59].

The forward modeling $\mathbf{F}(log(\mathbf{V_S}))$ and the Jacobian $\mathbf{J_{ij}}$ from Eq. 4.10 are computed with the 1D finite elements (FE) approach presented in [42] and based on [64]. In the context of inversion, for which the velocity model is not known in advance, it is difficult to optimally set the 1D grid according to the basic rules of thumbs associated with the FE methods (minimum size of the layers, minimum total extent of the grid). To ensure good precision and stability of the FE forward modelling during inversion, here, it was used a rather fine homogeneous grid with a rather large maximum extent (2-3 times the largest apparent wavelength of the observed c curve). However, even for (non-parametric) grid-

based deterministic inversion, it may not be desirable such a fine grid as it would result in an excessive number of parameters, hence resulting in rather large matrices to be inverted. Heterogeneous layer thickness (e.g., increasing with depth) can also be used, which may be an optimal choice for efficiently inverting dispersion curves recorded over a broad frequency range, and various subsurface velocity settings (e.g., when simultaneously inverting a full profile). Finally, we may use few layers only as for the case of a deterministic parametric inversion. In order to make our approach flexible in all these situations, we decouple the parameter grid used for the inversion from the FE grid used to compute the dispersion curves and the Jacobians. To do so, we define the layers j used for inversion as composed of a specific number of finite element sub-layers k as follows (see also Fig. 4.16d)

$$\mathbf{V_S}_k^{(n)} = \mathbf{V_S}_j^{(n)}, \qquad k \in [a_j, b_j] \tag{4.12}$$

where a_j and b_j are the first and last element of the j^{th} layer in the finer finite element grid. Accordingly, the elements of the Jacobian matrix are given by

$$\mathbf{G_{ij}}^{(n)} = \mathbf{V_S}_j^{(n)} \sum_{k=a_j}^{k=b_j} \mathbf{J_{ik}}^{(n)} \tag{4.13}$$

Following the same purpose of section 4.1.2, in order to be able to control the model sharpness, the stabilizer used at the laterally constrained inversion (LCI) is the minimum gradient support (MGS), in this case, the model weighting matrix takes the form of

$$\mathbf{W_m} = \mathbf{Q_z}^T \mathbf{Q_z} + \gamma \mathbf{Q_x}^T \mathbf{Q_x} \tag{4.14}$$

with

$$\mathbf{Q_{z,ij}} = \frac{\mathbf{L_{z,ij}}}{\sqrt{(\mathbf{L_z} log(\mathbf{V_S}^{(n)}))_j^2 + \zeta^2}} \qquad \mathbf{Q_{x,ij}} = \frac{\mathbf{L_{x,ij}}}{\sqrt{(\mathbf{L_x} log(\mathbf{V_S}^{(n)}))_j^2 + \zeta^2}} \tag{4.15}$$

where $\mathbf{L_z}$ and $\mathbf{L_x}$ are first or second-order differential operators applied to neighboring model elements in vertical and horizontal directions, respectively. The difference between the stabilizer presented in section 4.1.2 and the one presented here, is that the latter is applied not only vertically (z-direction) (as it was in section 4.1.2) but also laterally (x-direction), it doesn't use a reference model, $\mathbf{V_S^{ref}}$ and a logarithmic transformation is applied on the model space, $\mathbf{V_S} \rightarrow log(\mathbf{V_S})$.

In section 4.1.2 it was proposed a practical criterion for the choice of ζ and this parameter was used to define the threshold discriminating between small and large velocity variations in order to investigate features at different scales. Here, it is worth noting the benefit of using the logarithmic space shear waves velocities parameterization, also in the framework of the MGS regularization. Indeed, by considering the logarithm of the shear-wave velocities, the scale-dependency of the MGS operator is automatically removed and, in principle, the same range of ζ values can be used to explore the sharpness of the solutions no matter if we are dealing with problems at crustal scale or data collected for near-surface characterizations.

4.2.3 Results

Synthetic data example

Single Sounding Vertically Constrained Inversion(VCI)

Layer	V_P (m/s)	V_S (m/s)	ρ (kg.m^3)	h (m)
1	260	150	1.24	2
2	433	250	1.41	4
3	346	200	1.35	6
4	693	400	1.57	∞

Table 4.1: Model used for the single sounding synthetic tests; the shear-wave vertical distribution is equal to the one of "Model 2" in [26]

In order to better illustrate the most basic features of our inversion procedure, we first present a synthetic experiment considering single-sounding inversion, i.e., a vertically constrained inversion only. For this test, we select a subsurface layered shear-wave models similar to one discussed in [26], with a homogeneous V_P/V_S ratio and density relationship parameters (see Tab. 4.1).

The synthetic $\mathbf{V_R}$ data are computed for frequencies between 4 Hz and 50 Hz with a step of 2 Hz using a FE grid 200 m deep and characterized by 0.2 m thick layers. During the inversion, as described by Equations 4.12 - 4.13 and Fig. 4.16d: i) for the forward modeling $\mathbf{F}(log(\mathbf{V_S}^n)$ and the associated calculation of the Jacobian $\mathbf{J_{ik}}$, the same, fine, FE discretization has been used, whereas, ii) for the actual inversion parameterization, the FE discretization has been remapped into coarser ones (100 and 550 layers). We define the starting model as a homogeneous model of velocity equal to the mean of the dispersion curve

$$\mathbf{V_S}^{(n=0)} = \overline{\mathbf{V}}_\mathbf{R}$$

A noise-free synthetic experiment it is performed. For this test, the fictitious uncertainty level is set to 1% and a very small χ^2 value of 0.005 in order to force the algorithm to fit the data as much as it can. Figure 4.17 shows the results for two different parameter grids. The first is a rather dense grid of 550 layers with constant layer thicknesses; the second one is coarser with increasing thicknesses. Firstly, one can see that both inversions show a final mean χ value in the range 0.01, i.e., corresponding to a fit of around 0.01%, which is largely acceptable according to what is needed in most of the practical situations. Both grids allow an effective reconstruction of the true model via the MGS regularization with ζ value of 0.001 (Fig. 4.17a). The inversion with the fine homogeneous grid steadily converges across a larger number of iteration than the inversion with the coarse heterogeneous grid. This is expected from the fact the fine grid gives more model freedom for the algorithm to reconstruct the model almost perfectly.

We perform a second single-sounding inversion experiment for noisy synthetic data, by using the heterogeneous grid analyzed above, and by testing two extreme values for ζ. For these tests, uncorrelated $\pm$5% random noise was added to the dispersion curve. For the inversions, we set a constant standard deviation value of 5% and a very small χ^2 value for the same purpose as the first experiment. The results are shown in Fig. 4.18. We see that both inversions reach the desired misfit and provide consistent solutions, which are

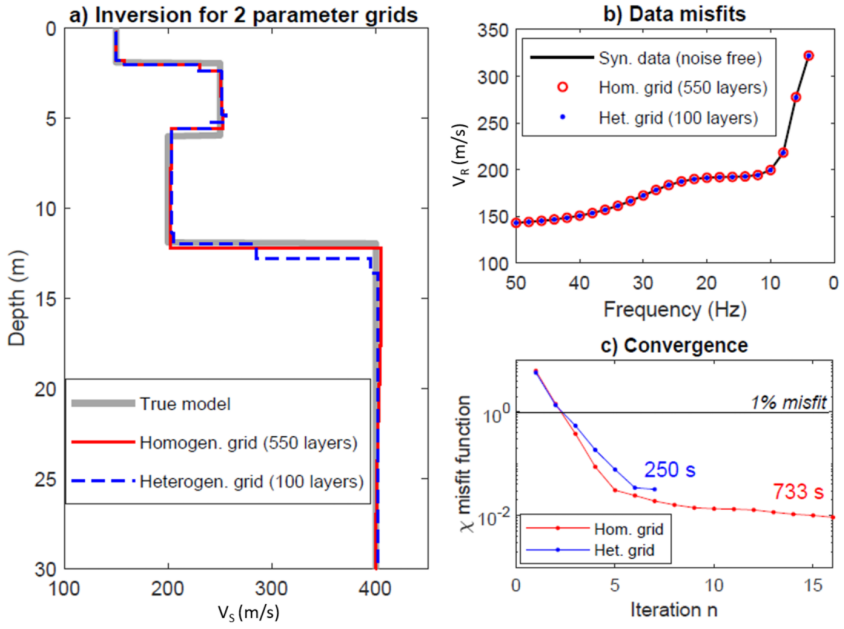

Figure 4.17: Noise free synthetic experiment with $\zeta = 0.001$ for two different parameter grids. a) Comparison between the models resulting from the inversions and the true model used for computing the synthetic data. b) Data misfits for the three tests. c) Evolution of the misfit during the iterative inverse procedure. Layer thickness in meter for the 2 grids from top to bottom: homogeneous grid of 550 layers up to a depth of 110 m [550×0.2 m], heterogeneous grid of 100 layers up to 110 m [10 layers of 0.2 m; 10 layers of 0.4 m; 10 layers of 0.6 m; 10 layers of 0.8 m; 10 layers of 1.0 m; 10 layers of 1.2 m; 10 layers of 1.4 m; 10 layers of 1.6 m; 10 layers of 1.8 m; 10 layers of 2 m].

a sharp model for $\zeta = 0.001$, and a smooth model for a large value $\zeta = 1$.

finally, it is applied this single-sounding VCI approach to a pseudo-2D profile composed of dispersion curves, computed for 50 layered models, which are stitched together afterward. The true layered models consist of the same 4 layers as the ones considered for the previous VCI test (described in Table 1), but with laterally varying thicknesses as shown in Fig. 4.19. This synthetic pseudo-2D data set was computed with the same FE parameterization as for the previous VCI test. Similarly, we added uncorrelated random noise in the range ±5% to each data point. The inversion setup was the same as for the previous test. Figure 4.20shows the results for four values of ζ. For the sake of consistency with the field data case discussed below, for which there is no STD information so that a χ^2 analysis is less relevant, the data misfits in term relative root mean square (RMS) error is also presented. In any case, it is clear from Fig. 4.20a and b that all the four experiments mostly fit the data within the error bars with comparable distributions, and by this fact show a stable sounding misfit level (of around 3 % in Fig. 4.20b) while showing different models (Fig. 4.20c). This highlights how non-unique is the inverse problem and motivates the use of various sharpness levels. When looking in more detail at each pseudo-section, we see rather high lateral variability of the solution. Our inversion procedure theoretically prevents over-fitting (this is well-demonstrated by Fig. 4.18) by including the information about the expected noise level in the inversion. Due to this characteristic, a data over-fitting cannot be considered as the main cause of such

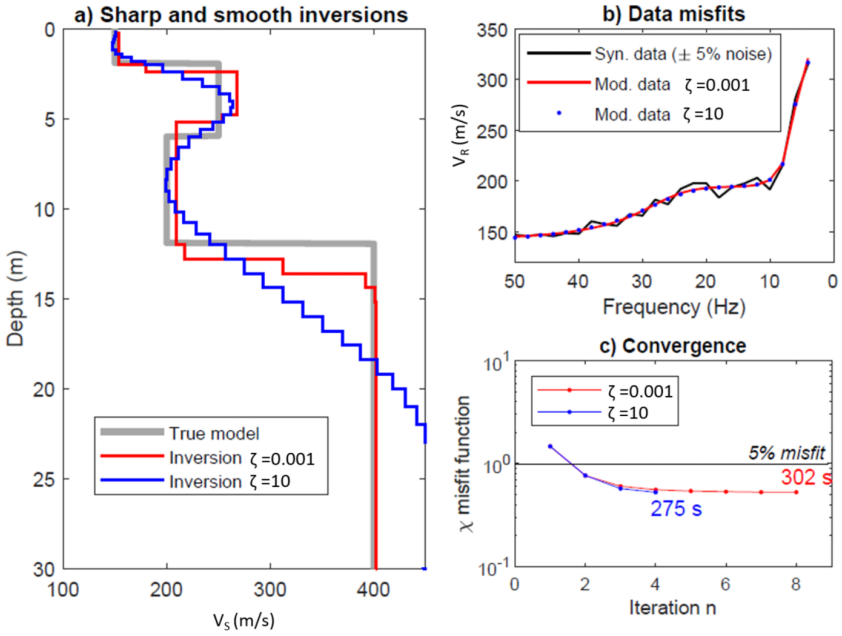

Figure 4.18: Noisy (±5%) synthetic experiment using the heterogeneous grid considered in the previous figure (100 layers) for $\zeta = 0.001$ (sharp) and $\zeta = 1$ (smooth). a) Comparison between the models obtained from both sharp and smooth inversions and the true model used for computing the synthetic data. b) Data misfits for the two tests. c) Evolution of the misfits during the iterative inverse procedure. We used a heterogeneous parameter grid with layer thickness increasing with depth and detailed in Fig. 4.17

variations. These kinds of lateral oscillations are actually recognizable in other examples of pseudo-2D reconstructions based on 1D forward modeling and concerning other types of geophysical data [4, 5]. These lateral instabilities in the solution are connected with the ill-posedness of the 1D inversion in presence of noisy measurements and a finite number of available observations. If using single-sounding inversions, such effect can only be avoided by laterally smoothing the data or by under-fitting the data. However, both of such operations may cost a loss in imaging resolution.

Synthetic Multi-soundings Laterally Constrained Inversion (LCI)

For the next synthetic tests, it is considered the simultaneous 1D inversions of 50 dispersion curves using bi-directional MGS constraints. By definition, such multi-soundings 1D inversion does not provide physically-based relations for modeling either the lateral variations of the models nor the lateral variations of the noise. In this respect, a 1:1 balance between the vertical and lateral constraints is not likely to be adapted for every case depending on the subsurface velocities and the spatial sampling of the profiles. That's why, in the presented inversion procedure, it is suggested a lateral weight γ in Eq. 4.14 to compensate such effect. In practice, γ can be easily adjusted by looking at the result of the first iteration. The workflow follows the steps: if the first iteration solution is significantly smoother than the lateral distribution of the dispersion curves, this means that γ is too large, conversely, if such solution shows an erratic lateral distribution, similar to some guessed noise feature, then γ should be increased. This operation is done manually as it required typically 4-5 tests only.

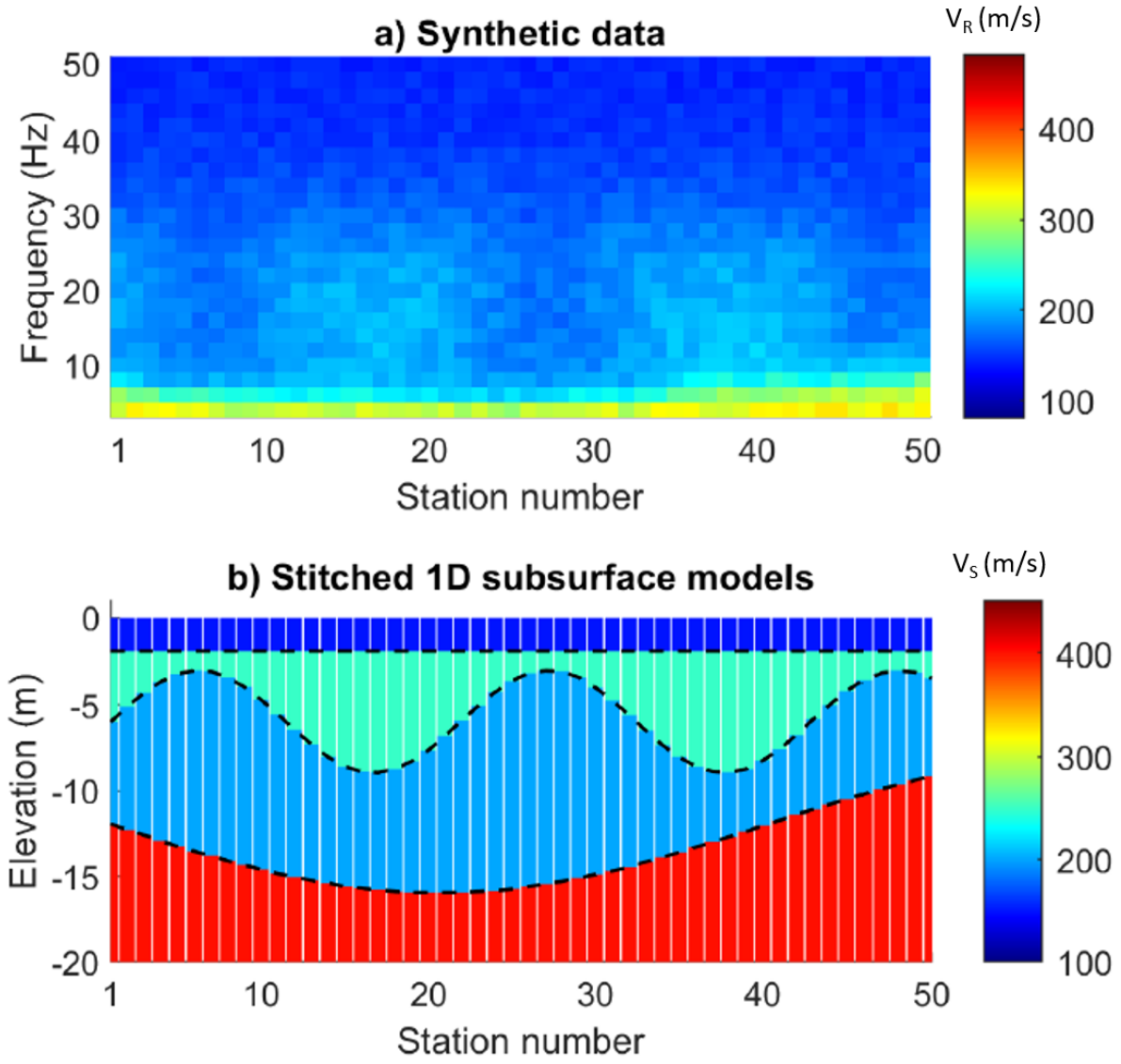

Figure 4.19: Synthetic pseudo-section composed of 50 soundings with (±5%) uncorrelated noise. a) Noisy synthetic multi-sounding data set. b) Input 1D subsurface β models stitched along the pseudo-section. The physical properties of the different layers are summarized in Tab. 4.1.

Similar to the single-sounding test, we take the starting models as a set of 50 homogeneous 1D models with a shear-wave velocity equal to the mean of the associated dispersion curves. This choice has important practical consequences as, for the first iteration, the term $\mathbf{L_z} log(\mathbf{V_S}^{(n)})^2$ from the vertical MGS operator, $S_{z,ij}$ is null, practically vanishes the vertical regularization. To avoid this effect, for the first iteration, and more generally if one of the vectors $\mathbf{L_{z,x}} log(\mathbf{V_S}^{(n)})^2$ contains zero values only, each regularization matrix is normalized by the sum of its diagonal.

$$\mathbf{W_m}^{(n=0,\mathbf{L_{z,x}} log(\mathbf{V_S}^{(n)})=0)} = \frac{\mathbf{Q_z}^T\mathbf{Q_z}}{\sum diag(\mathbf{Q_z}^T\mathbf{Q_z})} + \frac{\gamma\mathbf{Q_x}^T\mathbf{Q_x}}{\sum diag(\mathbf{Q_x}^T\mathbf{Q_x})} \tag{4.16}$$

For the following iterations, where model gradients show non-zeros values, we don't perform such balancing in order to ensure a rather "natural" or self-induced model-

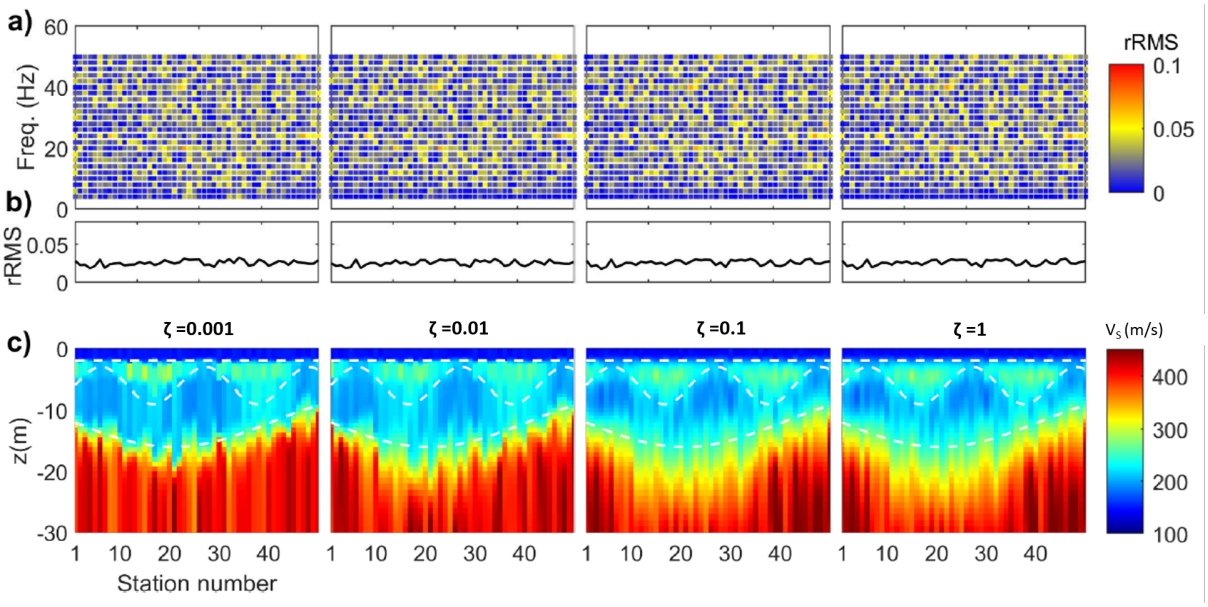

Figure 4.20: Single-sounding MGS inversions for different value of ζ applied to a pseudo-2D noisy ($\pm 5\%$) profile. a) Relative RMS value for each data point. b) Mean relative RMS value for each sounding. c) Pseudo-2D model resulting from stitching all the 1D inversion results along the pseudo-section. The used inversion grid is the same heterogeneous one utilized for the results in Figs. 4.17 and 4.18

dependent iterative sharpening effect. In practice, we scale nevertheless the complete regularization term by the sum of the diagonal elements of one MGS matrix (we take the z-direction). This is done to facilitate the β-search described above as it ensures that the optimal $\mathbf{V_S^n}$ lies in a relatively narrow range:

$$\mathbf{W_m}^{(n\geq 1, \mathbf{L_{z,x}} log(\mathbf{V_S}^{(n)})\neq 0)} = \frac{1}{\sum diag(\mathbf{Q_z}^T \mathbf{Q_z})} [\mathbf{Q_z}^T \mathbf{Q_z} + \gamma \mathbf{Q_x}^T \mathbf{Q_x}] \tag{4.17}$$

The results of the LCI-MGS inversion are shown in Fig. 4.21 for four values of ζ, hence providing models characterized by similar data misfits, but varying sparsity levels. We can see that the LCI inversion removes the lateral oscillations observed in the previous single-sounding inversions case without compromising the data fitting performances. This example illustrates the benefit of using lateral constraints and demonstrates the possibility to provide the resulting pseudo-2D models with different degrees of sharpness.

Field data example

In this section, we apply the proposed inversion scheme to observed surface wave data from a quick-clay research site in Norway [86].

The Vålen quick clay test site

Quick clay may be described as highly sensitive marine clay that changes from a relatively stiff condition to a liquid mass when disturbed. Extended quick lay layers account for a lot of geo-hazards in Scandinavia and North America and hence their occurrence and extent need to be mapped. The Vålen site is located near the town of Vestfossen, approximately 65 km south-west of Oslo. As a marine clay deposit in coastal, post-submarine area, this test site of the Norwegian Geotechnical Institute (NGI) is subject to quick clay

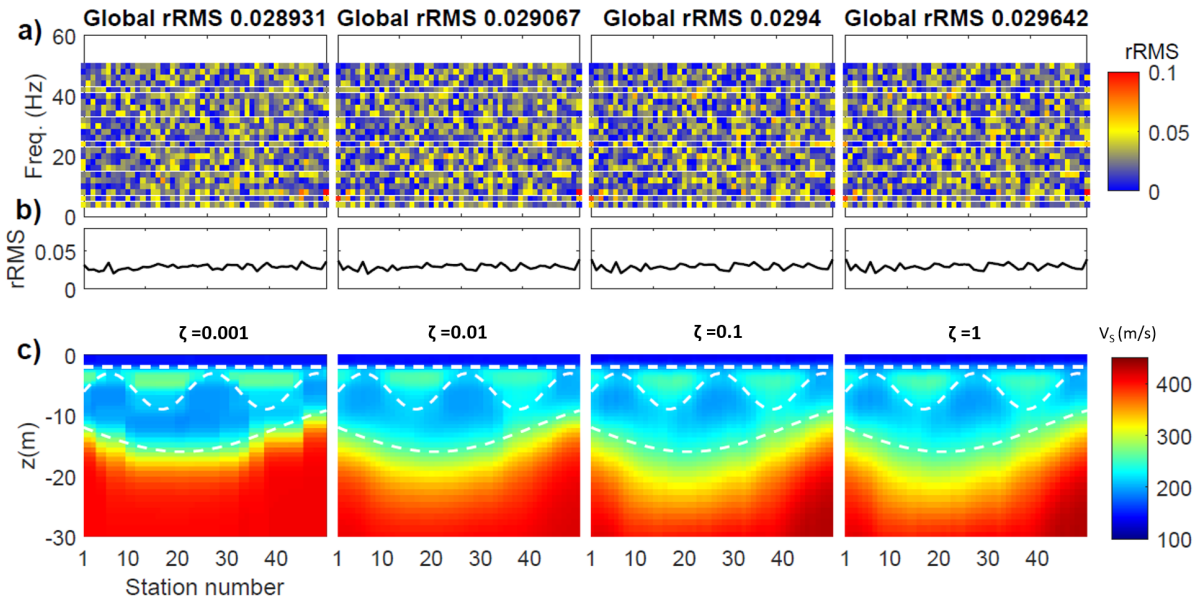

Figure 4.21: Multi-sounding MGS inversions for different values of ζ and $\gamma = 0.5$ applied to a pseudo-2D noisy ($\pm$%) profile. a) Relative RMS value for each datum; the global relative RMS value is indicated above the graphics. b) Mean relative RMS value for each sounding. c) Pseudo-2D section resulting from stitching all the 1D inversion results along the pseudo-line. The used inversion grid is the same heterogeneous one utilized for the results in Figs. 4.17, 4.18 and 4.20

landslides. Motivated by positive results obtained in a similar area [81], a geophysical survey including seismic measurements for (MASW) was performed in summer 2010 to better constrain the whole geological setting. The expected quick-clay layers are targeted to check their geophysical/geotechnical response to the different measurement techniques adopted. Here, we only consider the MASW data to test out our LCI-MGS inversion.

Multichannel Analysis of Surface Waves

Seismic surface-wave data were recorded using a Geometrics Geode seismograph with 24 4.5-Hz vertical geophones and a 5-kg sledgehammer as seismic source. The survey was carried out in roll-along mode. The offset between the source and the nearest geophone was kept at 5 m, with a geophone spacing of 1 m, leading to a geophone spread of 23 m. Data were recorded from 67 shot positions with 2-m shot spacing, thus yielding a 132-m long 2D line (Fig. 4.22). For each configuration, the shots were repeated twice and stacked on-site to improve the signal-to-noise ratio. The sampling interval was 0.25 ms, with a record length of 1 s. For each of the configurations, the dispersion curves were picked interactively using either a commercial software (SurfSeis; phasevelocity/frequency domain) [77] or in-house frequency/wavenumber domain routines. However, the data covering the south-eastern part of the acquisition line show both fundamental and higher modes.

Inversion of dispersion curves

The data pseudo-section showing the dispersion curve as a function of the distance from the initial point of the Vålen's survey line is presented in Fig. 4.22 . Four ζ values was tested, ranging from 0.001 to 1 and we use a lateral weight of $\gamma = 2$. Because the

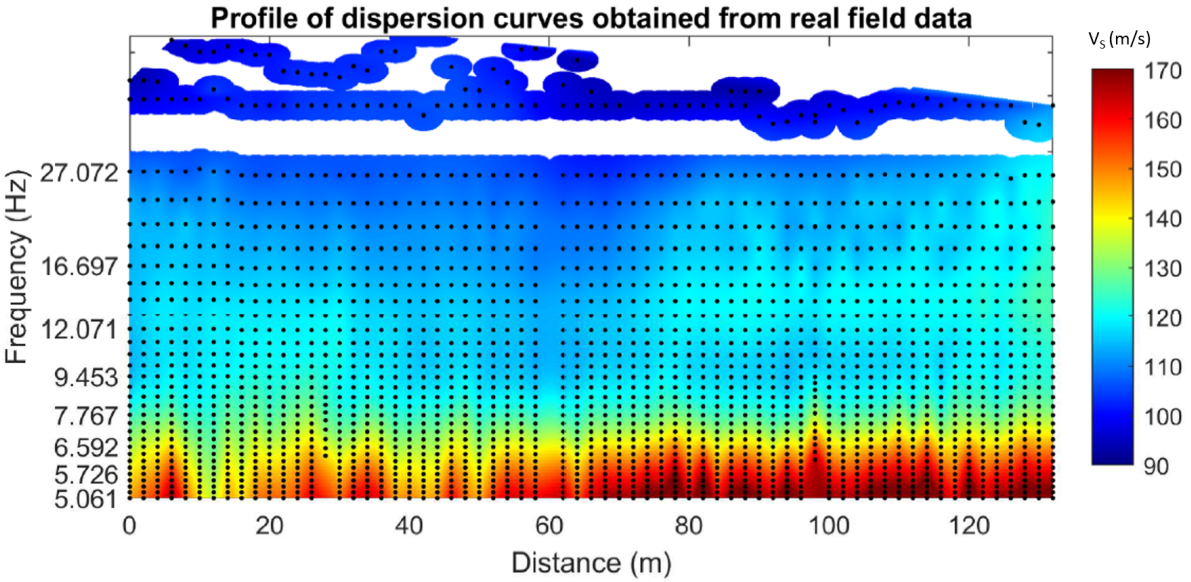

Figure 4.22: Pseudo-section of the Rayleigh wave velocity as a function of frequency and off-set as extracted in the range 5-50 Hz from the seismic data collected in Vålen (Norway). Each column represents the dispersion curve for that specific location.

observed velocities are slower for this data set, we set a heterogeneous grid composed of 40 layers with a maximum depth of 40 m with the following layer thickness distribution from top to bottom: [10 layers of 0.4 m; 10 layers of 0.8 m; 10 layers of 1.2 m; 10 layers of 1.6 m]. Because we have no robust information about the true level of uncertainties, we assumed, based on the variability in the data, a standard deviation of 2%. The results are shown in Fig. 4.23. Consistently with our assumptions, the large majority of the data are fitted within the 2% threshold; only around 15 Hz, the data misfit is systematically higher, but still it never exceeds 4%.

Not surprisingly, the retrieved shear-wave velocity distributions (characterized by different levels of vertical and lateral sparsity) are equally compatible with the observations. Still, they present very peculiar and different features; for example, the smooth horizontal transition from the relatively high-velocity area ($> 200m/s$) at the bottom of the section and the shallower layer disappears when the ζ value decreases. In the same way, also the deepest fast layer is more homogeneous when the inversion settings are selected to favor more blocky reconstructions. Along the same line of reasoning, it is probably worth noticing that the shallow layer ($\sim 150m/s$ - characterizing the shear-wave velocity inversion in the near-surface) extends continuously for the entire length of the section in the smoother reconstructions, whereas, when stronger sparsity constraints are chosen, it is not only better defined vertically, but, laterally, it dissolves into an (almost) homogeneous upper layer of ($< 150m/s$). The interpretation of the geotechnical soundings available for this test site indicates the presence of a quick-clay layer from about 30 m distance to the end of the line, at about 5 m depth. This unit is around 10 m towards the end of the profile and thinner in the middle. The low-velocity layer around 5 m below the surface would then correspond to the quick clay. To this respect, the inversion results with a low ζ value are in better agreement with the interpretation of the geotechnical soundings. The more detailed correspondence of the different inversion results with the actual geology needs to

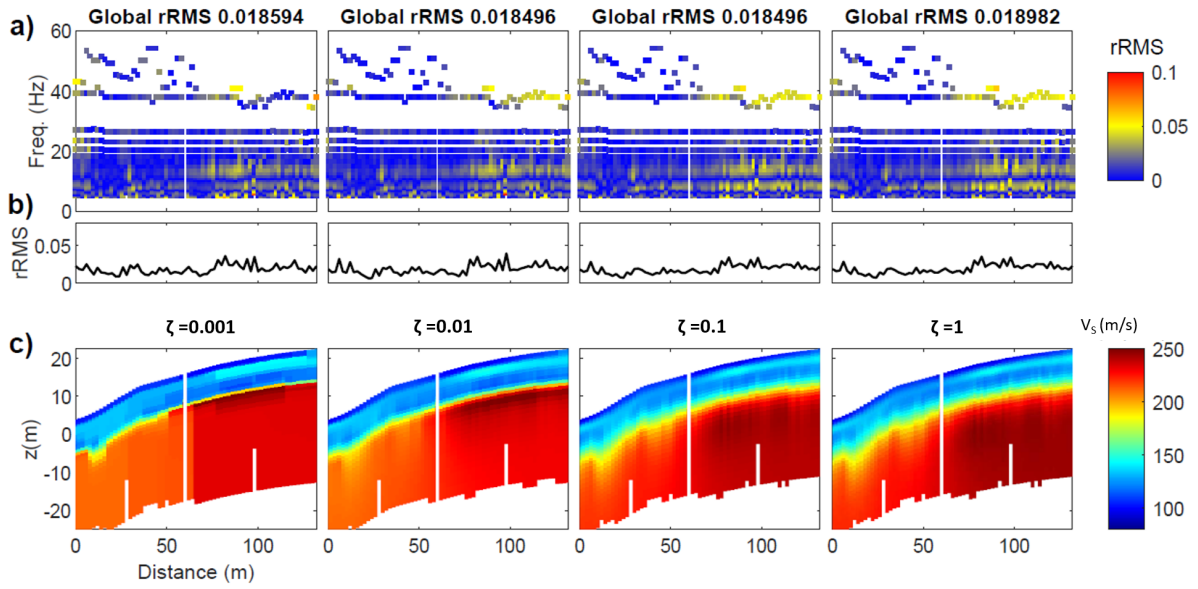

Figure 4.23: Multi-sounding MGS inversions for different values of ζ and $\gamma = 2$ applied to the field data shown in Fig. 4.22. a) Relative RMS value for each data point ; the global relative RMS value is indicated above the graphics. b) Mean relative RMS value for each sounding. c) Pseudo-2D section resulting from stitching all the 1D inversion results along the pseudo-line. We use a 40 layers heterogeneous parameter grid with layer thickness varying from top to bottom as follows: [10 layers of 0.4 m; 10layers of 0.8 m; 10 layers of 1.2 m; 10 layers of 1.6 m].

be further investigated, but it is, in any case, not the point of the present research. In fact, what we would like to convey here is that surface wave inversion is a severely ill-posed problem, so, a proper regularization is necessary and the MGS provides a useful tool to explore the model space by enforcing variable levels of sparsity both in the vertical and, now, also the horizontal directions. The field example clearly demonstrates that even with a relatively low noise level in the data, rather different shear-wave velocity distributions can be inferred. This variability needs to be taken into account and possibly quantified in order to support quantitatively decisions that might have relevant socio-economic impacts, as, here, concerning the quick clay conditions [87], or in other cases, regarding, for example, the seismic risk assessment [10].

4.2.4 Conclusions

We incorporate the Minimum Gradient Support (MGS) regularization into a Laterally Constrained Inversion (LCI) scheme. This allows the reconstruction of (pseudo-)2D distribution of shear-wave velocity inferred from dispersion curve measurements with a tunable level of sparsity. It is the first time that LCI-MGS approaches are applied to seismic surface wave inversion. In addition, in the attempt to increase the local convexity of the minimization problem, we propose to perform the inversion in the space of the logarithm of the parameters' values. Moreover, the adopted strategy for the automatic selection of the parameter controlling the importance of the regularization is discussed in detail. The performances of this novel algorithm are tested both on synthetic and field data showing, once more, the necessity for a flexible tool to explore the solution space and to enforce

the model spatial coherence by means of the proper prior information.

Chapter 5

Constrained inversion of time domain electromagnetic and surface waves data for geotechnical characterization of the PLLN

This chapter is based on two conference papers:

- *Inversion of electrical resistivity tomography (ERT) and transient electromagnetic (TEM) data for geotechnical site characterization of PLLN alluvial area, Lisbon.* submitted to the 6^{th} International Conference on Geotechnical and Geophysical Site Characterization that took place in Budapest - Hu, September 2021 [9].
- *Inversion of TDEM data constrained by surface seismic and borehole surveys for geotechnical characterization of the Northen Lisbon Logistic Park (PLLN)* presented on the 4^{th} Doctoral Congress in Engineering, that took place in Porto - PT, June 2021 [99].

5.1 Introduction

This chapter presents the result of several surveys carried out in the Northern Lisbon Logistic Park (PLLN) to map the underground to provide a good geotechnical characterization.

Geophysical methods have become an increasingly common practice in different areas such as mining, archeology, environmental studies, hydrology, geotechnical characterization, among others. There have been numerous applications of these methods in geotechnics. Solberg et al. [92] combined geotechnical studies, electromagnetic data collected by helicopter, electrical resistivity tomography (ERT), and electric cone penetration (CPT) data to investigate an area where landslides occurred, in Trondheim - Norway in 2012. The fact that they performed an electrical tomography shortly after the landslide was useful to outline future risk areas and to develop a possible evacuation plan for the population. Giordano and Comina [37] carried out ERT and seismic surface waves (SSW) tests to study the stability of a natural bridge in Piedmont-Italy. As both methods are non-invasive, it was possible to investigate the state of the bridge without damaging it. The investigation allowed the description of the natural state of the rock mass that composes the bridge and possible mechanisms of instability.

Constrained inversion of time domain electromagnetic and surface waves data for geotechnical characterization of the PLLN

Geotechnical and foundation projects require a deep knowledge of the subsurface. Defining the boundaries of each material and correctly characterizing them is essential. The application of geophysical methods for geotechnical characterization has become a common practice due to the possibility of investigating large areas within a short time, in a non-intrusive way, and with a great ratio of cost-effectiveness. When compared with conventional ground surveys like, e.g., boreholes, CPT, SPT, geophysical methods are a great asset since they can be performed with few people and with equipments that are easy to transport even by a single person. The survey doesn't take long and is performed with a minimum perturbation of the site.

The present work aims to take advantage of different information, from geophysical and geotechnical methods to improve the subsurface characterization.

5.2 Study Area

The study area is located in the Northern Lisbon Logistic Park (PLLN), in Castanheira do Ribatejo (Vila Franca de Xira, Portugal), Fig. 5.1.

On the left bank of the Tejo River, the area has good access to road and maritime infrastructures. A project for a river pier and the construction of a warehouse and several support buildings such as a nursery, car silo, social building, and water reserves have been studied. Due to future constructions, several geotechnical surveys have been performed and some of the results are published in [61].

The alluvial plain is located in the region of the left bank of the lower sedimentary Tejo basin and is geologically framed in the Cenozoic sedimentary basin of the lower Tejo, where an important sedimentary filling, predominantly detrital and of continental origin, is preserved, with interpolations of marine and brackish formations corresponding to transgressive maximums (Fig 5.2). The existing landfill deposits have an anthropogenic origin and are mainly due to platforms for the insertion of road and railways, as well as for the implantation of buildings and the construction of landfills along the riverbanks to protect marginal land from flooding [23].

In the Tejo valley, alluviums are generally made up of alternating sands and muds, with a basal deposit of sand with pebbles and gravels that can reach four dozen meters. Pebbles and/or gravels are often dominant. These layers are contemporaneous with the Wurm regression maxim [17].

The total area of PLLN is 100ha, from which 7.3ha were studied in this work. The area investigated in this work is shown on the left in Fig. 5.1 by the shadow zone, and in more detail on the right, with the seismic and TDEM surveys marked.

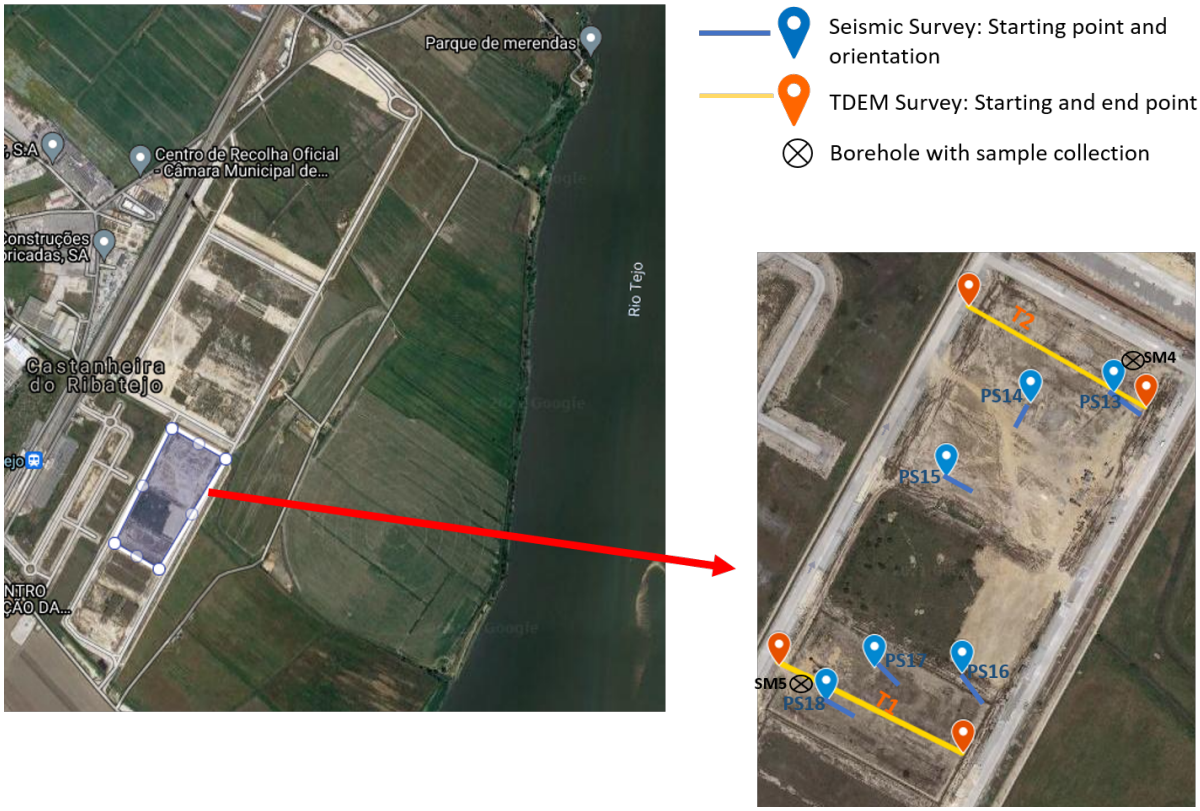

Figure 5.1: Area under study and location of the seismic and TDEM surveys

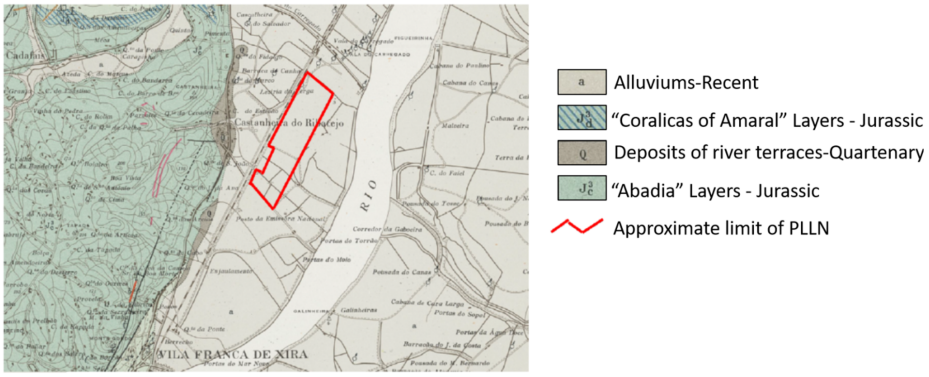

Figure 5.2: Geological framing of PLLN (Geological Cartography - Sheet 30-D, Alenquer, Geological Services of Portugal)

5.2.1 Seismic survey

The seismic active MASW and the passive HVSR methodology were applied. Figure 5.1 shows the place where the surveys were performed as well as its orientation. The MASW was carried out over 48 m with 24 geophones of 4.5 Hz (Geospace) spaced 2 m each, with record of the vertical component. The energy source used was a 10 kg hammer, applied on both ends of the profile, East and West. For each line of acquisition, 10 individual shots were recorded, for each side (East and West).

The HVSR data were collected at the central point of the 48 m alignment with the seismograph MR2002-CE(SYSCOM) and as receiver a 3D velocity sensor (MS2003+,

SYSCOM) that presents the same characteristics for the three components and a flat response between 1 and 350 Hz. Time series were recorded for 40 to 50 min, with a sampling frequency of 400 Hz.

5.2.2 TDEM survey

In the present work, the acquisition of electromagnetic data was performed with the TEM-FAST 48 HPC equipment. This equipment allows obtaining two parameters as a function of time, the resistivity (Ωm) and impedance (V/A). The configuration used was a 25 m square loop where the transmitting source (Tx) and the receiver (Rx) are coincident. Two profiles (T1 and T2 in Fig. 5.1), each 150 m long, were studied by performing 15 adjacent acquisitions located 10 m apart.

5.3 MASW and HVSR Inversion workflow

The dispersion curve provided by the MASW data and the ellipticity curve provided by the HVSR data were jointly inverted with the software *Geopsy* [36]. The inversion strategy, developed by Wathelet [108, 109] is a stochastic direct search method and applies the neighbourhood algorithm. The multidimensional parameter space is divided into Voronoi cells (Fig. 5.3), which are used to make the decomposition of the parameter space. A misfit value is associated with each cell, which is calculated for the central point (Fig. 5.3).

The characteristic setting parameters are (as discussed in details in [108]):

- it_{max}: number of iterations to perform;
- n_{s0}: number of models randomly chosen inside the parameter space at the beginning of the inversion;
- n_s: number of models to be generated at each iteration;
- n_r: number of best cells (with the lowest misfit) in which the n_s models are generated.

The inversion process is composed of the following phases:

1. a set of n_{s0} models is randomly generated with a uniform probability in the parameter space;
2. the misfit function is calculated for the most recently generated models;
3. the n_r models with the lowest misfit of all models generated so far are selected;
4. an average of $\frac{n_s}{n_r}$ new samples with a uniform probability in each selected cell is generated;
5. the n_s new samples are added to the previous ensemble of models. The procedure goes back to the second step for the number of iteration itmax. .

Figure 5.3(a) is an example of a two-dimensional parameter showing the models (black dots) and the limits of the Voronoi cells. n_{s0} models (=9, in this case) are generated and the grey cell has the lowest misfit. In this example, seven new models are generated in one cell ($n_r = 1$, and $n_s = 7$). Figure 5.3(b) depicts the Voronoi geometry after the first iteration. For a more detailed description of the method see [108, 109].

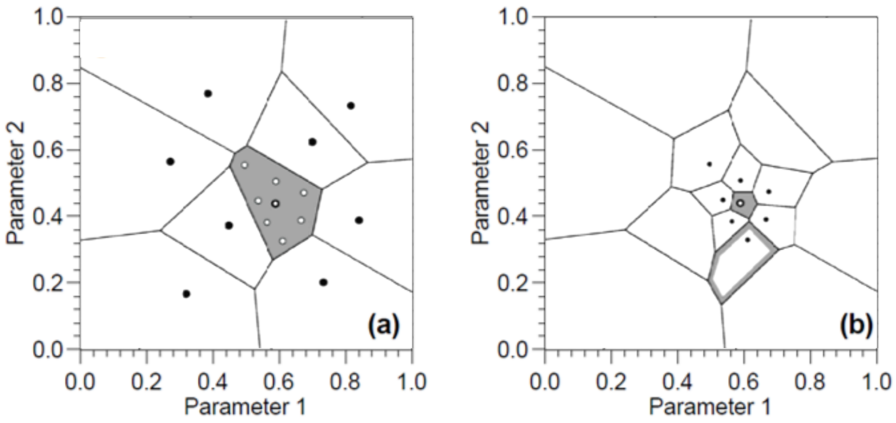

Figure 5.3: Voronoi cells for 2D space. Based on [108]

5.4 TDEM Inversion workflow

The inversion strategy applied to the TDEM data follows the general principles described in from chapter 3 and 4. The inverse problem is solved as an optimization problem where the goal is to find the model minimizing the stabilizer that, at the same time, generates data compatible with the observations.

The objective function for TDEM problem, similar to Eq. 4.3 is:

$$\phi(\mathbf{m}) = \frac{1}{2}\phi_d + \beta\phi_m(\mathbf{m}) = \frac{1}{2}\left\|\mathbf{W_d}(\mathbf{d^{obs}} - F(\mathbf{m})\right\|^2 + \beta\left\|\mathbf{W_m}(\mathbf{m} - \mathbf{m_{ref}})\right\|^2 \tag{5.1}$$

where d^{obs} are the acquired TDEM data, $F[m]$ is the forward operator that for a given resistivity model $[m]$ simulates the respective data, W_d and W_m are weighting matrix, λ is the trade-off parameter that balance the importance between the misfit and the regularization, and m_{ref} is a reference model.

In this specific case, the inversion was carried out as an optimization problem using the second-order Inexact Gauss-Newton method implemented in an open source software *SimPEG* [20]. It was used a Tikhonov regularization, as presented in Eq. 5.1, where the resulting model is forced to be close to a reference model.

The data weighting matrix $\mathbf{W_d}$ is a diagonal matrix whose elements are given by $\frac{1}{\sigma_\mathbf{i}}$, where $\sigma_\mathbf{i}$ is the error associated to the i^{th} data. The model weighting matrix $\mathbf{W_m}$, for the Tikhonov regularization is defined as 1D discrete approximation of the spatial derivative.

The trade-off parameter, β is defined through a cooling approach, where β is reduced by a factor of 1.5 every Gauss Newton iteration.

The stopping criteria is based upon the discrepancy principle, stopping the inversion when $\phi_d \leq \chi\phi_d^*$, with $\chi = 1$ and $\phi_d^* = 0.5N_{data}$ (with ϕ_d as defined in Eq. 3.3).

5.5 Results

5.5.1 Constrained Inversion

The inversion of TDEM data constrained by a reference model based upon available information from seismic inversion and boreholes, and connected through petrophysical relationships was performed. This study aimes to understand how important is, for the TDEM inversion, to have good prior information and how this information improves the final model.

Two tests were performed with the same parameters (mesh discretization, weight matrix values, number of iterations, etc.), differing only in the reference model. In test A the reference model is a homogeneous medium with a resistivity of 25 Ωm. In test B the reference model is defined as shown in Fig 5.4. Based on the model provided by the seismic survey (Fig. 5.5) and the borehole (Fig. 5.6), each layer was identified as a soil type. With the soil type identified, through tables published in the literature [12, 80, 82, 83], a range for the value of resistivity was defined. From this range, a specific value of resistivity for each layer was chosen based on electrical tomography survey [9] performed at the same place. The resistivity values for each reference model are presented in Tab. 5.1 a) for the profile T1 and in Tab. 5.2 a) for the profile T2. It should be noted that the resistivity value can vary by several orders of magnitude for the same material depending on the location, as it is affected by temperature, soil saturation, salinity of water content, porosity, among others. Due to this variation on resistivity values for the same material, a sensitivity test was performed, to understand the influence of the choice of the resistivity for each layer at the reference model impacts the final model. Fig. 5.7 shows the result for 4 inversion models:

- m_1 is the model obtained with the reference model presented in Fig. 5.4b.
- m_2 is the model obtained from a reference model created from m_1^{ref} with a deviation of +5%
- m_3 is the model obtained from a reference model created from m_1^{ref} with a deviation of -5%
- m_4 is the model obtained from a reference model created from m_1^{ref} with a deviation of +10%

From Fig. 5.7 is possible to see that the resulting model (m_1, m_2, m_3, m_4) is weakly modified by small variations on the reference model. The variation is more marked at the 4^{th} material layer, where the difference between the inverted models is visible.

Figure 5.5 represents the seismic profile obtained at a location very close to the TDEM survey. The seismic active MASW and the passive HVSR methodology were applied. The acquisition was performed in both directions along the survey line, East and West, indicated PS_E and PS_W. The result is associated with a range of possible models characterized by a 30%-wide data misfit range, described as PS_E^{lim} and PS_W^{lim} in Fig. 5.5. A detailed description of the procedure for acquiring SSW data and processing them is given in [38, 61]. Although there were 6 seismic acquisition lines, only those close to the TDEM profiles T1 and T2 (Fig. 5.1) were used in this work (PS13 and PS18).

Figures 5.8 and 5.10, and 5.9 and 5.11 show the inversion result for the 15 TDEM acquisitions plotted side by side for test A and test B, respectively along profiles T1 and

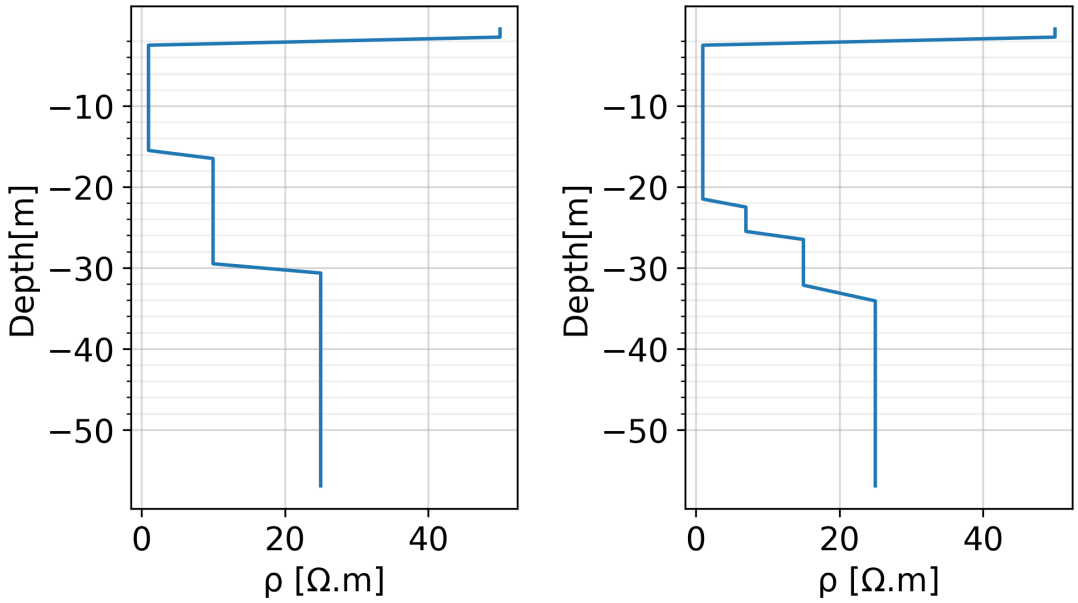

(a) T1 - Reference model **(b)** T2 - Reference model

Figure 5.4: Reference model used to constrain the TDEM inversion and based upon the seismic profile and borehole information.

a) Reference Model			b) Test A			c) Test B		
Layer	Thickness [m]	Resistivity [Ω.m]	Layer	Thickness [m]	Resistivity [Ω.m]	Layer	Thickness [m]	Resistivity [Ω.m]
1	2.0	50.0	1	4.0	0.7 to 3.9	1	1.0	16.0 to 33.0
2	12.0	1.0	2	7.0	0.1 to 6.0	2	3.0	0.8 to 1.5
3	14.0	10.0	3	18.0	3.8 to 9.2	3	10.0	0.3 to 0.9
4	-	25.0	4	-	0.5 to 25.0	4	15.0	4.2 to 11.6
						5	-	19.1 to 25.0

Table 5.1: Resistivity values and layer thickness for each layer on the reference model and for the the inversion of the 9th acquisition in test A and B at T1

a) Reference Model			b) Test A			c) Test B		
Layer	Thickness [m]	Resistivity [Ω.m]	Layer	Thickness [m]	Resistivity [Ω.m]	Layer	Thickness [m]	Resistivity [Ω.m]
1	2.0	50.0	1	1.0	6.2 to 11.5	1	1.5	17.0 to 31.0
2	20.0	1.0	2	8.0	0.2 to 2.4	2	20.0	0.7 to 2.1
3	2.0	7.0	3	22.0	1.4 to 14.8	3	3.0	4.0 to 8.0
4	8.0	15.0	4	-	1.2 to 8.4	4	6.0	12.1 to 15.9
5	-	25.0				5	-	22.1 to 23.4

Table 5.2: Resistivity values and layer thickness for each layer on the reference model and for the inversion of the 9th acquisition in test A and B at T2

T2. For the first profile - T1, comparing Fig. 5.8 and Fig. 5.9, Test B identified one more layer than Test A, the most superficial layer, designated as landfill in the reference model. Both identified a conductivity layer, but with different thickness and position. Test A identify this layer from 5 to 10 m and Test B from 2 to 16 m. An intermediate resistivity layer is also identified by both models, until 30 m deep. Tables 5.1 b) and 5.1

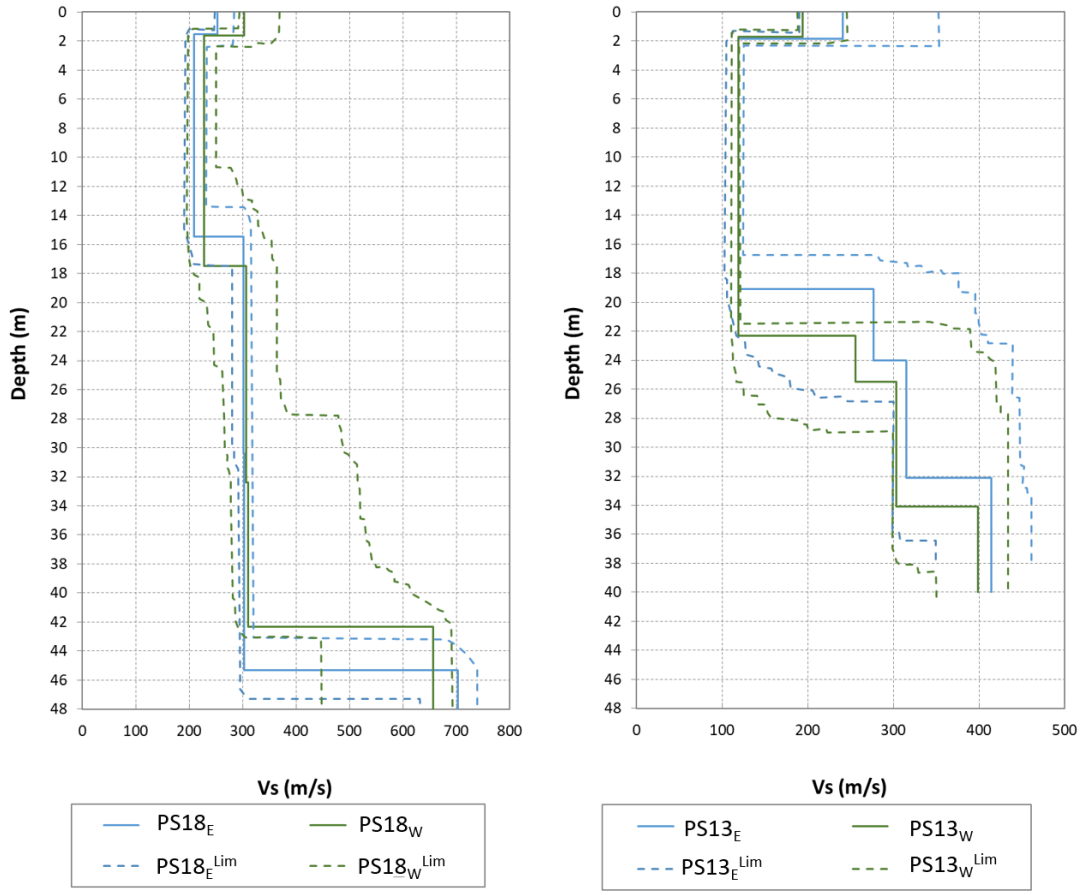

(a) PS18 **(b)** PS13

Figure 5.5: Seismic Profile from joint inversion of MASW + HSVR. $PS18_E^{lim}$ and $PS18_W^{lim}$ define the interval for the chosen model ($PS18_E$ and $PS18_W$) at the acquisition with East and West direction, respectively (The same for PS13). Adapted from [61]

c) show the approximate values for the resistivity and thickness of each layer for tests A and B respectively, on the ninth acquisition. The predicted and observed data for each sounding along profiles T1 and T2 are presented in Fig. 5.12 and 5.12. These figures shows that both models are fitting the data with a $\chi^2 \approx 0.87$. Table 5.1 a) represents the values used in the reference model. Through its analysis, it is possible to notice that, as expected, model B has values of resistivity and thickness of the layers close to the reference model. Despite the discrepancy between the intermediate layers, both models identified the bedrock at a depth of 30m. For the second profile - T2, both tests identify a first layer with higher resistivity, equivalent to the landfill, the difference is on the resistivity value for this layer. Without the reference model, test A identifies a layer from $\approx$ 2.0 m to 10.0 m with low resistivity, indicating a saturated soil. Test B group this layer with the next, and this low resistivity layer becomes thicker, with $\approx$ 18m. Like in the first profile, since test B has the information provided by the reference model, the resulting model tends to be close to this one, and the shape and values of resistivity are similar to the reference model.

As mentioned in [80, 83], the resistivity in rocks and soils is given by the conduction

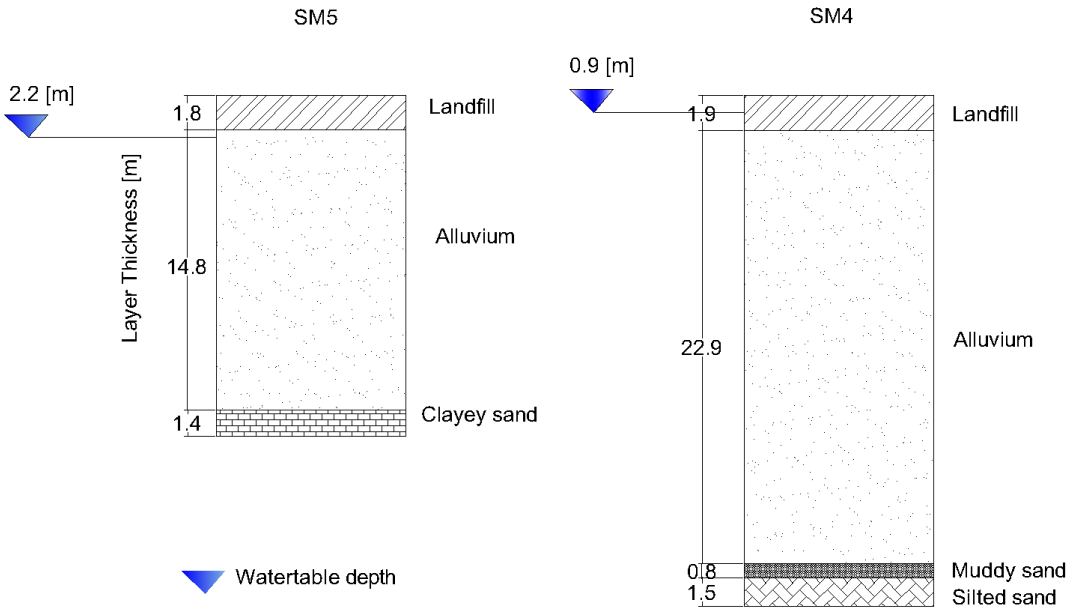

Figure 5.6: Geological profile from the borehole SM5 and SM4, as shown in Fig. 5.1 close to the place where the TDEM was carried out

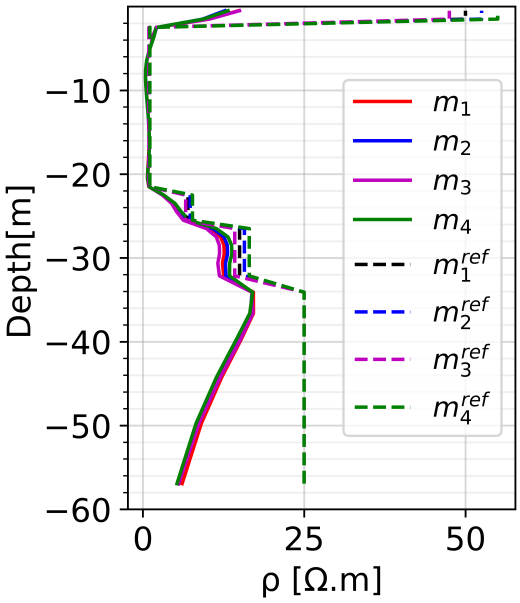

Figure 5.7: Sensitivity test performed to understand the influence of variations on the choice of the resistivity values for the reference model

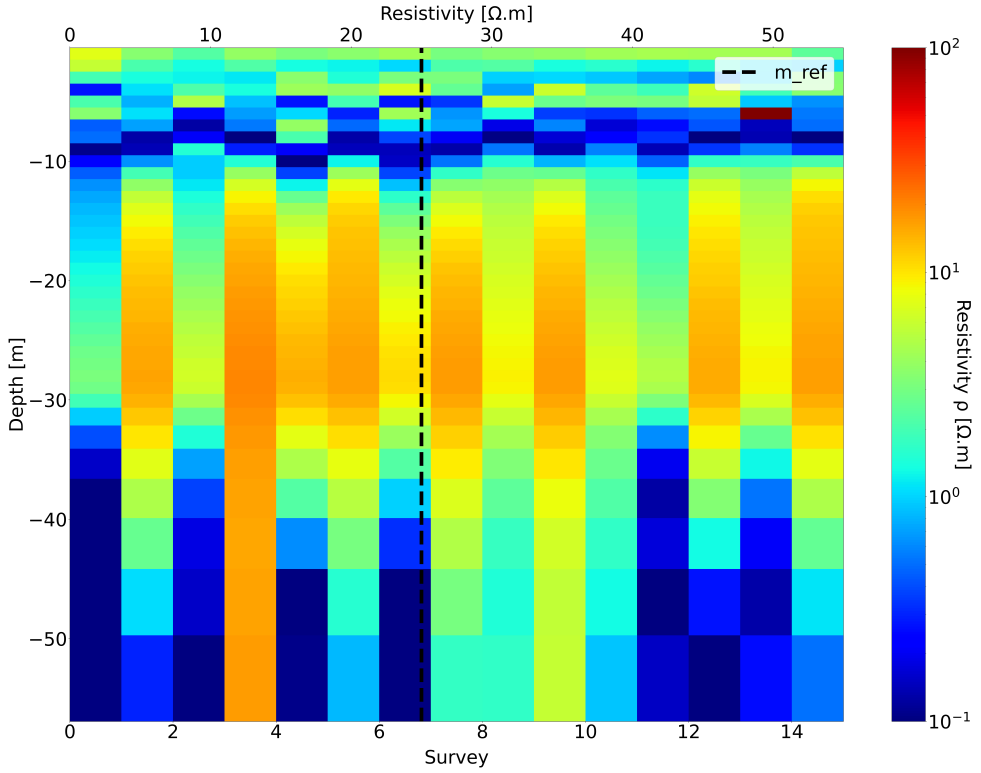

Figure 5.8: T1 - Test A: Inversion of TDEM data with homogeneous reference model

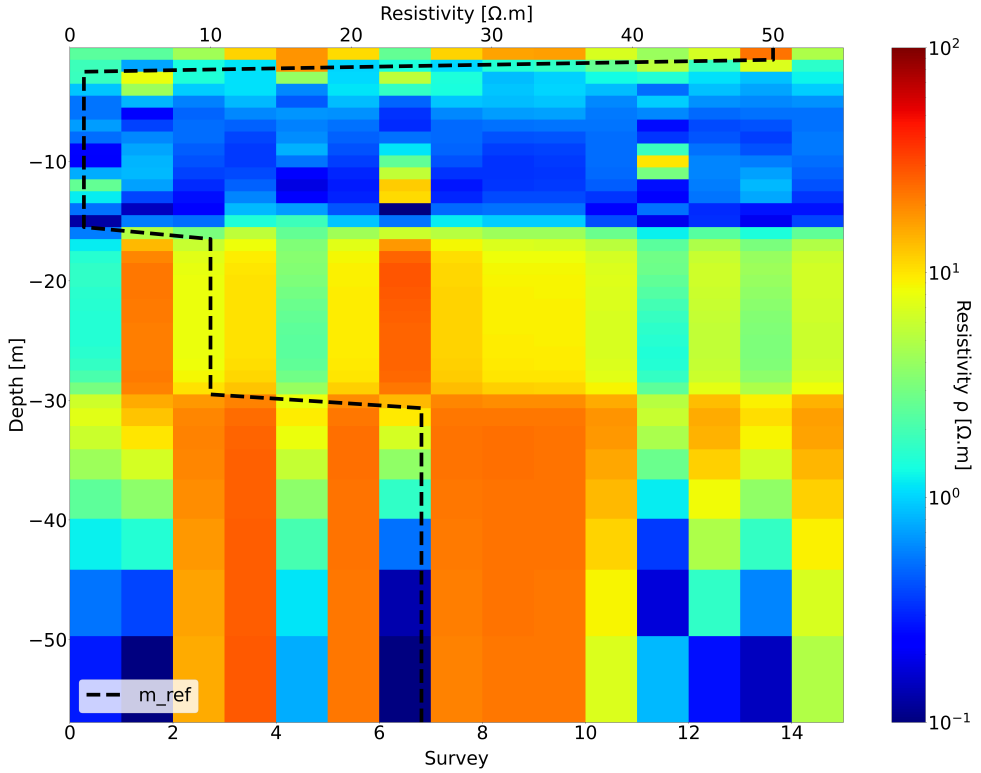

Figure 5.9: T1 - Test B: Inversion of TDEM data with reference model shown in Fig. 5.4a

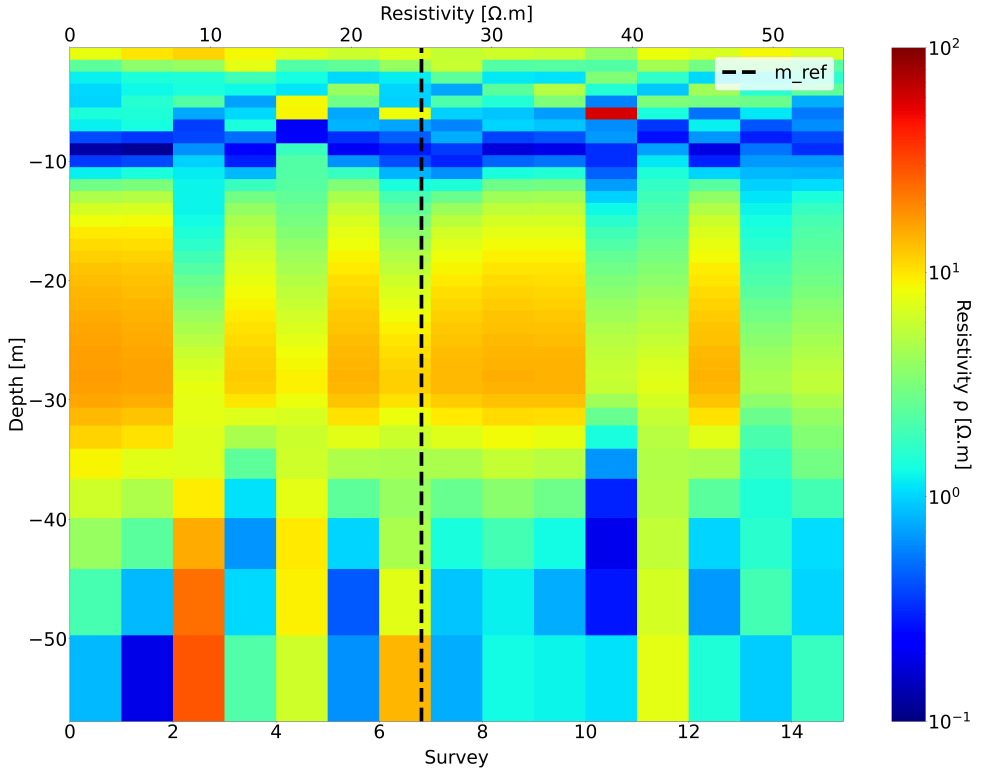

Figure 5.10: T2 - Test A: Inversion of TDEM data with homogeneous reference model

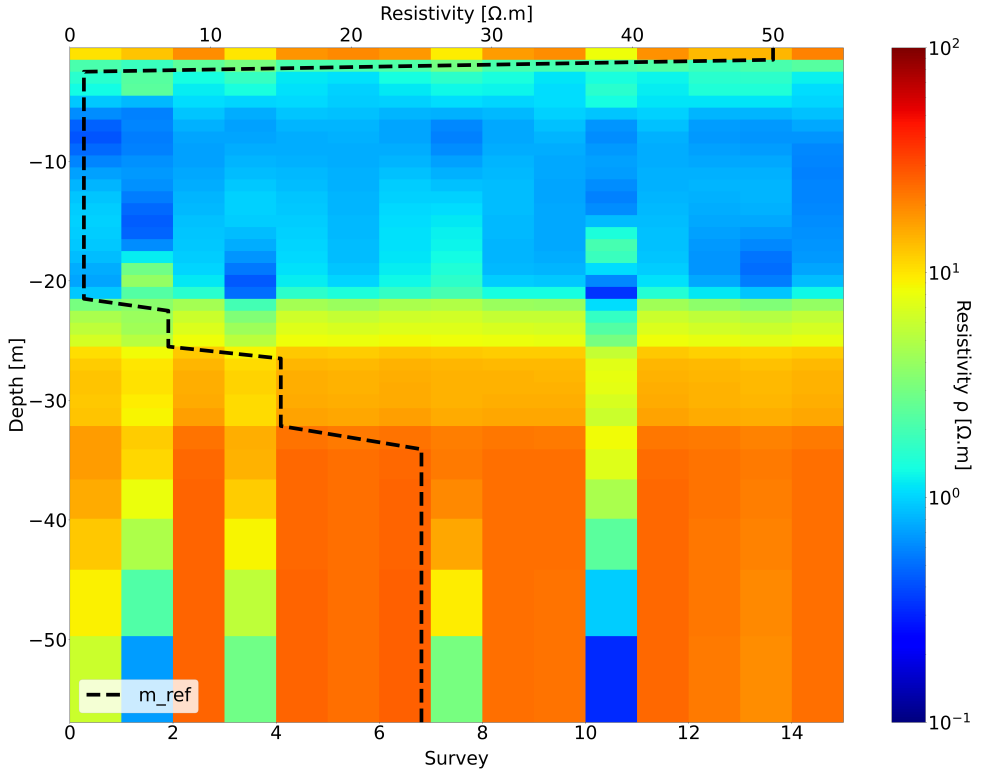

Figure 5.11: T2 - Test B: Inversion of TDEM data with reference model shown in Fig. 5.4b

of ions in the pores, so the porosity and the material that fills the pores have a great influence on the resistivity value. In the case under study, the water level was quite shallow, at a depth of 2.20m and it was brackish water, which leads to very low resistivity values between $0.1\Omega m$ and $25.0\Omega m$. The presence of a thick very conductive layer lower the depth of investigation, which makes the TDEM method reach only a depth of 30m (when in theory should reach 3 to 4 times the size of the loop [93], in this study the loop size is 25m).

The analysis of tests A and B allows concluding that the introduction of an accurate reference model leads to a more uniform result, with smoother variations and with resistivity values closer to those indicated in the reference model, which is desirable when one has a high degree of confidence in the proposed reference model. Without the introduction of a reference model, the interface between the first and second layer wasn't clear, this result would be enough for a first characterization of geotechnical layers and the bedrock depth. However, for a geotechnical project, an accurate resistivity and thickness of each layer are relevant, for which the result from test B would more suitable.

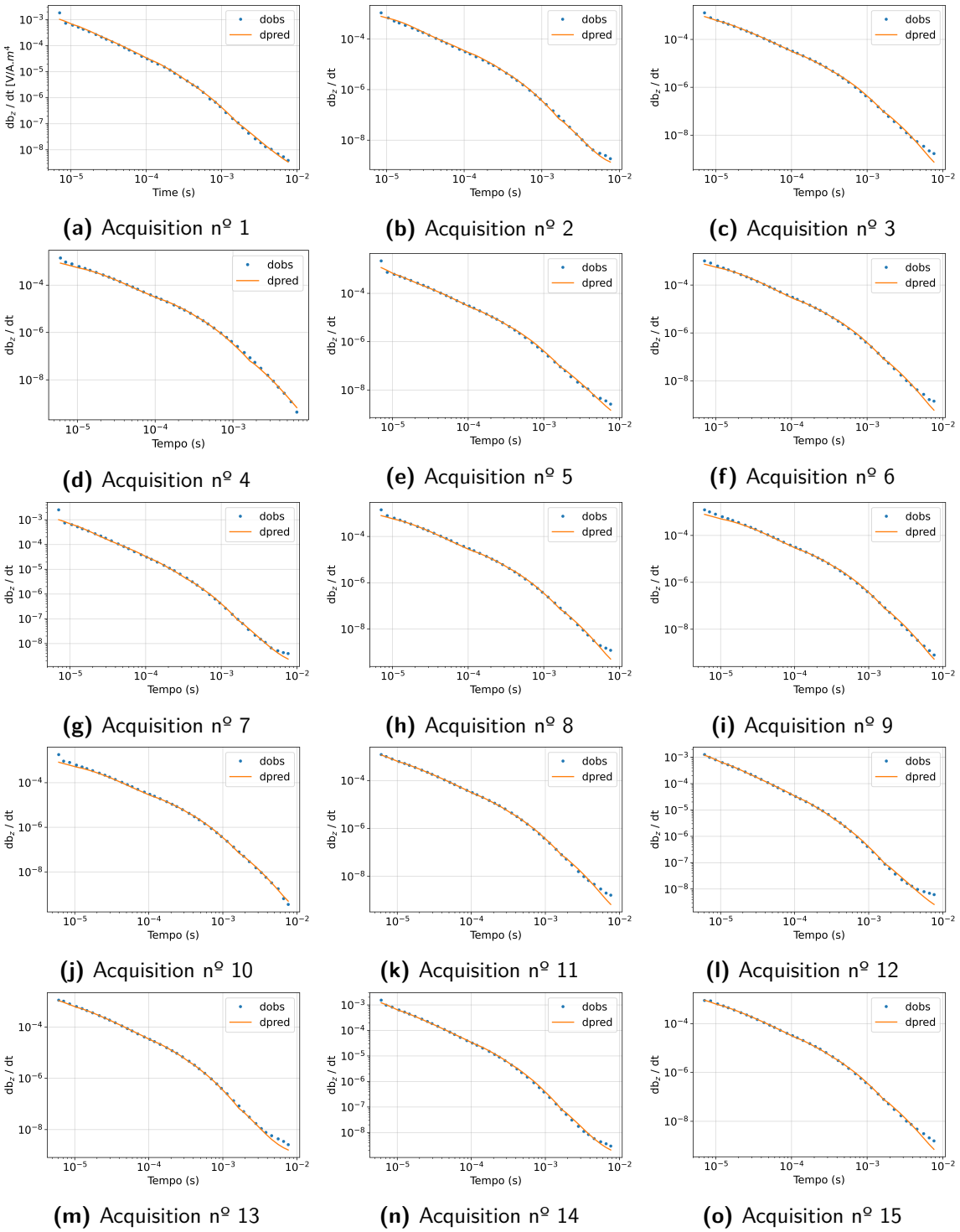

(a) Acquisition nº 1 **(b)** Acquisition nº 2 **(c)** Acquisition nº 3

(d) Acquisition nº 4 **(e)** Acquisition nº 5 **(f)** Acquisition nº 6

(g) Acquisition nº 7 **(h)** Acquisition nº 8 **(i)** Acquisition nº 9

(j) Acquisition nº 10 **(k)** Acquisition nº 11 **(l)** Acquisition nº 12

(m) Acquisition nº 13 **(n)** Acquisition nº 14 **(o)** Acquisition nº 15

Figure 5.12: Predicted and observed data for TDEM inversion of T1 with the reference model presented in Fig. 5.4a.

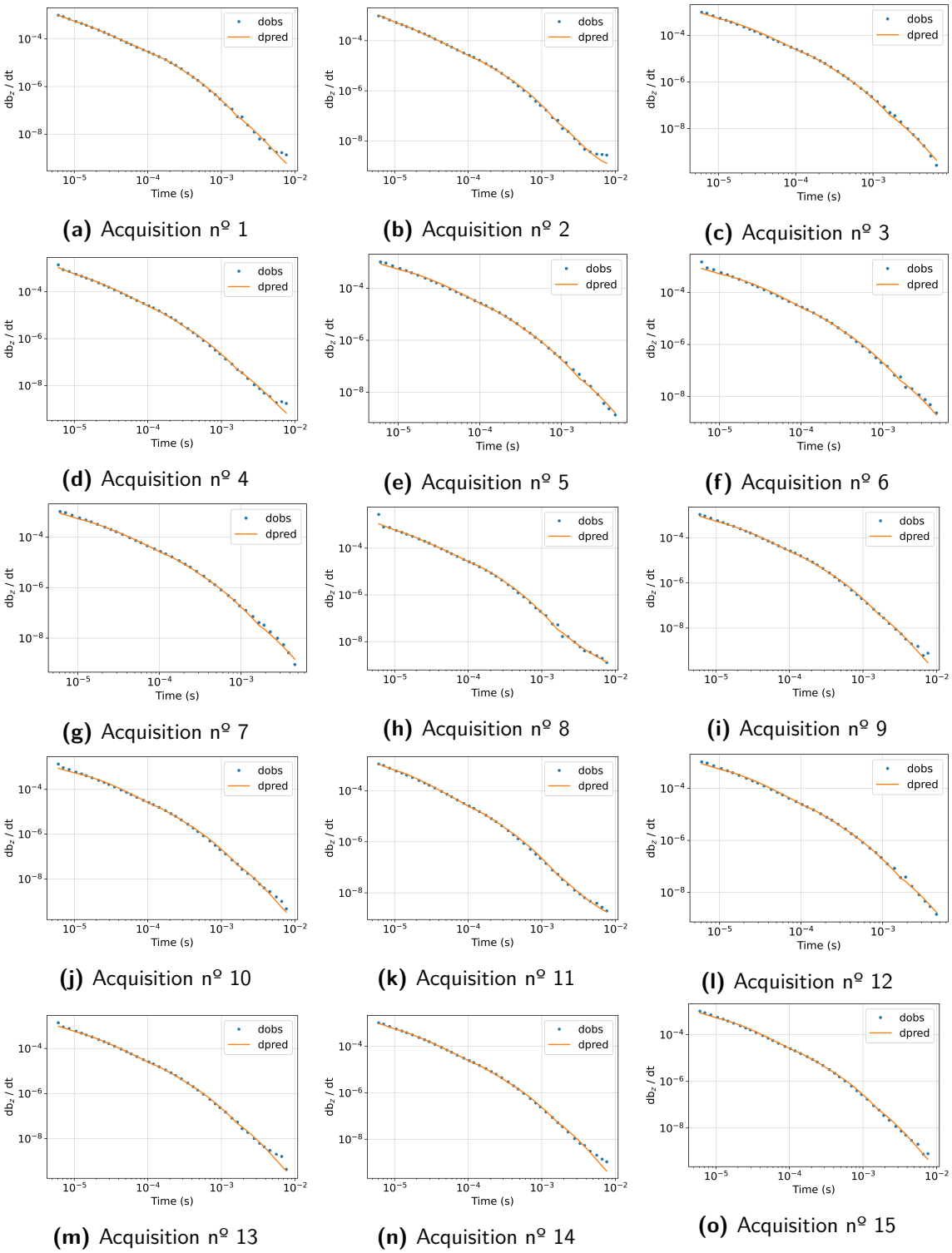

(a) Acquisition nº 1 **(b)** Acquisition nº 2 **(c)** Acquisition nº 3

(d) Acquisition nº 4 **(e)** Acquisition nº 5 **(f)** Acquisition nº 6

(g) Acquisition nº 7 **(h)** Acquisition nº 8 **(i)** Acquisition nº 9

(j) Acquisition nº 10 **(k)** Acquisition nº 11 **(l)** Acquisition nº 12

(m) Acquisition nº 13 **(n)** Acquisition nº 14 **(o)** Acquisition nº 15

Figure 5.13: Predicted and observed data for TDEM inversion of T2 with the reference model presented in Fig. 5.4b.

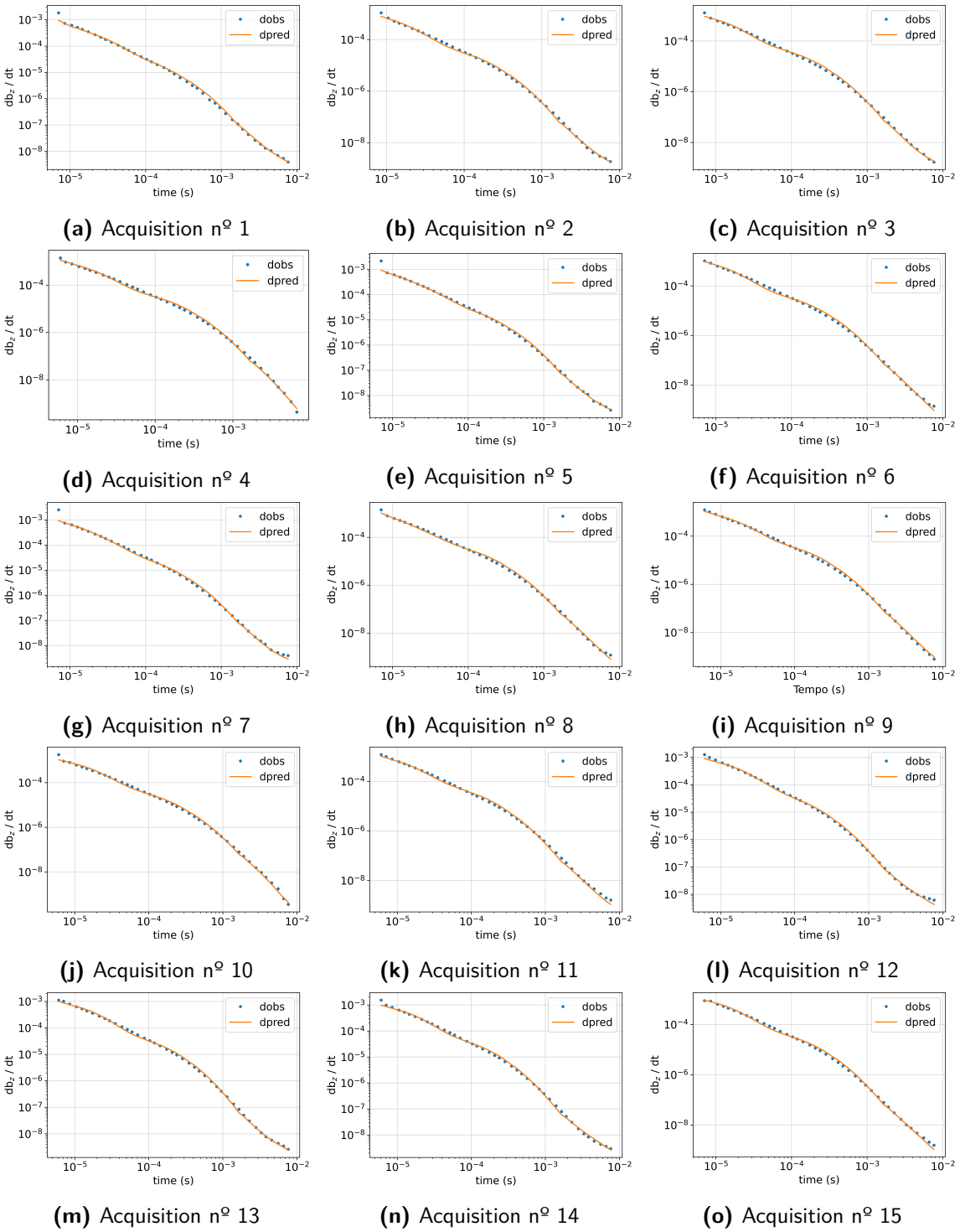

(a) Acquisition nº 1 **(b)** Acquisition nº 2 **(c)** Acquisition nº 3

(d) Acquisition nº 4 **(e)** Acquisition nº 5 **(f)** Acquisition nº 6

(g) Acquisition nº 7 **(h)** Acquisition nº 8 **(i)** Acquisition nº 9

(j) Acquisition nº 10 **(k)** Acquisition nº 11 **(l)** Acquisition nº 12

(m) Acquisition nº 13 **(n)** Acquisition nº 14 **(o)** Acquisition nº 15

Figure 5.14: Predicted and observed data for TDEM inversion of T1 with homogeneous reference model

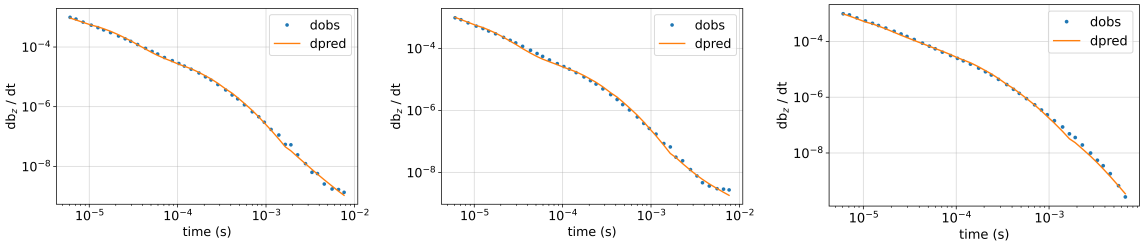

(a) Acquisition nº 1 **(b)** Acquisition nº 2 **(c)** Acquisition nº 3

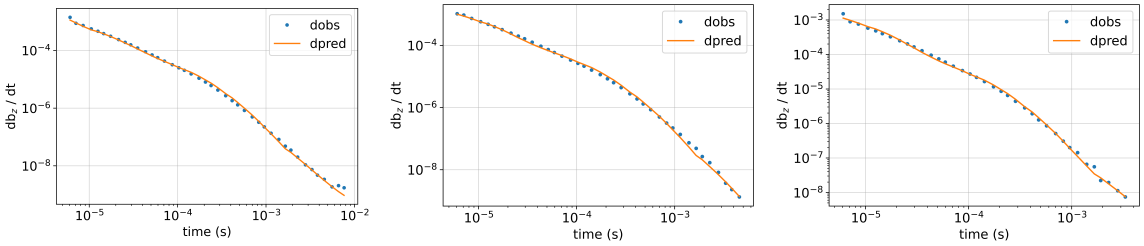

(d) Acquisition nº 4 **(e)** Acquisition nº 5 **(f)** Acquisition nº 6

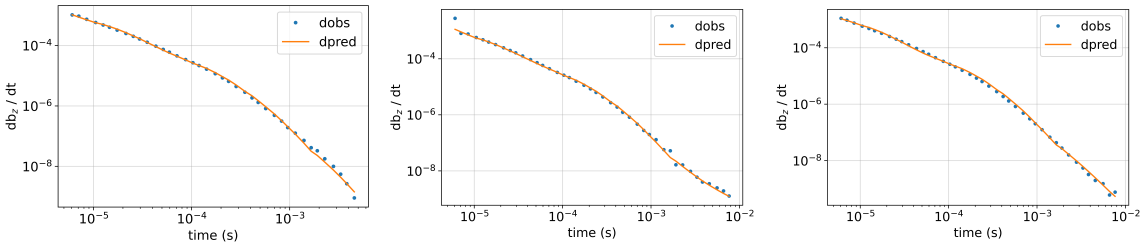

(g) Acquisition nº 7 **(h)** Acquisition nº8 **(i)** Acquisition nº 9

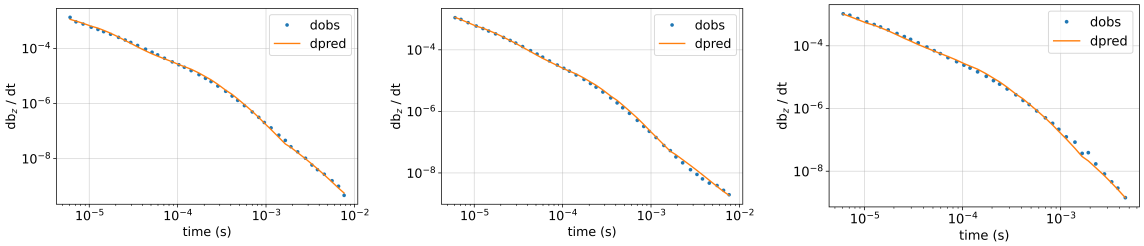

(j) Acquisition nº 10 **(k)** Acquisition nº 11 **(l)** Acquisition nº 12

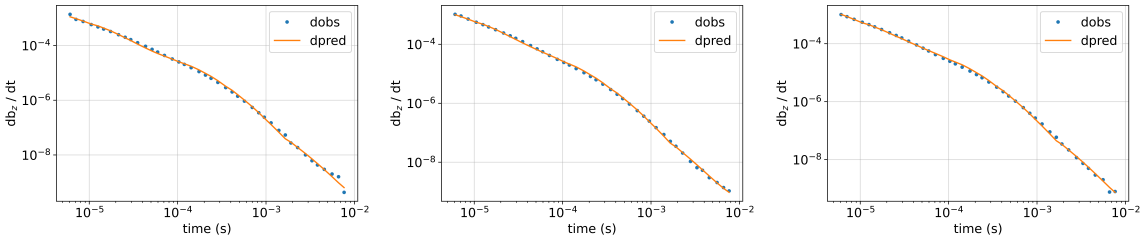

(m) Acquisition nº 13 **(n)** Acquisition nº 14 **(o)** Acquisition nº 15

Figure 5.15: Predicted and observed data for TDEM inversion of T2 with homogeneous reference model

5.6 Interpretative analyses of the inverted data with geotechnical tests

The best practice for geotechnical characterization is to compile all information available and compile them carefully into a coherent picture, to find the best solution to proceed with geotechnical projects. In this section, all the data available : SPT, boreholes, SSW surveys, ERT surveys, and TDEM surveys are analyzed (the place where the surveys were carried out are presented in Fig. 5.1). The processing and inversion of the ERT data are discussed in detail in [9]; those results are included here to provide a more comprehensive understanding of the investigated area. The original ERT survey lines were collected along the T1 and T2 TDEM profiles, with a length of 180 m each and electrode distances of 5 m. By using the inversion software RES2DINV, the retrieved resistivity models could fit the observations with mismatches respectively equal to 10.4% for the T1 profile and to 7.6% for the T2 profile. Figure 5.16 summarize the surveys for the section T1. The TDEM model seems to identify one layer from 20m to 30m that is assumed on the SSW as a unique layer from 20m to 43m. The TDEM model is in agreement with the SPT3 which also has this division, the difference is that the SPT3 doesn't go deeper, and only identifies the beginning of this layer (medium sand with gravels). From an engineer's point of view, this would imply an overestimation of the depth where the foundations could lay, implying a higher cost in the construction. By comparing the TDEM and ERT model, the lateral non-uniformity of the model with variable thickness is clear. At the center of the profile, assuming the blue variations as one single layer, four layers are identified: i) the shallowest one, representing the landfill, ii) the second one, representing the alluvium, iii) the third one, that is a mix of layers with higher or lower concentration of clay and sand (from SM5 and SPT3), and iv) the deeper layer, probably the 'medium sand with small gravels' identified in SPT3. The same interpretation can be performed for T2. A shallower layer with $\approx$ 5 m thick (in agreement with SPT2 and SM4) and 100-300 Ωm resistivity is identified in the ERT model. The TDEM does not record resistivity value of this layer, however the presence of this layer is identified. The vertical regularization at the TDEM model is smooth, which forces the reconstructed model to have a smooth transition between the shallowest (resistive) layer and the followed conductive layer. This thick conductive layer is related to the presence of clays (Alluvium layer from boreholes), the ERT, TDEM and SSW indentify this layer. In TDEM this layer appears as laterally continuous, but from the ERT is possible to see that from $\approx$ 65 to 100 m in x-direction this layer has a more resistivity material.

Figure 5.18, shows isolines for a) the depth of the base of the alluvium layer and b) for the depth of the top of the gravel layer. This image was created based on the interpretation of all geotechnical tests performed and presented in [61].

By inserting the TDEM and SSW results from T1 (Fig. 5.16) on these isomaps, it is clear that the alluvium layer is well defined, with a thickness $\approx$ 10m to 15m. The beginning of the stiff layer, from Fig. 5.18 is variable, going from 10m to 25m, and for the TDEM survey, this layer is identified at a depth of 30m.

Comparing Fig. 5.17 with the isomap (Fig. 5.18), T2 is inserted in a zone where the depth at which the alluvium layer ends is $\approx$ 15m to 20m, that is in agreement with the TDEM and SSW models.

T2 falls in area where the beginning of the gravel layer is not very specific, and the

information provided by the isomap is that the beginning of this layer is up to 10m, but from the TDEM and SSW models one could say that this layer starts at a depth of $\approx$ 25m.

After analyzing all information available, is possible to say that a good option (on the conservative side) to unload piles stress would be over 30m deep.

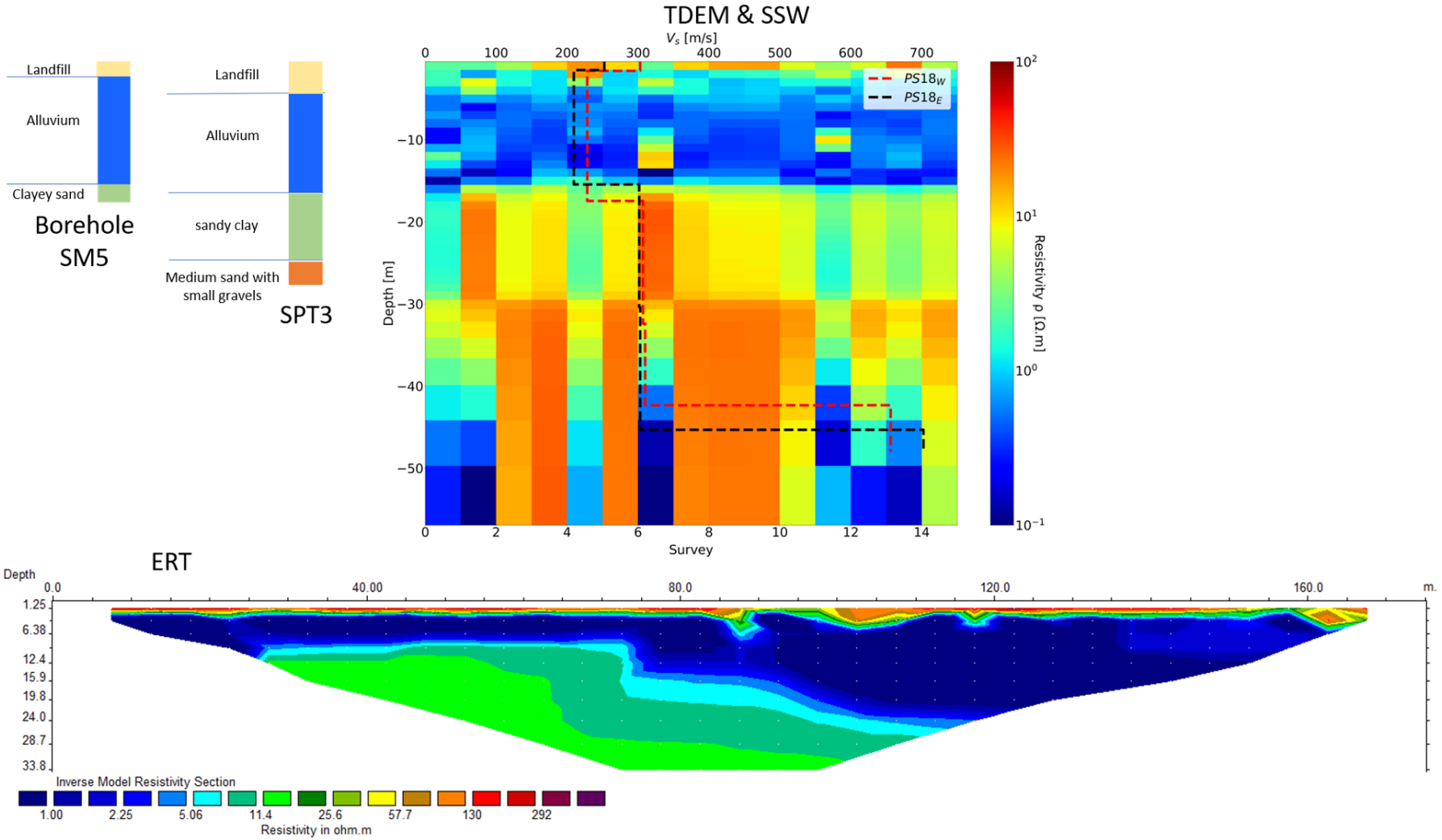

Figure 5.16: Summary of information available for T1: Borehole, SPT, SSW, TDEM and ERT

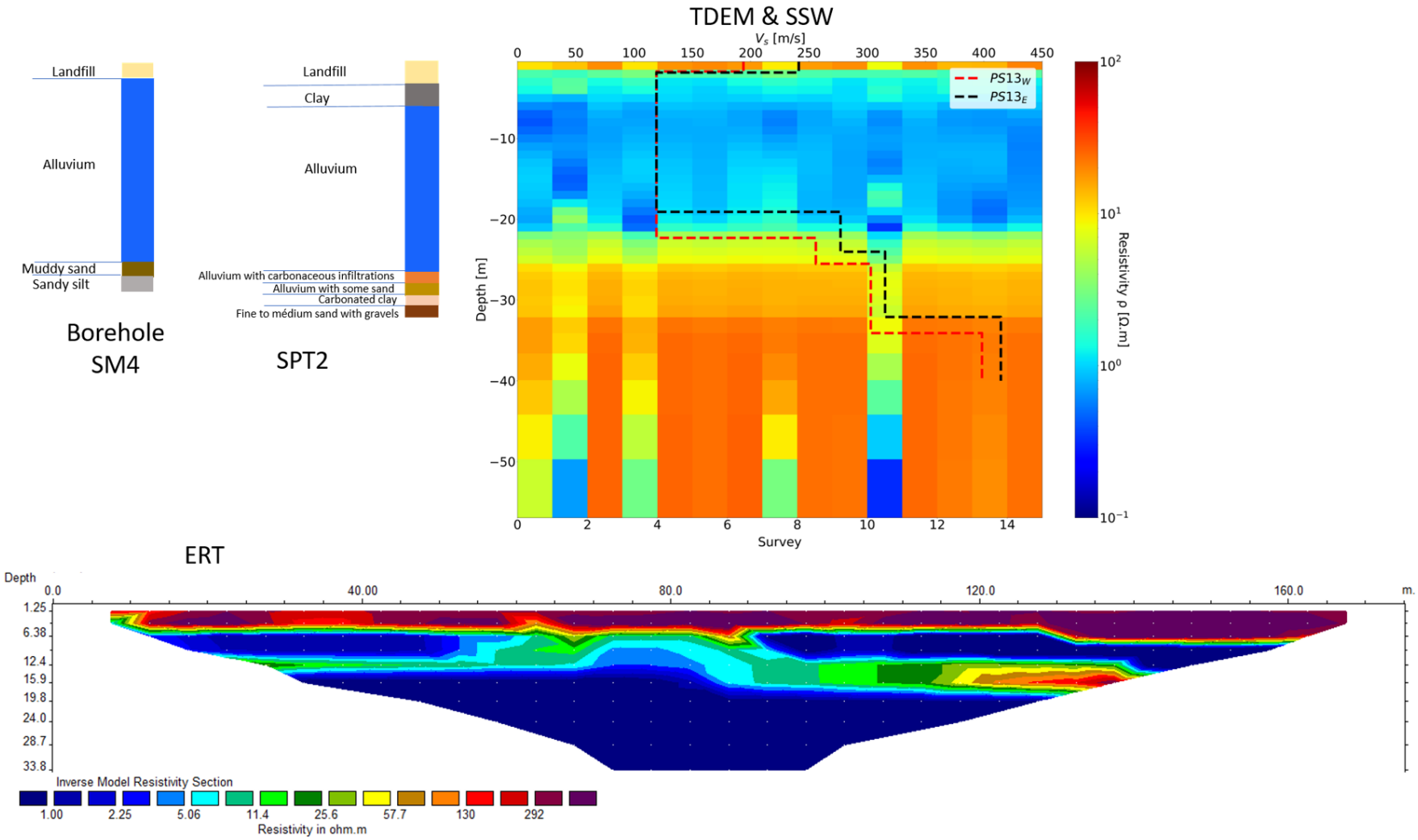

Figure 5.17: Summary of information available for T2: Borehole, SPT, SSW, TDEM and ERT

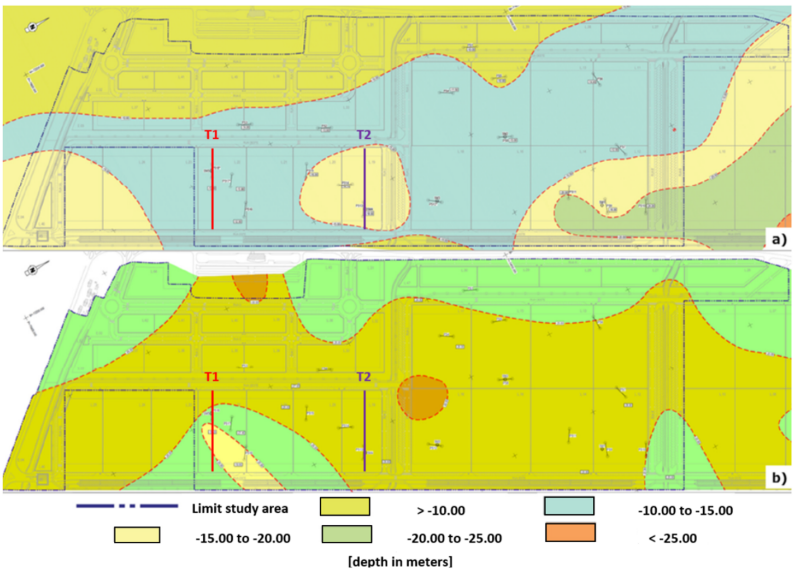

Figure 5.18: Isolines for: a) the depth of the base of the alluvium layer and b) for the depth of the top of the gravel layer. Adapted from [61]

Chapter 6

Conclusions and outlook

The lack of tools that are easy to deal with and able to perform tuning models to investigate a specific range of variations inspire the development of this thesis. Inversion strategies are well studied, and the minimum gradient support (MGS) stabilizer has been implemented in several algorithms, but never before to seismic surface waves (SSW). This thesis has successful implemented the MGS stabilizer, that is tunable and allows the user to efficiently explore the model space. In addition, the parameters controlling the inversion algorithm have a physical meaning (connected with the scales of the features that the user expects to see in the reconstructions). The stabilizer was tested on two synthetic datasets with different scales: from crustal to near-surface studies. The effectiveness of the stabilizer was also tested in real data and the results compared with information about the lithology that is available. The user has been instructed on how to set the focusing parameter ζ in order to investigate the space model with results with different degrees of sharpness. To provide a broad view of the model, a pseudo-2D inversion is also implemented through lateral constrain strategies. This allows the user to have a 2D image from the subsurface (although a 1D inversion of each sounding is performed) that is also tunable in z and x-direction. These strategies, developed in a general workflow, were applied to real and synthetic data.

Due to a lack of time, on the final field example in chapter 5, the SSW was not inverted with the procedure explained in 4 (despite of the fact of chapter 4 have also presented field examples). In the case of study, SSW models were obtained from previous inversions presented in [61]. The individual analyses of data can often lead to ambiguity and the model provided can not be sufficient to characterize the area in a desirable way. In order to get models with better resolution, more information about layers, and less uncertainty, a cross-analysis of different datasets was performed. The TDEM inversion constrained by the SSW data and by the borehole information gives a final model with well-defined layers, in agreement with the information available, thus allowing a more accurate geotechnical project.

Both methods, SSW and TDEM, have peculiar advantages and are able to discriminate between the different materials. The resolution and depth of investigation are depending on the acquisition geometries and on the quality of the signals; so, preliminary studies should be performed in advance to assess the possibility to reach the target to be investigated and the environmental noise of the site to guarantee "similar" performances of the two approaches. The main advantage of SSW consists of its capability of directly retrieving the shear modulus of the soil, G_0, which is extremely important for geotech-

nical characterizations and, in turn, for civil engineer applications. Both methodologies are severely ill-posed; thus, when possible, it would be useful to migrate the information from one method to the other (in some sort of joint interpretation/inversion) in order to get a unique, coherent (and more reliable) picture of the subsurface.

The TDEM model by itself (with a homogeneous reference model), gives good information about the subsurface, it misses the value of the first layer, because the loop size is 25m. With a shorter loop probably would be possible to better identify this layer, but, on the other hand, with a smaller loop wouldn't be possible to reach the bedrock. Since the first layer was characterized by the geotechnical prospecting (SPT, boreholes) and also by the SSW, it was thought it would be better to perform a large loop and reach the bedrock. By constraining the TDEM inversion with other datasets the weak point is the choice of the resistivity values. In this thesis, it relies on the writer's judgment after analyzing published tables and the ERT profile. An alternative would be to use equations that relate the shear-wave velocity to resistivity, a study with this already exists and equations are provided, but they are locally dependent and were created to be used in Southern Africa [51]. Another approach, which was the first idea for this thesis, but due to the short time it wasn't possible to implement, would be connecting the two datasets by geometrical/structural constrain which implies that where one property is changing (let's say the resistivity) also the other property (shear wave velocity) should change, regardless the amount. This approach would lead to a shear wave velocity profile with better resolution and low uncertainty. The shear wave velocity is correlated to the shear modulus, which is a fundamental parameter in the design of foundations, therefore, the implementation of a joint inversion through geometrical constraints would be a great improvement to be developed in the future.

Bibliography

[1] Ajo-Franklin, J. B., B. J. Minsley, and T. M. Daley
2007. Applying compactness constraints to differential traveltime tomography. *Geophysics*, 72(4):R67–R75.

[2] Aki, K., P. Richards, and U. S. Books
2002. *Quantitative Seismology*. University Science Books.

[3] Assembly, U. N.
2015. Transforming our world: the 2030 agenda for sustainable development– resolution adopted by the general assembly on 25 september 2015: 70/1. https://sustainabledevelopment.un.org/post2015/transformingourworld. United Nations– Sustainable Development knowledge online platform, accessed 28-October-2019.

[4] Auken, E. and A. V. Christiansen
2004. Layered and laterally constrained 2d inversion of resistivity data. *Geophysics*, 69(3):752–761.

[5] Auken, E., A. V. Christiansen, B. H. Jacobsen, N. Foged, and K. I. Sørensen
2005. Piecewise 1d laterally constrained inversion of resistivity data. *Geophysical Prospecting*, 53(4):497–506.

[6] Auken, E., N. Foged, and K. I. Sørensen
2002. Model recognition by 1-d laterally constrained inversion of resistivity data. In *8th EEGS-ES Meeting*.

[7] Bai, P., G. Vignoli, and T. Hansen
2021. Under revision. 1d stochastic inversion of airborne time-domain electromagnetic data with realistic prior and accounting for the forward modeling error. *Remote Sensing*.

[8] Baird, C.
2014. Science question with surprising answers. https://www.wtamu.edu/~cbaird/sq/2014/06/26/how-does-a-photon-accelerate-to-light-speed-so-quickly/. Retrieved July-2021.

[9] Baltazar, P., J. Viegas, G. Vignoli, C. Escada, F. Santos, F. Moreno, and J. Santos
2021. Conference paper: Inversion of electrical resistivity tomography (ERT) and transient electromagnetic (TEM) data for geotechnical site characterization of PLLN alluvial area, lisbon. https://www.issmge.org/publications/review-platform/conferences/isc2020. In Review Process.

[10] Boaga, J., G. Vignoli, and G. Cassiani
2011. Shear wave profiles from surface wave inversion: the impact of uncertainty on seismic site response analysis. *Journal of Geophysics and Engineering*, 8(2):162–174.

[11] Bowles, J. E.
1997. *Foundation analysis and design*, 5th edition.

[12] Braga, A. d. O.
1997. Métodos geoelétricos aplicados na caracterização geológica e geotécnica-formações rio claro e corumbataí no município de rio claro-sp. *Rio Claro*.

[13] Britannica
2022. Transcendental function. https://www.britannica.com/science/transcendental-function. From Encyclopedia Britannica. Retrieved January-2022.

[14] Britannica, E.
2021. Magnetic permeability. https://www.britannica.com/science/magnetic-permeability. "Accessed 11-March-2021".

[15] Britannica, T. E. o. E.
2020. Lenz's law. https://www.britannica.com/science/Lenzs-law. Retrieved September-2021.

[16] Callister, W. D. and D. G. Rethwisch
2011. *Materials science and engineering*, 8th edition. John wiley & sons NY.

[17] Camarate, J., G. Zbyszewski, and O. Ferreira
1962. Folha de alenquer 30-d. https://geoportal.lneg.pt/pt/dados_abertos/cgp50k/30-D. Explanatory News Sheet 30-D Alenquer. Text in Portuguese.

[18] Carrasquilla, A., C. A. Gonçalves, and E. Ulugergerli
2007. Evaluating the performance of different geophysical methods for groundwater prospecting in espirito santo basin-southeast brazil. *Tecnociencia*, 9(2):89–106.

[19] Cercato, M.
2007. Computation of partial derivatives of rayleigh-wave phase velocity using second-order subdeterminants. *Geophysical Journal International*, 170(1):217–238.

[20] Cockett, R., S. Kang, L. J. Heagy, A. Pidlisecky, and D. W. Oldenburg
2015. Simpeg: An open source framework for simulation and gradient based parameter estimation in geophysical applications. *Computers & Geosciences*, 85:142–154.

[21] Comina, C.
2001. Inversione congiunta di misura di resistività e di propagazione di onde superficiali. Master's thesis, Politecnico di Torino - Facoltà di Ingegneria. Text in Italian.

[22] Constable, S. C., R. L. Parker, and C. G. Constable
1987. Occam's inversion: A practical algorithm for generating smooth models from electromagnetic sounding data. *Geophysics*, 52(3):289–300.

[23] Coutinho, M. and F. Leão
2016. Estudo de impacte ambiental do cais fluvial da castanheira do ribatejo. Report R049.16-15/06.06, Instituto do Ambiente e Desenvolvimento. Text in Portuguese.

[24] Dal Moro, G., M. Pipan, and P. Gabrielli
2007. Rayleigh wave dispersion curve inversion via genetic algorithms and marginal posterior probability density estimation. *Journal of Applied Geophysics*, 61(1):39–55.

[25] Dentith, M. and S. T. Mudge
2014. *Geophysics for the mineral exploration geoscientist*. Cambridge University Press.

[26] Dokht Dolatabadi Esfahani, R., A. Gholami, and M. Ohrnberger
2020. An inexact augmented lagrangian method for nonlinear dispersion-curve inversion using dix-type global linear approximation. *Geophysics*, 85(5):EN77–EN85.

[27] Dragonetti, G., A. Comegna, A. Ajeel, G. P. Deidda, N. Lamaddalena, G. Rodriguez, G. Vignoli, and A. Coppola
2018. Calibrating electromagnetic induction conductivities with time-domain reflectometry measurements. *Hydrology and Earth System Sciences*, 22(2):1509–1523.

[28] E Richart, F.
1970. *Vibrations of soils and foundations*. Printed in the United States of America.

[29] Erkan, K.
2008. A comparative overview of geophysical methods. Technical report, Ohio State University. Division of Geodetic Science.

[30] Farquharson, C. G. and D. W. Oldenburg
2004. A comparison of automatic techniques for estimating the regularization parameter in non-linear inverse problems. *Geophysical Journal International*, 156(3):411–425.

[31] Ferreira, J.
2004. Modelação da excitação dinâmica superficial do subsolo. aplicação à análise espectral das ondas de superfície. Master's thesis, Instituto Superior Técnico. Text in Portuguese.

[32] Fiandaca, G., J. Doetsch, G. Vignoli, and E. Auken
2015. Generalized focusing of time-lapse changes with applications to direct current and time-domain induced polarization inversions. *Geophysical Journal International*, 203(2):1101–1112.

[33] Foti, S.
2000. *Multistation methods for geotechnical characterization using surface waves*. PhD thesis, Politecnico di Torino.

[34] Foti, S., F. Hollender, F. Garofalo, D. Albarello, M. Asten, P.-Y. Bard, C. Comina, C. Cornou, B. Cox, G. Di Giulio, et al.
2018. Guidelines for the good practice of surface wave analysis: A product of the interpacific project. *Bulletin of Earthquake Engineering*, 16(6):2367–2420.

[35] Foti, S. and C. Strobbia
2002. Some notes on model parameters for surface wave data inversion. In *Symposium*

on the Application of Geophysics to Engineering and Environmental Problems 2002, Pp. SEI6–SEI6. Society of Exploration Geophysicists.

[36] GEOPSY
2021. Geopsy. http://www.geopsy.org/index.html. Open source software for geophysical research and applications. Retrieved August-2021.

[37] Giordano, N. and C. Comina
2016. Combined 3d seismic and resistivity surveys for the stability study of a natural bridge in conglomerate rock. In *Near Surface Geoscience 2016-22nd European Meeting of Environmental and Engineering Geophysics*, Pp. cp–495. European Association of Geoscientists & Engineers.

[38] Gouveia, F. M. P.
2017. *Dynamic characterization of the soil in urban areas under confined conditions*. PhD thesis, Universidade de Lisboa - Instituto Superior Técnico - Departamento de Eng. Civil, Arquitetura e Georrecursos.

[39] Guillemoteau, J., G. Vignoli, J. Barreto, and G. Sauvin
2021. Under revision. Sparse laterally constrained inversion of surface wave dispersion curves via minimum gradient support regularization. *Geophysics*.

[40] Haber, E.
2014. *Computational methods in geophysical electromagnetics*. SIAM.

[41] Haney, M. M. and L. Qu
2010. Rayleigh wave dispersion curve inversion: Occam versus the l1-norm. In *SEG Technical Program Expanded Abstracts 2010*, Pp. 1871–1876. Society of Exploration Geophysicists.

[42] Haney, M. M. and V. C. Tsai
2017. Perturbational and nonperturbational inversion of rayleigh-wave velocities. *Geophysics*, 82(3):F15–F28.

[43] Hansen, C.
2008. *Regularization Tools – A Matlab Package for Analysis and Solution of Discrete Ill-Posed Problems*. Technical University of Denmark.

[44] Hansen, T. M., K. S. Cordua, B. H. Jacobsen, and K. Mosegaard
2014. Accounting for imperfect forward modeling in geophysical inverse problems—exemplified for crosshole tomography. *Geophysics*, 79(3):H1–H21.

[45] Haskell, N. A.
1953. The dispersion of surface waves on multilayered media. *Bulletin of the seismological Society of America*, 43(1):17–34.

[46] Haus, H. A. and J. R. Melcher
1989. *Electromagnetic fields and energy*, volume 107. Prentice Hall Englewood Cliffs, NJ.

[47] Heagy, L. J.
2018. *Electromagnetic methods for imaging subsurface injections*. PhD thesis, University of British Columbia.

[48] Hubbard, S., J. Peterson Jr, E. Majer, P. Zawislanski, K. Williams, J. Roberts, and F. Wobber
1997. Estimation of permeable pathways and water content using tomographic radar data. *The leading EDGE*, 16(11):1623–1630.

[49] Issa, B., I. M. Obaidat, B. A. Albiss, and Y. Haik
2013. Magnetic nanoparticles: surface effects and properties related to biomedicine applications. *International journal of molecular sciences*, 14(11):21266–21305.

[50] Ivanov, J., G. Tsoflias, R. D. Miller, S. Peterie, S. Morton, and J. Xia
2016. Impact of density information on rayleigh surface wave inversion results. *Journal of Applied Geophysics*, 135:43–54.

[51] Jones, A. G., S. Fishwick, R. L. Evans, M. R. Muller, and J. Fullea
2013. Velocity-conductivity relations for cratonic lithosphere and their application: Example of southern africa. *Geochemistry, Geophysics, Geosystems*, 14(4):806–827.

[52] Kausel, E.
1981. *An explicit solution for the Green functions for dynamic loads in layered media.* Department of Civil Engineering, School of Engineering, Massachusetts ....

[53] Kausel, E.
2005. Waves propagation modes: From simple systems to layered soils. In *Surface Waves in Geomechanics: Direct and Inverse Modelling for Soils and Rocks*, Pp. 165–202. Springer.

[54] Kausel, E. and J. M. Roësset
1981. Stiffness matrices for layered soils. *Bulletin of the seismological Society of America*, 71(6):1743–1761.

[55] Key, K.
2016. Mare2dem: a 2-d inversion code for controlled-source electromagnetic and magnetotelluric data. *Geophysical Journal International*, 207(1):571–588.

[56] Krivochieva, S. and M. Chouteau
2002. Whole-space modeling of a layered earth in time-domain electromagnetic measurements. *Journal of Applied Geophysics*, 50(4):375–391.

[57] Lai, C. G.
2005. Surface waves in dissipative media: Forward and inverse modelling. In *Surface waves in geomechanics: direct and inverse modelling for soils and rocks*, Pp. 73–163. Springer.

[58] Larsson, J.
2007. Electromagnetics from a quasistatic perspective. *American Journal of Physics*, 75(3):230–239.

[59] Last, B. and K. Kubik
1983. Compact gravity inversion. *Geophysics*, 48(6):713–721.

[60] Ley-Cooper, A. Y., A. Viezzoli, J. Guillemoteau, G. Vignoli, J. Macnae, L. Cox, and T. Munday
2015. Airborne electromagnetic modelling options and their consequences in target definition. *Exploration Geophysics*, 46(1):74–84.

[61] Lopes, I., G. Tavares, G. Ferreira, B. Peniche, and J. Santos
2018. Joint inversion of masw and rayleigh wave ellipticity in the site characterization of plln alluvial area, VFX, N Lisbon. In *24th European Meeting of Environmental and Engineering Geophysics*.

[62] Ludwig, R., H. Gerhards, P. Klenk, U. Wollschläger, and J. Buchner
2009. Electromagnetic methods in applied geophysics. *Institute of Environmental Physics Heidelberg University*.

[63] Luo, Y., J. Xia, J. Liu, Q. Liu, and S. Xu
2007. Joint inversion of high-frequency surface waves with fundamental and higher modes. *Journal of Applied Geophysics*, 62(4):375–384.

[64] Lysmer, J.
1970. Lumped mass method for rayleigh waves. *Bulletin of the Seismological Society of America*, 60(1):89–104.

[65] MacNeill, J.
1980. *Electrical conductivity of soils and rocks*. Geonics Limited.

[66] Madsen, R. B. and T. M. Hansen
2018. Estimation and accounting for the modeling error in probabilistic linearized amplitude variation with offset inversion. *Geophysics*, 83(2):N15–N30.

[67] Maraschini, M. and S. Foti
2010. A monte carlo multimodal inversion of surface waves. *Geophysical Journal International*, 182(3):1557–1566.

[68] Monteiro Santos, F. A.
2012. Prospecção geofísica 1. Apontamentos da disciplina de Prospecção Geofísica 1 - Faculdade de Ciências da Universidade de Lisboa.

[69] Nabighian, M., ed.
1988. *Electromagnetic methods in applied geophysics*, volume 1. Society of Exploration Geophysicists.

[70] Nabighian, M. N., J. C. Macnae, et al.
1991. Time domain electromagnetic prospecting methods. *Electromagnetic methods in applied geophysics*, 2(Part A):427–509.

[71] Nelles, O.
2013. *Nonlinear System Identification: From Classical Approaches to Neural Networks, Fuzzy Models, and Gaussian Processes*. Springer Nature.

[72] Oldenburg, D. W. and Y. Li
1999. Estimating depth of investigation in dc resistivity and ip surveys. *Geophysics*, 64(2):403–416.

[73] Oldenburg, D. W. and Y. Li
2005. Inversion for applied geophysics: A tutorial. *Investigations in geophysics*, 13:89–150.

[74] Pagliara, G. and G. Vignoli
2006. Focusing inversion techniques applied to electrical resistance tomography in an experimental tank. *arXiv preprint physics/0606234*.

[75] Park, C. B.
2005. Masw horizontal resolution in 2d shear-velocity (vs) mapping. *Open-File Report, Lawrence: Kansas Geologic Survey*.

[76] Park, C. B. and M. Carnevale
2010. Optimum masw survey—revisit after a decade of use. In *GeoFlorida 2010: Advances in Analysis, Modeling & Design*, Pp. 1303–1312.

[77] Park, C. B., R. D. Miller, and J. Xia
1999. Multichannel analysis of surface waves. *Geophysics*, 64(3):800–808.

[78] Park, C. B., R. D. Miller, J. Xia, and J. Ivanov
2007. Multichannel analysis of surface waves (masw)—active and passive methods. *The Leading Edge*, 26(1):60–64.

[79] Park, S.
2021. Multichannel analysis of surface waves (masw). http://www.masw.com/OverallProcedure.html. MASW website from Park Seismic LLC. Retrieved June-2021.

[80] Parkhomenko, E. I.
2012. *Electrical properties of rocks*. Springer Science & Business Media.

[81] Pfaffhuber, A. A., M. Bastani, S. Cornee, M. Rømoen, S. Donohue, T. E. Helle, M. Long, P. O'Connor, and L. Persson
2010. Multi-method high resolution geophysical & geotechnical quick clay mapping. In *Near Surface 2010-16th EAGE European Meeting of Environmental and Engineering Geophysics*, Pp. cp–164. European Association of Geoscientists & Engineers.

[82] Rashid, Q. A., H. Abuel-Naga, E.-C. Leong, Y. Lu, and H. Al Abadi
2018. Experimental-artificial intelligence approach for characterizing electrical resistivity of partially saturated clay liners. *Applied Clay Science*, 156:1–10.

[83] Samouëlian, A., I. Cousin, A. Tabbagh, A. Bruand, and G. Richard
2005. Electrical resistivity survey in soil science: a review. *Soil and Tillage research*, 83(2):173–193.

[84] Samtani, N. C. and E. A. Nowatzki
2006. Soils and foundations: Reference manual vol. i. Technical report, United States. Federal Highway Administration.

[85] Santamarina, J. C., K. A. Klein, and M. A. Fam
2001. *Soils and waves*, volume 316. J. Wiley & Sons New York.

[86] Sauvin, G., S. Bazin, M. Vanneste, I. Lecomte, and A. Pfaffhuber
2011. Towards joint inversion/interpretation for landslide-prone areas in norway-integrating geophysics and geotechnique. In *Near Surface 2011-17th EAGE European Meeting of Environmental and Engineering Geophysics*, Pp. cp–253. European Association of Geoscientists & Engineers.

[87] Sauvin, G., I. Lecomte, S. Bazin, J.-S. L'Heureux, M. Vanneste, I.-L. Solberg, and E. Dalsegg
2013. Towards geophysical and geotechnical integration for quick-clay mapping in norway. *Near Surface Geophysics*, 11(6):613–624.

[88] Schwab, F. and L. Knopoff
1971. Surface waves on multilayered anelastic media. *Bulletin of the Seismological Society of America*, 61(4):893–912.

[89] SimPEG
2019. Simpeg.xyz. https:http://docs.simpeg.xyz/content/api_core/api_Mesh.html. Simulation and Parameter Estimation in Geophysics – SimPEG Online platform. Retrieved April-2019.

[90] Slichter, L. B. and M. Telkes
1942. Electrical Properties of Rocks and Minerals. In *Handbook of Physical Constants*, chapter 21, Pp. 300–319. Geological Society of America.

[91] Socco, L. V., D. Boiero, S. Foti, and R. Wisén
2009. Laterally constrained inversion of ground roll from seismic reflection records. *Geophysics*, 74(6):G35–G45.

[92] Solberg, I.-L., M. Long, V. C. Baranwal, A. S. Gylland, and J. S. Rønning
2016. Geophysical and geotechnical studies of geology and sediment properties at a quick-clay landslide site at esp, trondheim, norway. *Engineering Geology*, 208:214–230.

[93] Spichak, V. V.
2015. *Electromagnetic sounding of the Earth's interior*, volume 40, chapter 3, Pp. 47–78. Elsevier, 2 edition.

[94] Strobbia, C.
2003. *Surface wave methods: acquisition, processing and inversion*. PhD thesis, Politecnico di Torino - Dottorato di Ricerca in Geoingegneria Ambientale.

[95] Strobbia, C., L. Andreas, P. Vermeer, and A. Glushchenko
2011. Surface waves: use them then lose them. surface-wave analysis, inversion and attenuation in land reflection seismic surveying. *Near Surface Geophysics*, 9(6):503–513.

[96] Survey, U. G.
2021. Body waves. https://earthquake.usgs.gov/learn/glossary/?term=body%20wave. Earthquake Glossary - Retrieved September-2021.

[97] Tarantola, A.
2005. *Inverse problem theory and methods for model parameter estimation*. SIAM.

[98] und Wissen, K. L.
2021. Basic geophysics: Surface waves. https://www.youtube.com/watch?v=3bTI2g-dQ_A&t=310s. YouTube Channel - A production of the Geophysical Institute (GPI) in collaboration with the Center for Technology-Enhanced Learning (ZML) at the Karlsruhe Institute of Technology (KIT) (in German) - Retrieved July-2021.

[99] Viegas, J., P. Baltazar, G. Vignoli, F. Santos, and J. Santos
2021. Conference paper: Inversion of TDEM data constrained by surface seismic and borehole surveys for geotechnical characterization of the northen lisbon logistic park PLL. In *DCE21-Symposium on Civil Engineering and Spatial Planning: Book of Abstracts*, H. Varum, A. Costa, J. Martins, D. Clemente, J. Martins, and P. Soares, eds., P. 169. FEUP edições.

[100] Vignoli, G., R. Deiana, and G. Cassiani
2012. Focused inversion of vertical radar profile (vrp) traveltime data. *Geophysics*, 77(1):H9–H18.

[101] Vignoli, G., G. Fiandaca, A. V. Christiansen, C. Kirkegaard, and E. Auken
2015. Sharp spatially constrained inversion with applications to transient electromagnetic data. *Geophysical Prospecting*, 63(1):243–255.

[102] Vignoli, G., I. Gervasio, G. Brancatelli, J. Boaga, B. Della Vedova, and G. Cassiani
2016. Frequency-dependent multi-offset phase analysis of surface waves: an example of high-resolution characterization of a riparian aquifer. *Geophysical Prospecting*, 64(1):102–111.

[103] Vignoli, G., J. Guillemoteau, J. Barreto, and M. Rossi
2021. Reconstruction, with tunable sparsity levels, of shear wave velocity profiles from surface wave data. *Geophysical Journal International*, 225(3):1935–1951.

[104] Vignoli, G., V. Sapia, A. Menghini, and A. Viezzoli
2017. Examples of improved inversion of different airborne electromagnetic datasets via sharp regularization. *Journal of Environmental and Engineering Geophysics*, 22(1):51–61.

[105] Vignoli, G., C. Strobbia, G. Cassiani, and P. Vermeer
2011. Statistical multioffset phase analysis for surface-wave processing in laterally varying media. *Geophysics*, 76(2):U1–U11.

[106] Vignoli, G. and L. Zanzi
2005. Focusing inversion technique applied to radar tomographic data. In *Near Surface 2005-11th European Meeting of Environmental and Engineering Geophysics*.

[107] Ward, S. H. and G. W. Hohmann
1988. Electromagnetic theory for geophysical applications. In *Electromagnetic Methods in Applied Geophysics: Voume 1, Theory*, Pp. 130–311. Society of Exploration Geophysicists.

[108] Wathelet, M.
2005. *Array recordings of ambient vibrations: surface-wave inversion*. PhD thesis, Université de Liège - Faculté des Sciences Appliquées. A thesis submitted for the degree of Doctor of Applied Sciences presented by Marc Wathelet.

[109] Wathelet, M.
2008. An improved neighborhood algorithm: parameter conditions and dynamic scaling. *Geophysical Research Letters*, 35(9).

[110] Wathelet, M., D. Jongmans, and M. Ohrnberger
2004. Surface-wave inversion using a direct search algorithm and its application to ambient vibration measurements. *Near surface geophysics*, 2(4):211–221.

[111] Wisén, R. and A. V. Christiansen
2005. Laterally and mutually constrained inversion of surface wave seismic data and resistivity data. *Journal of Environmental & Engineering Geophysics*, 10(3):251–262.

[112] Xia, J., R. D. Miller, and C. B. Park
1999. Estimation of near-surface shear-wave velocity by inversion of rayleigh waves. *Geophysics*, 64(3):691–700.

[113] Xing, G., F. Niu, M. Chen, and Y. Yang
2016. Effects of shallow density structure on the inversion for crustal shear wave speeds in surface wave tomography. *Geophysical Journal International*, 205(2):1144–1152.

[114] Zhao, C., P. Yu, and L. Zhang
2016. A new stabilizing functional to enhance the sharp boundary in potential field regularized inversion. *Journal of Applied Geophysics*, 135:356–366.

[115] Zhdanov, M. and E. Tolstaya
2004. Minimum support nonlinear parametrization in the solution of a 3d magnetotelluric inverse problem. *Inverse problems*, 20(3):937.

[116] Zhdanov, M., G. Vignoli, and T. Ueda
2006. Sharp boundary inversion in crosswell travel-time tomography. *Journal of Geophysics and Engineering*, 3(2):122–134.

[117] Zhdanov, M. S.
2002. *Geophysical inverse theory and regularization problems*, volume 36. Elsevier.

[118] Zunino, A. and K. Mosegaard
2019. An efficient method to solve large linearizable inverse problems under gaussian and separability assumptions. *Computers & Geosciences*, 122:77–86.

[119] Zunino, A., K. Mosegaard, K. Lange, Y. Melnikova, and T. Mejer Hansen
2015. Monte carlo reservoir analysis combining seismic reflection data and informed priors. *Geophysics*, 80(1):R31–R41.